



Norwegian University of  
Science and Technology

# Ultimate Strength and Capacity Assessment of Ice Class Vessel Operating in Ice

**Håkon Mork**

Marine Technology

Submission date: July 2016

Supervisor: Bernt Johan Leira, IMT

Co-supervisor: Håvard Nyseth, DNV GL, Høvik  
Sören Ehlers, IMT

Norwegian University of Science and Technology  
Department of Marine Technology





## Problem Description

Heading: Ultimate strength and capacity assessment of ice class vessel operating in ice

1. A review of ice properties and alternative methods for representing ice should be carried out. A material model implemented by a previous MSc student in cooperation with DNV GL in 2013 may be used as basis for the review.
2. A brief study on non-linear structural analysis and its application on ultimate capacity strength assessments of frame structures in ships should be carried out.
3. Establish a finite element model of a part of the bow section of a selected ice-strengthened vessel. The structural model should extend longitudinally between two bulkheads and vertically between the tank top and the main deck. The model will be used for linear and non-linear structural analysis using ABAQUS. The student may take advantage of previous models developed by DNV GL.
4. A parameter study should be carried out to evaluate the response in the hull structure when subject to a given load patch. The structural model developed in item 3 is to be used as basis for the work. Parameters to be varied may be the size of the patch (length and height) and the applied position on the hull structure.
5. Based on a relevant impact scenario, a quasi-static non-linear analysis is to be carried out of the hull structure under extreme ice loading (loading and unloading). The ultimate capacity of the structure is to be evaluated in terms of yielding, permanent sets and plastic straining. Design loads from ice class rules may also be looked into.



## Preface

This is an individual master thesis written in cooperation with the Department of Ship Structures - Maritime Advisory at DNV GL, where I have previously worked as a summer intern. The work has been carried out at DNV GL's main office at Høvik, except for a few weeks spent at The Department of Marine Technology at The Norwegian University of Science and Technology (NTNU), Trondheim. The thesis is the final project of my Master of Science degree at NTNU within the field of marine technology and structural engineering, and was written during the spring and summer of 2016.

During the last year I have taken interest in arctic engineering, and I have had several courses and written a project thesis within ice engineering. DNV GL gave me the opportunity to take part in a project related to ice loading and hull strength for this master thesis, which also allowed me to take advantage of the project thesis. It has been a great experience to use theory and skills obtained throughout my education in an ongoing project between DNV GL and a customer. The work has been instructive and interesting and I hope this thesis, including scripts and results, will be useful for DNV GL in the continuation of the project.

I would like to thank everyone who has been involved and helped me with my work. Special greetings go to DNV GL supervisors, Ole Jakob Hareide and Håvard Nyseth, whom I have had meetings with on a regular basis. Their advice and our discussions have been constructive and crucial for the progress and direction of the thesis. I am grateful for having the opportunity to write my thesis in collaboration with my department at DNV GL and for getting access to a desk, a computer and relevant software.

Professor Sören Ehlers (TUHH/NTNU) has been an important resource, especially in the planning phase and when the project thesis was written when I was still at Hamburg University of Technology (TUHH). I would also like to thank my main supervisor from NTNU, Professor Bernt J. Leira, who has been helpful in the final period of the work. During the meetings we had and through email correspondence he has provided vital feedback. At last, I would like to thank friends who have been helpful proofreading the thesis.

Håkon Mork



DNV GL, Høvik, July 2016



## Abstract

In an ongoing project between DNV GL and a customer, the ultimate strength and damage on a ship exposed to ice loading are to be assessed. The vessel has the DNV GL class notation Ice(1A\*), but is now considered for operation in more severe ice conditions than it initially was designed for. The purpose of the thesis is to analyze the response of a hull model subjected to different loads and to determine the residual capacities after first yield. Ice properties and numerical models will also be reviewed.

Ice as a material is complex because its properties are strongly dependent on parameters such as strain, strain rate, porosity, salinity, crystal structure and stress-state. Moreover, the load distribution exerted by ice on impacting structures is highly irregular due to brittle failure, including fracturing, crushing and spalling. These properties make ice difficult to model. The developed numerical models all have their flaws and there are currently no "verified" material models for ice, despite decades of research. The main issue seems to be their ability to reproduce the irregular load distributions.

Class rules use a simplified approach where it is assumed that all energy will be dissipated by the ice, implying crushing of ice. When exceeding design load level, the hull will start to deform plastically and the residual capacity will be utilized. Ice class vessels are actually expected to experience loads somewhat larger than the design loads, and some deformation is accepted. The rules do, however, only have a single design point at first yield and there are no further requirements on the residual strength of the hull.

A finite element model of a part of the bow was considered. Rectangular, uniform pressure patches of different sizes were applied at different locations of the model. Linear response analyses were executed and the capacity with respect to first yield was determined. The highest stress levels occurred in the stiffeners, and loads centered the farthest away from the bulkheads were found to be the most critical. Linear capacities ranged between 1.3 MPa and 3.7 MPa. It was also found that the rule design loads are similar to the first yield capacities calculated.

The residual capacities were determined by doing nonlinear finite element analyses. A user defined ultimate strength criterion based on maximum allowable permanent deformations was made. Permanent lateral deformation at stiffener midspan of 0.5 % or 1.0 % of the stiffener length was set as a criterion. The idea was to allow deformations that can be regarded as acceptable, and the strain levels were found to be well below material capacity using these criteria. The hull showed to exhibit ultimate strengths in the range of 1.5 to 3.6 times the linear capacity, depending on the load distribution. Two boundary conditions were considered, and they gave equal results.

Even though the hull exhibits large residual capacities after first yield, it is questioned whether this alone can be used as leverage for allowing the vessel to operate in more severe ice conditions than it was designed for. Ice loads larger than design loads are expected in the first place, so some of this residual strength is taken into account by the class notations. Numerous damages on ice class vessels have been reported, so it

---

is clear that the simplified method used in class notations has its weaknesses.

For future work it is recommended to do analyses with nonuniform pressure patches, which is more realistic and more conservative. Doing long-term full scale measurements is also recommended. A distribution function can be fit to the the measured loads and from this a new design load can be determined using a probabilistic approach. Using the capacities calculated in this thesis, it can be determined whether the vessel can operate in harsher ice conditions than it was initially designed for or not.

## Sammendrag

I et pågående prosjekt mellom DNV GL og en kunde skal maksimal skrogstyrke og skader på et skipsskrog utsatt for islast vurderes. Fartøyet har DNV GLs klassenotasjon Ice(1A \*), men det vurderes nå om det er forsvarlig å la skipet operere i verre isforhold enn skipet er designet for. Formålet med oppgaven er å analysere responsen når skroget utsettes for ulike laster og å bestemme reststyrke etter første flyt. Isegenskaper og numeriske modeller for is skal også bli gjennomgått.

Is som materiale er komplekst ettersom egenskapene er sterkt avhengige av parametre som tøyning, tøyningshastighet, porøsitet, salinitet, krystallstruktur og spenningstilstand. Lastfordelingen under sammenstøt er høyst ujevn på grunn av isens sprø egenskaper som resulterer i sprekkdannelser, knusing og at biter knekker av. Disse egenskapene gjør at is er svært vanskelig å modellere. Eksisterende materialmodeller for is er mangelfulle, og det finnes ingen ”verifisert” materialmodell på tross av flere tiår med forskning. Hovedproblemet med modellene er evnen deres til å reprodusere de ujevne trykkfordelingene som oppstår under sammenstøt.

Klasseregler bruker en forenklet metode hvor det antas at all energi absorberes av isen, noe som betyr at isen knuses. Ved en overskridelse av dette lastnivået vil skroget deformeres plastisk, og noe av reststyrken utnyttes. For fartøy med isklasse forventes det faktisk at laster større enn designlastene oppstår under seiling, ettersom permanente deformasjoner er akseptert. Reglene bruker likevel er bare ett enkelt designpunkt, som er første flyt, og det er ingen ytterligere krav til reststyrke.

Beregninger ble utført på en elementmetodemodell av en del av baugen. Modellen ble lastet med nesten-rektangulære, jevnt fordelte trykk i ulike størrelser, sentrert på forskjellige steder av modellen. Lineære responsanalyser ble utført og last ved første flyt ble beregnet. De høyeste spenningsnivåene forekom i stiverne og laster sentrert lengst bort fra skottene viste seg å være mest kritisk. De lineære lastkapasitetene er mellom 1,3 MPa og 3,7 MPa. Regellastene var tilsvarende kapasitetene som ble beregnet fra de lineære analysene.

Restkapasitet ble beregnet ved å utføre ikke-lineære elementmetodeanalyser. Det ble laget et maksimalstyrkekriterie der permanent deformasjon midt på en stiver maksimalt kan være 0,5 % eller 1,0 % av stiverlengden. Ideen var å tillate deformasjoner som kan anses som akseptable og tøyningnivået var ved bruk av dette kriteriet være langt under materialkapasiteten. Skroget viste seg å ha en maksimalstyrke i området fra 1,5 til 3,6 ganger lasten ved første flyt, avhengig av lastfordeling. To grensebetingelser ble anvendt og de ga relativt like resultater.

Selv om skroget har stor restkapasitet etter første flyt, stilles det spørsmål ved om dette alene er nok for å tillate operasjon i tyngre isforhold enn det skipet var designet for. Islast større enn designlastene er forventet, så noe av restkapasiteten er allerede tatt med i beregningene av klassereglene. Det rapporteres jevnlig om skader på fartøy med isklasse, så den forenklete metoden som brukes i klasseregler har sine svakheter.

For videre arbeid anbefaler forfatteren å gjøre analyser med laster med ujevn trykkfordeling, hvilket er mer realistisk og konservativt. Det anbefales også å gjøre langtids fullskalamålinger. En fordelingsfunksjon kan tilpasses måledataene og en ny designlast

---

kan bestemmes ut fra en sannsynlighetstilnærming. Kapasitetene beregnet i denne oppgaven kan da sammenlignes med den nye designlasten og det kan avgjøres om fartøyet kan operere i tyngre isforhold enn det var konstruert for.



# Contents

<b>1</b>	<b>Introduction</b>	<b>1</b>
1.1	Background and Motivation . . . . .	1
1.2	Scope and Limitations . . . . .	2
<b>2</b>	<b>Properties of Ice</b>	<b>5</b>
2.1	Ice Features . . . . .	5
2.2	Mechanical Properties of Ice . . . . .	6
2.3	Pressure Distributions . . . . .	12
<b>3</b>	<b>Ice Class Rules</b>	<b>19</b>
<b>4</b>	<b>Numerical Models Representing Ice</b>	<b>23</b>
4.1	Plasticity Based Material Model for Ice . . . . .	23
4.2	Other Models . . . . .	27
4.3	Remarks on Material Models . . . . .	34
<b>5</b>	<b>Finite Element Analysis</b>	<b>35</b>
5.1	Linear Finite Element Analysis . . . . .	38
5.2	Nonlinear Structural Analysis . . . . .	39
5.2.1	Solution Schemes . . . . .	43
5.2.2	Tensor Analysis . . . . .	47
5.3	Finite Element Model of Ship Hull . . . . .	49
5.3.1	Elements . . . . .	54
5.3.2	Mesh Convergence Study . . . . .	55
<b>6</b>	<b>Analyses and Results</b>	<b>61</b>
6.1	Linear Analyses . . . . .	66
6.2	Nonlinear Analyses . . . . .	71
6.2.1	Load-Displacement Curves . . . . .	71
6.2.2	Ultimate Strength . . . . .	75
6.3	Rule Design Loads . . . . .	77
<b>7</b>	<b>Discussions</b>	<b>83</b>
7.1	Finite Element Model . . . . .	83
7.2	Loads . . . . .	85
7.3	Solution Scheme and Procedure . . . . .	86
7.4	Results . . . . .	86
<b>8</b>	<b>Conclusions</b>	<b>89</b>
<b>9</b>	<b>Recommendations for Future Work</b>	<b>91</b>
	<b>References</b>	<b>93</b>
	<b>Appendices</b>	<b>A.1</b>
<b>A</b>	<b>Python Scripts</b>	<b>A.3</b>
A.1	Create Input Files (Linear Analyses) . . . . .	A.3

A.2	Write Data to File (Linear Analyses) . . . . .	A.5
A.3	Create Input Files (Nonlinear Analyses) . . . . .	A.10
A.4	Write Load-Displacement Data to File (Nonlinear Analyses) . . . . .	A.12
A.5	Write Detailed Load-Displacement and Shear Data to File (Nonlinear Analyses) . . . . .	A.16
A.6	Calculate Rule Design Loads . . . . .	A.22
<b>B</b>	<b>Mesh Details</b>	<b>A.25</b>
<b>C</b>	<b>Additional Results</b>	<b>A.27</b>
C.1	Verification of Stress Distributions along Paths . . . . .	A.27
C.2	Ultimate Strengths in Numbers . . . . .	A.28
<b>D</b>	<b>Electronic Attachments</b>	<b>A.29</b>
D.1	Excel-sheet with Results from Linear Analyses . . . . .	A.30

## List of Figures

2.1	Example of a first-year sea ice ridge in the Barents Sea 2005 (Høyland, 2015).	6
2.2	Iceberg shapes (MANICE., 2005).	7
2.3	Experimental data showing a decrease in strength for increasing porosity (G. W. Timco & Frederking, 1986).	7
2.4	Experimental data showing a decrease in Young's modulus for increasing porosity (Langleben & Pounder, 1961).	8
2.5	Experimental data showing compressive strengths for different strain rates of freshwater ice (Gold & of Building Research, 1977).	9
2.6	Strain rate and temperature dependency of compressive strength of sea ice based on experimental data (G. Timco & Weeks, 2010). The ice surface is assumed to have the same temperature as the air.	9
2.7	Illustration of ductile to brittle transition as a function of strain rates with schematic stress strain curves (Schulson & Duval, 2009, ch. 11).	10
2.8	Increasing compressive strength for increasing strain rate (Schulson & Duval, 2009, ch. 11).	10
2.9	Brittle compression strength of unconfined fresh-water ice (Schulson & Duval, 2009, ch. 11).	11
2.10	Yield stress envelopes for columnar and granular sea- and freshwater ice in a plane stress state (G. W. Timco & Frederking, 1984).	12
2.11	Pressure contours showing spatial variation at interface during indentation of sea ice (Sodhi, Takeuchi, Nakazawa, Akagawa, & Saeki, 1998).	13
2.12	Reproduction on surface profile after indentation test. The "line"-profile is clearly visible (Tuhkuri, 1995).	14
2.13	Example of line-load experienced during indentation, red indicating high pressure and white zero (Erceg, Taylor, & Ehlers, 2015).	14
2.14	Contact ratio versus strain rate (Takeuchi et al., 2000).	14
2.15	Wide interaction area seen from side (I. J. Jordaan, 2001).	15
2.16	Wide interaction area seen on impacted area (I. J. Jordaan, 2001).	16
2.17	Pressure distribution on icebreaker hull during impact with bergy bit of 1900t. The size is approximately 2.4 m × 2.0 m (Ritch, Frederking, Johnston, Browne, & Ralph, 2008).	16
3.1	Energy dissipation for strength, ductile and shared-energy design (NORSOK, 2004b).	21
4.1	Failure strain as a function of hydrostatic pressure (Liu, Amdahl, & Løset, 2011).	24
4.2	Representation of yield surfaces for different parameters (Liu et al., 2011).	25
4.3	Recorded maximum pressures for different set of parameters (Table 2) (Liu et al., 2011).	26
4.4	Pressure versus nominal area relation for numerical results versus experimental data (Liu et al., 2011).	27
4.5	Numerical simulation of conical shaped iceberg impacting wall (Liu et al., 2011).	28

4.6	Example of pressure distribution on wall during impact with conical shaped iceberg (Liu et al., 2011). . . . .	28
4.7	FEM model of iceberg impacting rigid wall (Ferrari, Rizzuto, & Prestileo, 2015). . . . .	29
4.8	Contact pressures from initial contact (Ferrari et al., 2015). . . . .	29
4.9	Eroded iceberg at end of impact analysis (Ferrari et al., 2015). . . . .	30
4.10	Pressure contour of iceberg colliding with rigid wall, Liu's material model. Units are mm and MPa. (Storheim, Kim, Amdahl, & Ehlers, 2012). . . . .	30
4.11	Pressure area relation of two of Gagnon's crushable foam models and the plasticity based model by Liu (Storheim et al., 2012). . . . .	31
4.12	Pressure contour of iceberg colliding with rigid wall, Gagnon's 2011 model. Units are mm and MPa (Storheim et al., 2012). . . . .	32
4.13	Deformation plot of impact between iceberg and deformable vessel. Gagnon's two models are on the left, Liu's on the right (Storheim et al., 2012). . . . .	32
5.1	A continuous mechanical problem discretized into finite elements and nodes. Element numbers are in parentheses. Global system with global node numbers is depicted in the upper right part. Local degree of freedoms are seen for element (3) in the bottom part (Hopperstad & Børvik, 2014). . . . .	36
5.2	Material nonlinearity. . . . .	40
5.3	Geometrical nonlinearity. . . . .	41
5.4	Geometrical nonlinearity. Snap-through: Instability occurs as the limit point is passed and the stiffness becomes negative. Stability is reached after "snapping through", and there is a following change from compression to tension in the rods. . . . .	42
5.5	Nonlinearity due to boundary conditions and contact. When the right part of bar comes in contact with the wall, the stiffness increases. Load deformation curve is seen to the right. . . . .	42
5.6	Illustration of the Newton-Raphson method (Hopperstad & Børvik, 2014). . . . .	45
5.7	Illustration of the modified Riks method (Memon & Su, 2004). . . . .	46
5.8	A body in undeformed ( $B$ ) and current ( $\varphi(B)$ ) configuration (Wriggers, 2008). . . . .	47
5.9	Body transformation according to Equation (5.32). The undeformed body is marked with the continuous blue line and the current configuration in blue dashed line. $E_i$ and $e_i$ are axes in material and current configuration. . . . .	48
5.10	Overview of FE model. . . . .	50
5.11	The gray box marks the location of the FE model. Outline is based on hull drawings. . . . .	50
5.12	Approximate length of stiffeners, taken as the distance between the midpoint of the web at both ends. . . . .	51
5.13	Cross section of stiffeners and hull skin. Dimensions corresponding to this figure are found in Table 4. . . . .	51
5.14	Material model for AH-36 and NV-NS steels. . . . .	53

5.15	FE model used for mesh convergence study. The loaded surface is marked in red. Three elements over the web height are used in this example. . . . .	56
5.16	FE model used for mesh convergence study. The yellow ellipse marks the location where stresses were extracted and the white ellipse marks the location where displacements were extracted (in direction of z). . . . .	57
5.17	Mesh convergence with a 5 MPa load. S4R and S4 elements were assessed. . . . .	58
5.18	Mesh convergence with a 6.25 MPa load. S4R elements were assessed. . . . .	59
6.1	Examples of resulting deformations for increasing load patch width, obtained from linear analyses and presented with a large deformation scale factor. Load patches are marked in red. More stiffeners are activated as the load patch width increases. . . . .	62
6.2	"All fixed" boundary conditions. Orange arrowheads indicate that translational DOFs are fixed in the direction of the arrow; blue double arrowheads indicate that rotational DOFs are fixed around the axis of the arrow. . . . .	64
6.3	"Partly fixed" boundary conditions. Orange arrowheads indicate that translational DOFs are fixed in the direction of the arrow. . . . .	65
6.4	Illustration of stress distribution in a stiffener at midspan. Higher stress values are marked in red and it is seen that the web covers the regions with the highest values. . . . .	67
6.5	Local coordinate systems are marked in yellow and the upper path for stress extraction on stiffener L1 is marked in red. . . . .	68
6.6	Local bending action in web due to lateral deformation of stiffeners. . . . .	69
6.7	Shell element with rendered thickness ( $t_{element}$ ). Section integration points are marked with blue crosses, and the dashed crosses indicate that data for these section points were not written to the result files. Using value at mid-section point will exclude the bending contribution $\sigma_{bending}$ , leaving only the membrane stress, $\sigma_{membrane}$ . . . . .	69
6.8	Load capacity as a function of load patch width. First yield is used as failure criterion. . . . .	70
6.9	Deformation is measured at the center of the load (origin in the coordinate system CSYS-L2-plate-fixed), in the direction of the load (z-axis of CSYS-L2-plate-fixed). Note the plastic hinges at the midspan and at the lower end of the load, marked in light gray. . . . .	72
6.10	Load-displacement curves for large deformations. . . . .	73
6.11	Load-displacement curves at onset of yielding. Reaction force on the second axis. . . . .	73
6.12	Load-displacement curves at onset of yielding. Pressure load on the second axis. . . . .	74
6.13	Load-displacement and "load-load" curves for large deformations. . . . .	75
6.14	Load-displacement and "load-load" curves showing load carrying distribution for the three central stiffeners for an increasing load width. . . . .	76

6.15	Procedure for obtaining capacities. $\Lambda$ represents load, $\delta$ represents displacement and the dots represent data points. Create a tangent to the load-displacement curve based on the origin and the first data point $(\delta_1, \Lambda_1)$ . Parallel shift the tangent curve so that it crosses the x-axis at the allowable permanent deformation $(\delta_{permanent})$ . The capacity $(\Lambda_{capacity})$ is found from the intersection of the two curves.	77
6.16	Example of "unloading-curves" along with load-displacement curve used for obtaining capacities. . . . .	78
6.17	Ultimate and linear capacity a function of load patch width. . . . .	79
6.18	Illustration of residual strength, taken as the nonlinear capacity divided by the linear capacity. . . . .	80
6.19	Ultimate capacity, linear capacity and rule design load as a function of load patch width. . . . .	81
B.1	Mesh details, decks. . . . .	A.25
B.2	Mesh details, stiffeners. . . . .	A.26
C.1	Example of stress distribution along a path (cross section) at the lower end of a stiffener. . . . .	A.27
D.1	Snip of the Excel-sheet displaying data from the linear analyses. . . .	A.30

---

## List of Tables

1	Key properties of ice relevant for ship-ice impacts. . . . .	17
2	Input parameters for yield surfaces. . . . .	25
3	Overview of vessel's main characteristics. . . . .	49
4	Scantling data (see Figure 5.12 and 5.13 for explanations). . . . .	49
5	Material constants. . . . .	53
6	Hardening rule. . . . .	53
7	Load patch dimensions . . . . .	61
8	Ultimate strengths from nonlinear analyses. "whole model", "all fixed".	A.28
9	Ultimate strengths from nonlinear analyses. "half model", "partly fixed". . . . .	A.28





# Nomenclature

## Abbreviations

H	Load patch height, z-component
W	Load patch width, x-component
ALS	Accidental Limit State
BC	Boundary Condition
DOF	Degree Of Freedom
FE	Finite Element
FEA	Finite Element Analysis (linear)
FEM	Finite element method
FSICR	The Finnish-Swedish Ice Class Rules
IACS	International Association of Classification Societies
ISO	International Organization for Standardization
LPF	Load Proportionality Factor
NLFEA	Nonlinear finite element analysis
NTNU	The Norwegian University of Science and Technology
PVW	Principle of virtual work
SLS	Serviceability Limit State
TUHH	Hamburg University of Technology
ULS	Ultimate Limit State

## Symbols

$\sigma'$	Deviatoric stress tensor	
$\sigma$	Stress tensor	
$\varepsilon^p$	Plastic strain tensor	
$\Delta R$	Load increment	
$\Delta r$	Displacement increment	
$\delta$	Symbol indicating virtual, Section 5	
$\Delta_f$	Displacement of vessel	[Mg] (tonnes)
$\delta_{ij}$	Kronecker delta	
$\ell_0$	Initial load patch width, see Section 3	[m]
$\ell_a$	Load patch width or stiffener spacing	[m]

$\epsilon$	Tolerance	
$\eta_Y$	Utilization (first yield)	[-]
$\Delta$	Differential operator	
$\mathbf{a}_e$	Connectivity matrix	
$\mathbf{B}$	Strain-displacement matrix	
$\mathbf{b}$	Body forces	
$\mathbf{C}$	Elasticity matrix	
$\mathbf{C}$	Damping matrix	
$\mathbf{C}_{n+1}^{alg}$	Consistent tangent operator	
$\mathbf{E}$	Green-Lagrange strain tensor	
$\mathbf{F}$	Deformation gradient	
$\mathbf{G}$	Residual nodal force vector	
$\mathbf{H}$	Displacement gradient	
$\mathbf{I}$	Identity tensor	
$\mathbf{K}$	Global stiffness matrix	
$\mathbf{K}^t$	Tangent stiffness matrix	
$\mathbf{M}$	Mass matrix	
$\mathbf{N}$	Matrix containing shape functions for all elements	
$\mathbf{N}_e$	Elemental interpolation functions	
$\mathbf{r}$	Global nodal displacements	
$\mathbf{R}^{ext}$	External nodal forces	
$\mathbf{R}^{int}$	Internal nodal forces	
$\mathbf{t}$	Traction forces	
$\mathbf{u}(\mathbf{x}, t)$	Displacement field	
$\mathbf{v}_e$	Element nodal displacement vector	
$\mathbf{X}$	Position vector in material configuration	
$\mathbf{x}$	Position vector	
$\nu$	Poisson's ratio	
$\sigma_Y$	Yield stress	
$\sigma_{eq}$	Equivalent stress	
$\sigma_{ij}$	Component of the stress tensor	
$\sigma_{max}$	Max stress ( <b>Mises</b> or <b>S11</b> ) over path	

---

$\tau_Y$	Yield stress in shear. $\tau_Y = \frac{\sigma_Y}{\sqrt{3}}$	
$\tau_{max}$	Max shear stress (S12) over path	
$\varepsilon_0$	Initial failure strain	
$\varepsilon_f$	Failure strain	
$\varepsilon_p$	Plastic strain	[-]
$\varepsilon_{acc}$	Accumulated plastic strain	
$\varepsilon_{eq}^p$	Equivalent plastic strain	[-]
$\varepsilon_{ij}^p$	Component of the plastic strain tensor	[-]
$a_0, a_1$ and $a_2$	See Section 4.1	
$a_1, b_1, c_1, c_a, c_d$ and $k_1$	See Section 3	
$C_Y$	Capacity (first yield)	
$E$	Young's modulus	
$E_t$	Tangent modulus	
$f$	Yielding function	
$H$	Hardening variable	
$h$	Design ice height	[m]
$h_0$	Level ice thickness	[m]
$i$	Iteration number	
$J_2$	Second invariant of the deviatoric stress tensor	
$n$	Increment number	
$P$	Nominal ice pressure	[MPa]
$p$	Hydrostatic pressure	
$p_2$	Melting pressure	
$P_{min}$	Engine power	[kW]
$R$	Load	
$r$	Displacement	
$S$	Surface of body	
$t$	Time	
$V$	Volume of structure	
$V_e$	Volume of element	



# 1 Introduction

Winter navigation started in the 19<sup>th</sup> century when the first ships got steam and diesel propulsion systems. In the beginning, ice strengthened ships and ice breakers were only able to extend the summer season, but as the technology evolved and experience was gained all year operation became a reality. With increased winter navigation came the need for regulations for the structures and for operations. These regulations have been revised over and over again as insight and experience on loading and damages have been gained (Riska & Kämäräinen, 2011). Ice loading can be severe and there are numerous examples of structures critically damaged due to ice loading (Marchenko, 2014). Design rule requirements have been made to prevent such damages, but at the same time there is a trade off between safety and costs. Class notations only use a single design point at first yield, and limited information on post-yielding response and ultimate strength of hulls is therefore available. Damages are at the same time accepted to some extent, and that is a challenge. Marine operation in ice infested waters is expected to increase and the frequency of reported damages is already high, so information on the post-yielding response of ship hulls exposed to ice loading is of interest for ship owners and classification societies.

## 1.1 Background and Motivation

In an ongoing project between DNV GL and a customer is the goal to assess whether a given vessel can operate in more severe ice conditions than it was initially designed for. Many factors have to be looked into in such an assessment, and among them are the hull strength and ice loads during operation. Full scale measurements using strain gauges are scheduled for the upcoming winter season, and to be able to use this data it is crucial to know the hull response during different loading scenarios. Information of the loads experienced by the hull can in this way be traced back from the strain data.

The philosophy behind the structural design of ships and offshore structures is often based on *limit state design* (NORSOK, 2004a). Different structural functions are required to be fulfilled in different scenarios. For a scenario with high probability of occurrence, high functionality of the structure is demanded, while for events with a low possibility of occurrence only the most fundamental functions of the structure are to be fulfilled. As an example, the Serviceability Limit State (SLS) would require that an oil-rig should be able to continue production at normal rate for weather conditions experienced "on daily basis". In an Accidental Limit State (ALS) scenario, which has an annual probability of exceedance of  $10^{-4}$ , the only requirement would be that a catastrophic failure should not occur. Permanent deformations, heavy vibrations and large displacements of the structure would then be allowed. Because of a weather dependency, these requirements are location specific for offshore structures.

For ships, however, ALS is not explicitly implemented in the design requirements for the structural resistance. There are requirements for double hull and watertight compartments, instead of requirements linked to events such as groundings or collisions. An Ultimate Limit State (ULS) design philosophy is implemented and ships

operating in open water are typically designed to withstand a North Atlantic 25-year wave<sup>1</sup>, no matter where the ship is operating (for DNV GL class rules). Even though a ship operates in an area with smaller loads and waves statistically, the requirements would be the same as for a ship operating in harsh conditions all year around. For ice going vessels, however, the structural requirements depend on the location of planned operation, the ice conditions during operation and on travel time in ice (*DNV GL rules for classification: Ships (RU-SHIP)*, 2016). This means that ships operating in ice on daily basis have other requirements than ships operating in the same ice conditions only once a year. It is the responsibility of the vessel operator to ensure that ice conditions are according to the class notation, and that is by no means an easy task. There are few ways of knowing the ice thickness without doing measurements. Snow on top of the ice can hide features, and deep ice ridges can be present with only minor changes on the surface, not to mention the varying ice strength. Even if conditions are found to be too harsh, it is not necessarily easy to just "drive away". Another factor which can increase the risk of misjudgments is lack of experience in winter navigation among operators and crew. Numerous examples of damages on ice class vessel have been reported, even though they apparently have been operated in conditions according to its class notations (Kujala & Ehlers, 2013; Storheim, 2016). Also ice breakers, which are designed to withstand repeated ice loading of the worst kind, have been prone to severe damages (Marchenko, 2014).

It is evident that the probability of experiencing loads exceeding the design values is higher for vessels operating in ice than for vessels operating in open water. Still, there is no requirement on residual strength after yielding. What will be the consequences if a vessel operator misjudges the ice conditions? Will a catastrophic failure occur, or can the ship take the additional loading? These questions are rarely assessed in design of an ice class vessel, in spite of the relatively high probability of exceeding design loads. It is therefore of great interest for DNV GL to get an insight in the response of a ship hull loaded above the design load and to determine the residual strength.

## 1.2 Scope and Limitations

The structural response of a DNV GL classified ship exposed to different loads will be assessed in this thesis.

In order to get an understanding of the behavior of ice and what happens when a structure and ice interact, detailed information on the material properties of ice will be introduced to begin with. Numerical models and analysis methods relevant for assessing ship-ice interactions will be presented, even though there will not be time to implement one of these methods in the analyses. Ice class rules philosophy and design loads will be introduced.

Some parts of the underlying theory behind the finite element method will be presented. Different types of nonlinearities will be explained, and relevant solution schemes, elements and material models used in the finite element method will be in-

---

<sup>1</sup>A 25-year wave is a wave with a return period of 25 years.

roduced. The finite element model of the hull used in the analyses will be presented. Local loads will be assessed so only a part of the starboard bow will be analyzed.

Procedures and loads used in the different analyses and the results obtained will be presented. Different loads and boundary conditions shall be assessed and rule design loads shall also be calculated. As time is limited, only uniform loads will be looked into. Both linear and quasi-static nonlinear analyses will be done, and the ultimate strength for different load cases based on a self made criterion shall be obtained. Results and procedures, along with applied boundary conditions shall be discussed.

Conclusions and recommendations for further work will be made at the end of the thesis. Scripts and other non-essential information shall be included in the appendices.

Readers are expected to have knowledge within the field of structural engineering on graduate level, and having knowledge within marine engineering is an advantage.

#### Note

The identity of the ship is kept confidential upon request by DNV GL. No drawings or ship documents will be presented for that reason. The Abaqus .cae-file could not be distributed, but the finite element models used are attached electronically through Abaqus input files (`Job-LoadPatch-W0-H0-nonames.inp`) (Appendix D). Sensitive names have been changed so that the scripts attached (Appendix A) may not work with the given input-files.

#### Note

The author wrote a project thesis on material properties for ice and on numerical models for representing ice last autumn (Mork, 2015). At that time, the topic of the master thesis was planned to be on ship-iceberg impacts and the project thesis was written with that in mind. Later the intended supervisor at DNV GL quit, and the topic for this master thesis had to be changed. In spite of this, parts of the project thesis are still relevant. Section 2 and 4 have been taken from the project thesis (Mork, 2015), but minor changes, removals and additions have been made where necessary.





## 2 Properties of Ice

### 2.1 Ice Features

It is common to divide ice into different classes such as first year, second year and multiyear ice, sea ice, freshwater ice and iceberg ice (MANICE., 2005). Iceberg ice is glacial ice that has drifted off to sea and its properties are somewhat different from those of sea ice. Glacier ice is formed when snow is compressed under its own weight over long periods of time. Sintering and creep gradually solidify the snow, such that polycrystalline, granular ice is formed. The crystals' c-axis is for "young" glacial ice orienting in random directions, making the ice isotropic (G. Timco & Weeks, 2010). However, the structure changes over time, and some preferential orientation of the c-axis develop (Schulson & Duval, 2009, p. 30). Still, iceberg ice was by T. J. Sanderson (1988) considered as an isotropic material, and this simplifying consideration have been adopted by others (Ferrari et al., 2015; Liu et al., 2011). More on glacial ice formation can be found in *Creep and Fracture of Ice* (Schulson & Duval, 2009, ch. 3).

Sea ice is formed when the temperature is sufficiently low for a long period of time and there is limited movement in the sea. The top layer consists of smaller crystals orienting in random directions. For further growth, the crystals' c-axis will be aligned, making the ice anisotropic. Due to movement of the ice sheet, ice ridges may be formed. As two layers of ice are pushed towards another, the ice sheet will break in smaller parts and pile up in a so-called ice rubble. An example of an ice ridge seen from above is found in Figure 2.1. The keel depth of ice ridges have been measured up 50 meters (Høyland, 2015). Still, the sail height usually is only a fraction of the depth, making them hard to detect. When the ice rubble freezes, a consolidated layer is formed. This layer may be several times thicker than the surrounding ice (Høyland, 2015). Passing heavy ice ridges may require repeated ramming, and even ice breakers do in special cases need to keep on ramming for hours at a time only to advance a ship length (Sawhill, n.d.). Ice hammocks are ridges localized around a point instead of an line, making them less of a problem to avoid if detected. Rafted ice is level ice that is pushed on top of another layer of level ice. Though ice ridges can be more severe, operating in rafted ice will in general increase loads and friction resistance significantly.

Iceberg size varies from thousands of square kilometers to smaller ones covering only some square meters (MANICE., 2005). When calved off from a glacier, they can take on many different shapes (Figure 2.2). Sharp edges and irregular shapes are common, and melting, turning and breaking make the icebergs change shape during their lifetime. Icebergs are in general inhomogeneous with respect to mechanical properties (Storheim et al., 2012). The temperature distribution in icebergs is characterized by a temperature gradient from the surface to a thickness of approximately 3 meters while central parts hold a more or less constant temperature (Løset, 1993). Impurities may be present in the ice, also affecting the inhomogeneity.



Figure 2.1: Example of a first-year sea ice ridge in the Barents Sea 2005 (Høyland, 2015).

## 2.2 Mechanical Properties of Ice

Since the behavior of ice is dependent on many parameters, it is not straight forward to state its mechanical properties. An attempt to present some of the more important properties and dependencies with respect to engineering problems follows.

The density of iceberg ice varies between  $600 \frac{\text{kg}}{\text{m}^3}$  for firm to about  $920 \frac{\text{kg}}{\text{m}^3}$  (Schulson & Duval, 2009, p. 25). Sea ice is filled with saltwater pockets and may therefore have a higher density. For freshwater ice, brine pockets or channels will not be present, but air pockets will (Schulson & Duval, 2009, ch. 3). As Figure 2.3 and 2.4 illustrate, the strength and Young's modulus decrease with increasing porosity (G. Timco & Weeks, 2010; Schulson & Duval, 2009). To be on the conservative side, it may be argued that properties of low porosity, high density ice should be used for design purposes if other information is not available. In that case the Young's modulus will be in the range 9-10 GPa and the density approximately  $900 \frac{\text{kg}}{\text{m}^3}$ . Sea water ice will in general be somewhat denser and have a slightly smaller Young's modulus. These properties depend on other parameters as well, so care should be taken when stating general values.

Ice behaves elastically, plastically and viscously. Arakawa and Maeno (1997) measured the maximum tangent modulus of fresh-water ice deformed with a strain rate of  $10^{-4} \text{s}^{-1}$  to be only a seventh of the Young's modulus, which illustrates how big the influence of viscosity is. Mechanical properties such as tensile and compression strength are strongly dependent on the strain rate (Schulson & Duval, 2009; G. Timco & Weeks, 2010; Gold & of Building Research, 1977). Figure 2.5 and 2.6 show that the compressive strength is a strong function of the strain rate, and that ice exhibits strain rate hardening. For a strain rate,  $\dot{\epsilon}$ , larger than approximately  $10^{-3} \text{s}^{-1}$ , a slight strain rate softening is reported (Figure 2.5) (Schulson & Duval,




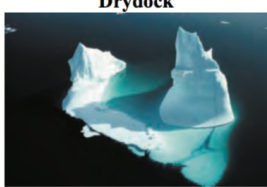



Shape	Average height to draft ratio	Shape	Average height to draft ratio
<b>Tabular</b> 	1:5	<b>Wedge</b> 	1:5
<b>Non-Tabular</b> 	1:5	<b>Drydock</b> 	1:1
<b>Domed</b> 	1:4	<b>Blocky</b> 	1:5
<b>Pinnacle</b> 	1:2		

Figure 2.2: Iceberg shapes (MANICE., 2005).

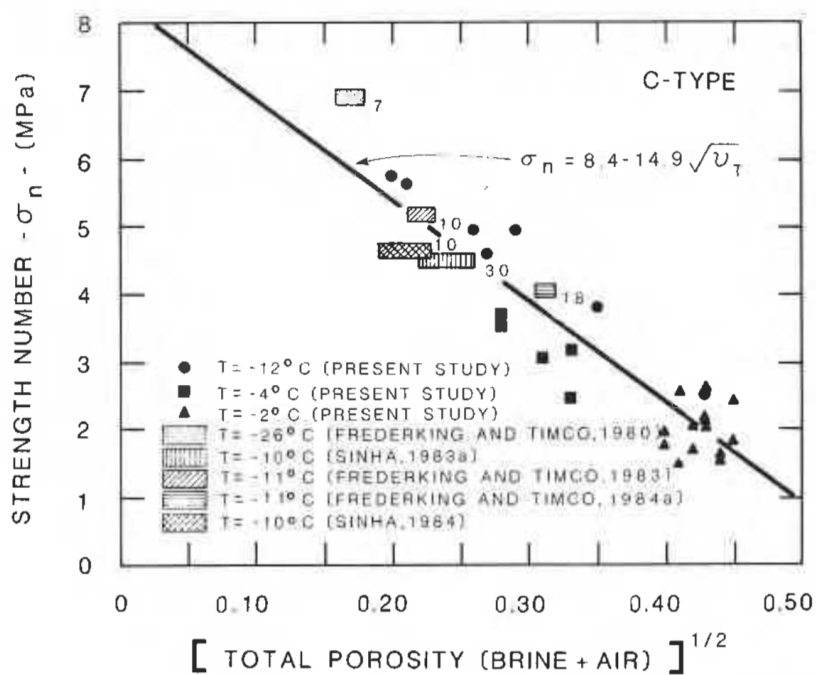


Figure 2.3: Experimental data showing a decrease in strength for increasing porosity (G. W. Timco & Frederking, 1986).

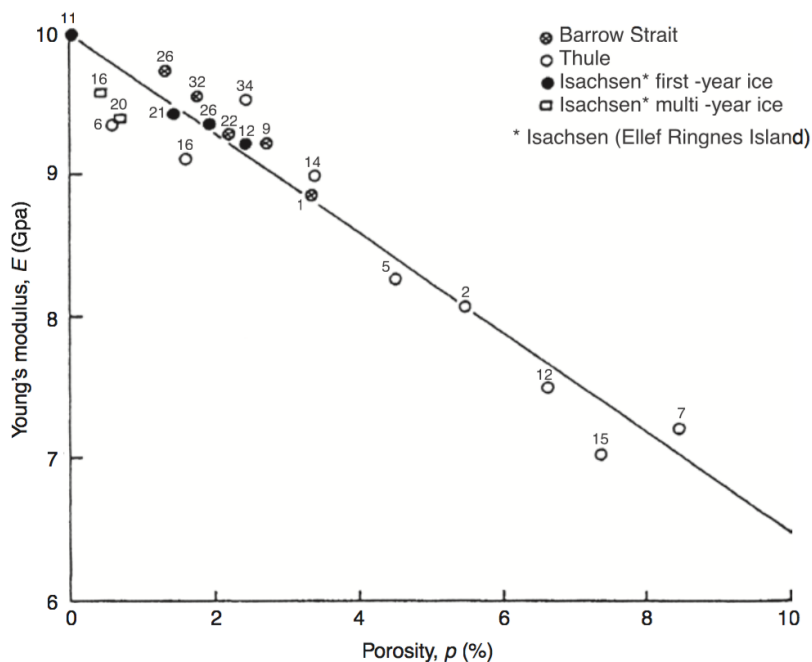


Figure 2.4: Experimental data showing a decrease in Young's modulus for increasing porosity (Langleben & Pounder, 1961).

2009, ch. 11.3). However, other data imply that there is continuous strain rate hardening also for high strain rates (Schulson & Duval, 2009, ch. 11.5), see Figure 2.8.

There is a transition between ductile and brittle behavior (Schulson & Duval, 2009; Gold & of Building Research, 1977), illustrated in Figure 2.7. At lower strain rates, creep and ductile behavior govern deformation. Strain-stress curves are smooth, and the ice experiences some strain softening and/or stress relaxation before failure. For brittle behavior at higher strain rates, the stress-strain curve is not as smooth and strain softening is not present before failure. Note that this is valid for unconfined ice, as confining pressures may cause a brittle to ductile transition (Schulson & Duval, 2009, p. 242). For high confining pressures, compression-failure will occur as *non-frictional* or *plastic* shear fault, in contrast to the *frictional* or *Coulombic* shear fault occurring for lower confining pressures (Schulson & Duval, 2009, p. 273). Plastic deformation happens mainly by gliding of dislocations in the basal plane, yielding greater strength than for Coulombic failure. Details on this can be found in *Creep and Fracture of Ice* (Schulson & Duval, 2009, p. 272). This explains why the compression strength is much higher for confined than for unconfined ice. Also, the sensitivity to hydrostatic pressure is much higher in the brittle regime than in the ductile, because high confining pressures may trigger plastic and more ductile behavior, in spite of high strain rates (Schulson & Duval, 2009).

Brittle behavior will typically dominate in higher speed impacts such as for a ship operating in ice, due to high strain rates. Fracturing, cracking, spalling, crushing and extrusion will then occur during deformation. Fracture toughness is an important factor for determining the amount of energy the ice can absorb. It increases with increasing density/decreasing porosity, making denser ice stronger. Many parameters influence the fracture toughness, which is explained in more detail by Schulson and

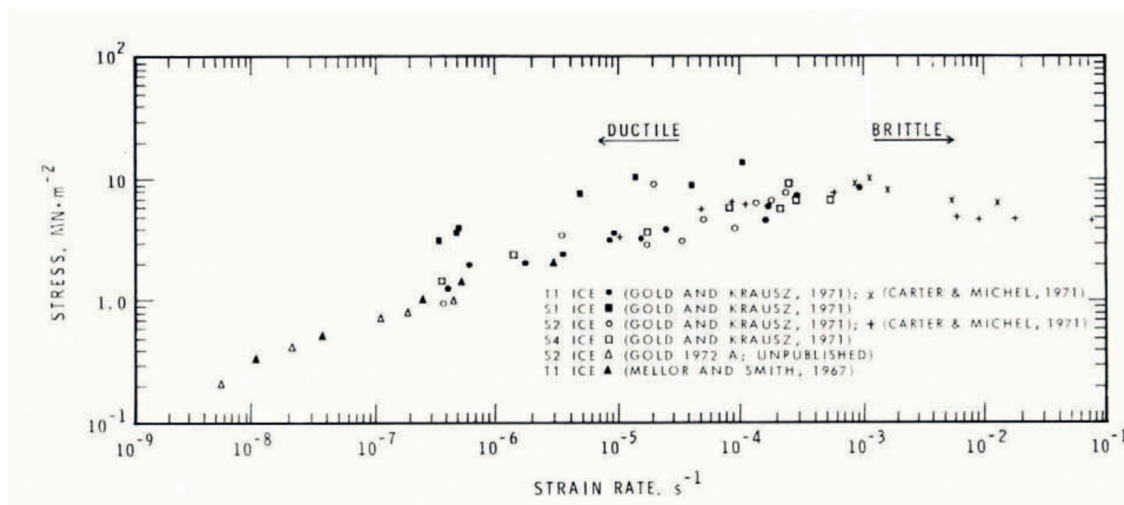


Figure 2.5: Experimental data showing compressive strengths for different strain rates of freshwater ice (Gold & of Building Research, 1977).

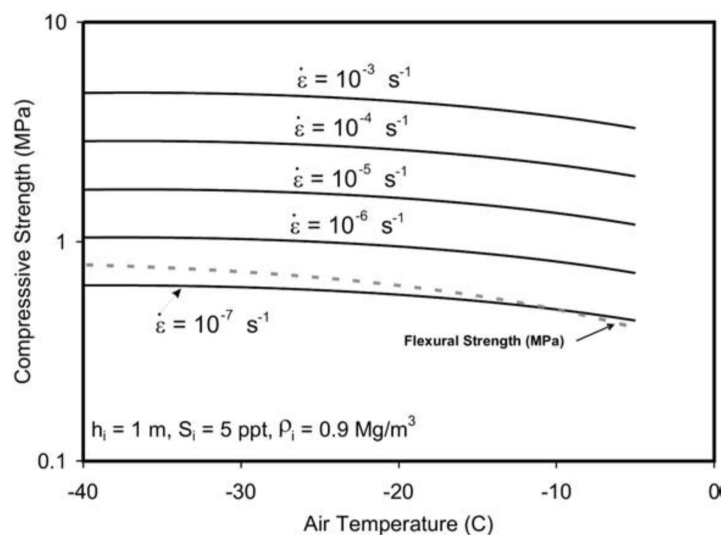


Figure 2.6: Strain rate and temperature dependency of compressive strength of sea ice based on experimental data (G. Timco & Weeks, 2010). The ice surface is assumed to have the same temperature as the air.



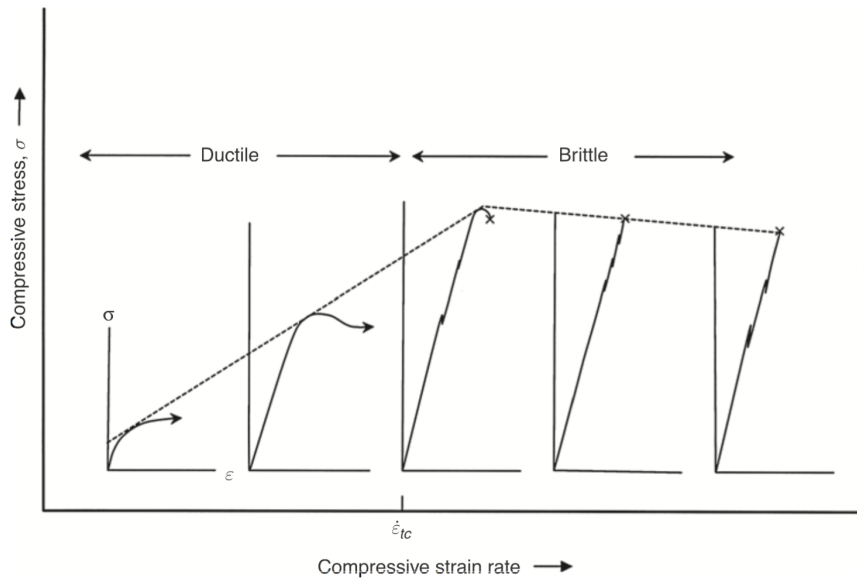


Figure 2.7: Illustration of ductile to brittle transition as a function of strain rates with schematic stress strain curves (Schulson & Duval, 2009, ch. 11).

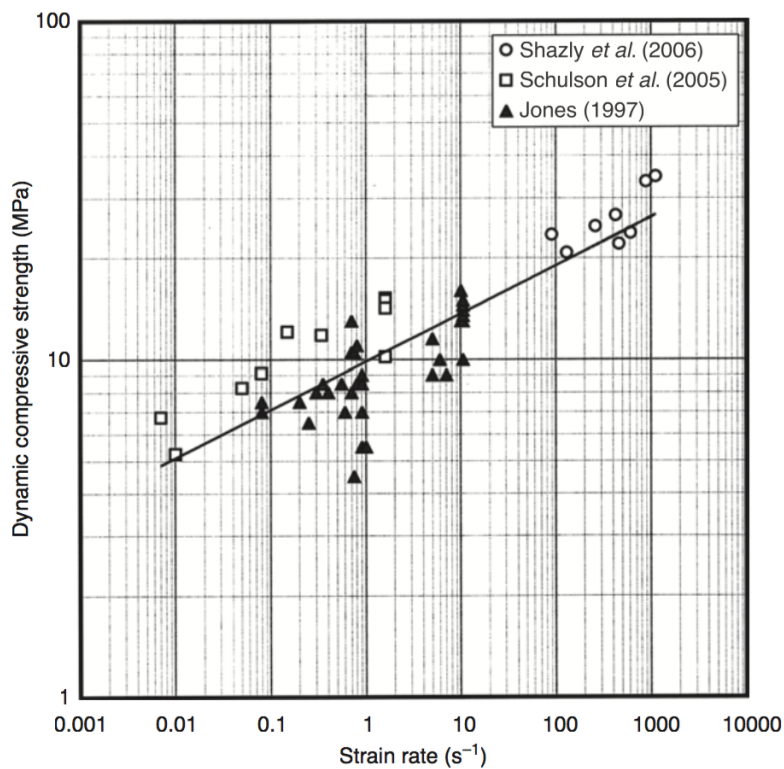


Figure 2.8: Increasing compressive strength for increasing strain rate (Schulson & Duval, 2009, ch. 11).

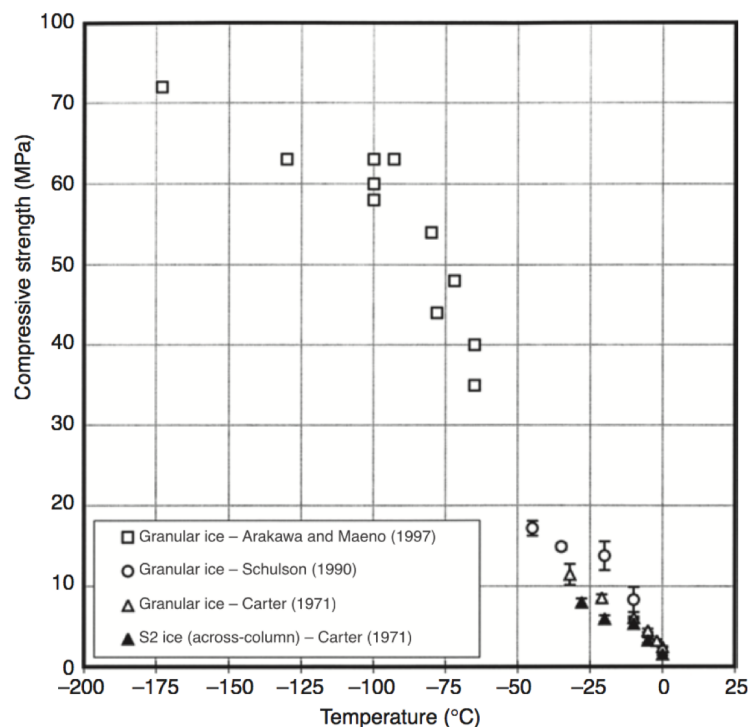


Figure 2.9: Brittle compression strength of unconfined fresh-water ice (Schulson & Duval, 2009, ch. 11).

Duval (2009, ch. 9). Cracking can cause pieces of different sizes to spall off from the main body. If pieces are not extruded away, further microcracking cause the ice to crush and powderize, before it eventually will be extruded away by high pressures. Crushing ice is energy demanding compared to spalling off bigger pieces.

Strength, elastic constants and other properties of ice are temperature dependent. With a temperature decrease from  $0^{\circ}\text{C}$  to  $-50^{\circ}\text{C}$  the stiffness, or any other fundamental elastic constant, increases only about 5 % (Schulson & Duval, 2009, p. 56) and with a temperature decrease from  $0^{\circ}\text{C}$  to  $-30^{\circ}\text{C}$ , the tensile strength of columnar-grained freshwater ice only increases 10 % (Schulson & Duval, 2009, p. 216). The strength curves in Figure 2.6 also indicate a rather low temperature dependency, especially when taking into account that salt-water ice exhibits greater thermal sensitivity than fresh-water ice (Weeks, 1962). On the other hand, the experimental data in Figure 2.9 show a more profound temperature dependency. It is not necessarily only the temperature at impact that matters, but the temperature history may also be of importance. Ice made at  $-50^{\circ}\text{C}$  may have different properties than ice frozen at  $-10^{\circ}\text{C}$  and then cooled to  $-50^{\circ}\text{C}$  right before an experiment. Generally, ice behaves more brittle (Erceg, Taylor, Ehlers, & Leira, 2014) and stiffness and strength increase somewhat with decreasing temperature, but there is some discrepancy on how big the influence is. The variation with strain rate is, anyways, much greater (G. Timco & Weeks, 2010).

Another parameter influencing the strength of ice is the confinement level. Note that "confinement level", "confinement pressure" and "hydrostatic pressure" all have the

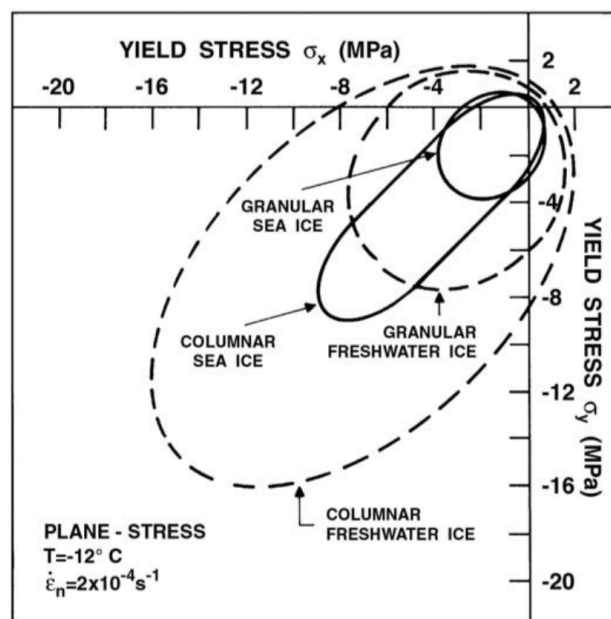


Figure 2.10: Yield stress envelopes for columnar and granular sea- and freshwater ice in a plane stress state (G. W. Timco & Frederking, 1984).

same meaning in this thesis. Geometry of both ice and structure during an impact influence the confining pressure. For ultimate strength tests of unconfined polycrystalline freshwater ice with a strain rate of  $10^{-3} \text{ s}^{-1}$ , typical maximum pressures measured are in the region of 10 MPa (Schulson & Duval, 2009, ch. 11). For tests conducted with samples of confined ice, the maximum pressures measured are many times as large. Local pressures over 70 MPa have been measured during impacts (I. J. Jordaan, 2001). The reason for this difference is that parts can easily break off/spall and cracks can propagate in the unconfined tests, but for confined samples these failure modes are not induced. Instead, plastic deformations, crushing and recrystallization take place (I. J. Jordaan, 2001), which are modes yielding larger strengths. Daley, Tuhkuri, and Riska (1998) emphasized the importance of crushed ice in ice-structure interaction: Both total force and confining pressures increase with the presence of crushed ice at the interface. The strength of ice is dependent on the crystal structure. Granular ice, which can be considered isotropic, is in general weaker than columnar or single crystal ice, which is anisotropic. Examples of different yield envelopes are shown in Figure 2.10. Tensile strength of ice is in general only a fraction of the compressive strength, also seen in the figure. The tensile strength is typically around 1-2 MPa for granular fresh-water ice and slightly less for sea ice (Schulson & Duval, 2009, p. 215).

### 2.3 Pressure Distributions

A ship-ice impact scenario is typically governed by relatively high impact velocities and thus strain rates. Experiments have shown that the pressure distribution during an ice-impact is highly nonuniform. Due to spalling and extrusion, some parts of



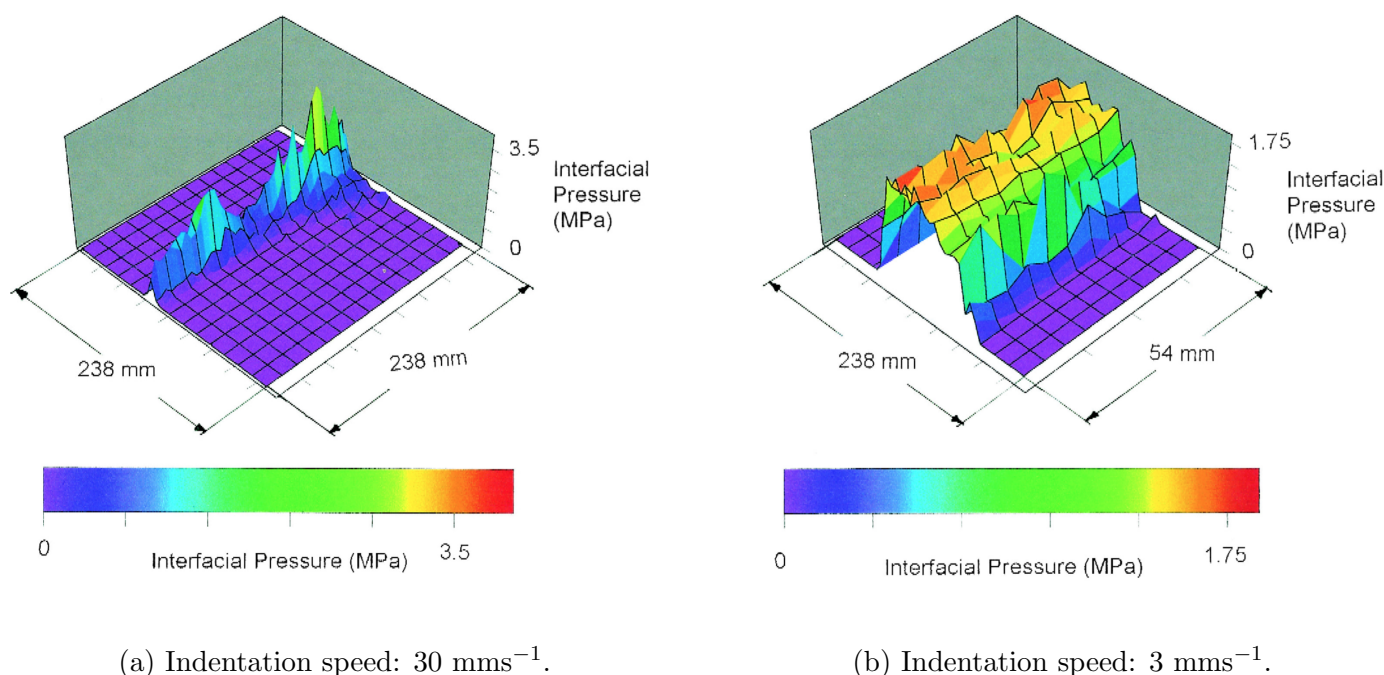
(a) Indentation speed:  $30 \text{ mms}^{-1}$ .(b) Indentation speed:  $3 \text{ mms}^{-1}$ .

Figure 2.11: Pressure contours showing spatial variation at interface during indentation of sea ice (Sodhi et al., 1998).

the projected contact area do not come in contact with the ice at all. Other areas, so-called *high pressure zones*, are subjected to very high local pressures which can reach over 70 MPa due to the high confinement pressures. On the outskirts of these high pressure zones pressures are significantly lower. Crushed and powderized ice extrudes through areas of low or zero pressure during impact. The contour of the high pressure zone for higher speed impacts between ice and a rigid wall typically forms a "line-like" load. This has been observed mostly on small to medium scale tests, but also in full-scale icebreaker measurements (Riska, Rantala, & Joensuu, 1990). The "line" is constantly changing shape and position as cracks develop, parts break off and crushing occurs, but will tend to lie near the center of the impact area where confinement is high (Figure 2.12). Figure 2.13 and 2.11a show typical line-like pressure distributions. At very low indentation speeds, and thus low strain rates, the pressure distributes more evenly because of ductile and creep behavior. This is shown in the difference in load patterns in Figure 2.11, where the indenter is moving at different speeds. The higher the strain rate, the more nonuniform and the more concentrated the high pressure zone will be, which experimental data in Figure 2.14 indicate: The contact ratio decreases for increasing strain rates. Another phenomenon occurring during medium strain rate indentation tests, is a surprisingly regular load fluctuation. As fracturing and flaking happens, load is relieved before building up again, producing a sawtooth-like force-time curve (I. J. Jordaan, 2001). For higher strain rates, on the other hand, there is evidence for a more continuous crushing with less sign of an oscillating load (I. J. Jordaan, 2001).

Several icebreakers have been equipped with pressure sensors or strain gauges on their hull, obtaining valuable data regarding the pressure versus contact area relation

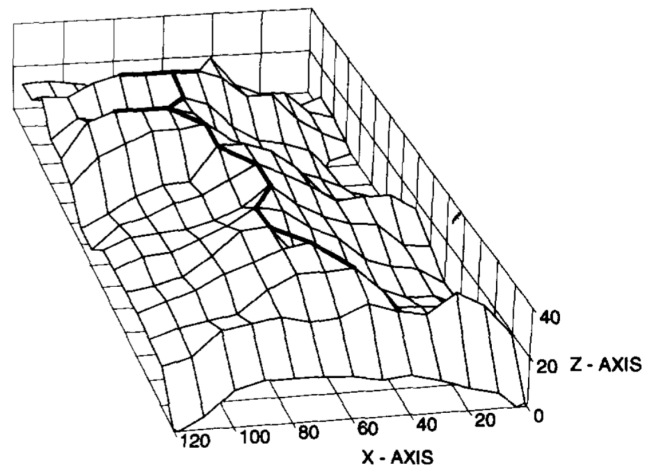


Figure 2.12: Reproduction on surface profile after indentation test. The "line"-profile is clearly visible (Tuhkuri, 1995).

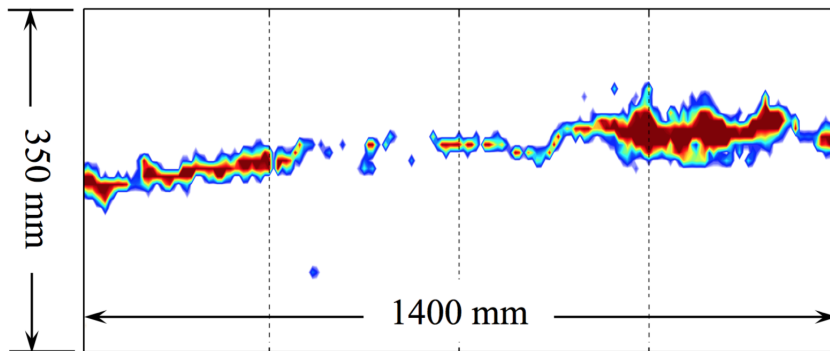


Figure 2.13: Example of line-load experienced during indentation, red indicating high pressure and white zero (Erceg et al., 2015).

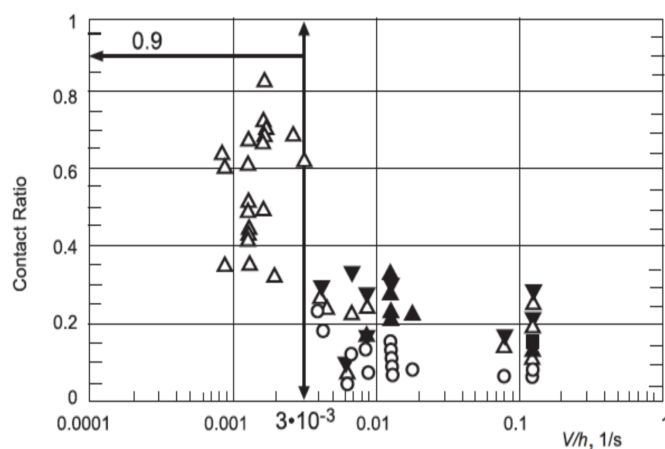


Figure 2.14: Contact ratio versus strain rate (Takeuchi et al., 2000).

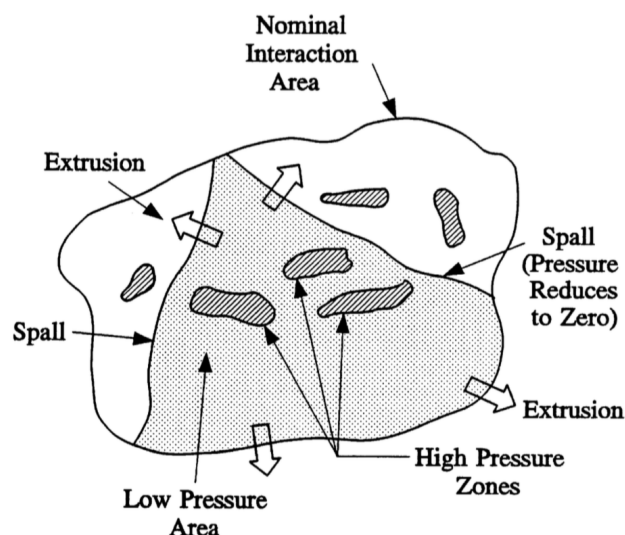


Figure 2.15: Wide interaction area seen from side (I. J. Jordaan, 2001).

during ramming (I. Jordaan, Li, Sudom, Stuckey, & Ralph, 2005). The data show that the average pressure is decreasing with increasing nominal contact area and this relation has been found in a variety of full-scale measurements. Nominal pressure is the total force divided by projected area. The Weibull-effect can to some extent be used to explain the decrease in strength for bigger areas: the bigger the contact area, the bigger the chance of a "weak link" (T. Sanderson, 1986). Design curves on the form  $P = Ca^D$  have been fitted to the data (T. J. Sanderson, 1988).  $P$  is global average pressure,  $a$  is global area and  $D$  and  $C$  are fitting-parameters. Ice class rule design pressures are often based on equations on this form. G. Timco and Sudom (2013) argued that even though this relation mostly holds true, there are cases where it does not, and other factors such as ice properties or failure mode are more important. It should be emphasized that these curves do not take into account the spatial variations of the pressure, but is the average over an area. The full-scale data showed little dependence on ramming speed, except at very low impact speeds (I. J. Jordaan, 2001; Ritch et al., 2008). For large ice features, the high pressure zones may appear more as separate patches, in contrast to the line-like load already described. An illustration of this pressure distribution is presented in Figure 2.15 and 2.16. As with smaller ice features, there are low pressure zones and areas not loaded at all. The icebreaker *CCGS Terry Fox* was equipped with strain gauges to measure localized pressures during impacts with icebergs (Ritch et al., 2008). Figure 2.17 shows a highly nonuniform pressure distribution measured during ramming of a 1900 t bergy bit. It was assumed that the pressure distributions within the loaded cells are uniform, which is not true. The true maximum pressure is thus larger than the approximately 11 MPa seen in the figure.

Some important parameters/characteristics influencing the behavior of ice, relevant for ship impact scenarios, are summed up in Table 1. A comment is given and the importance is rated from high to low.

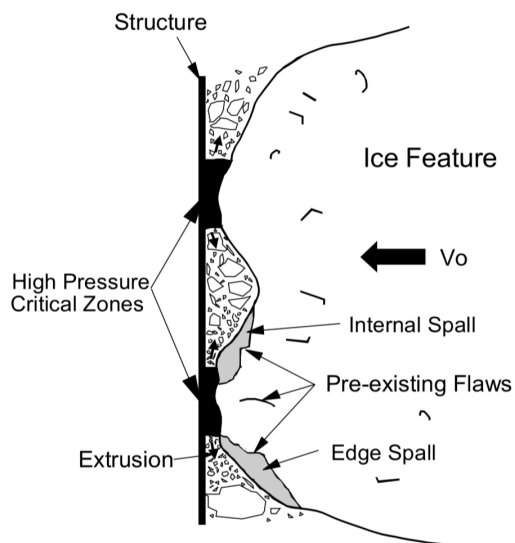


Figure 2.16: Wide interaction area seen on impacted area (I. J. Jordaan, 2001).

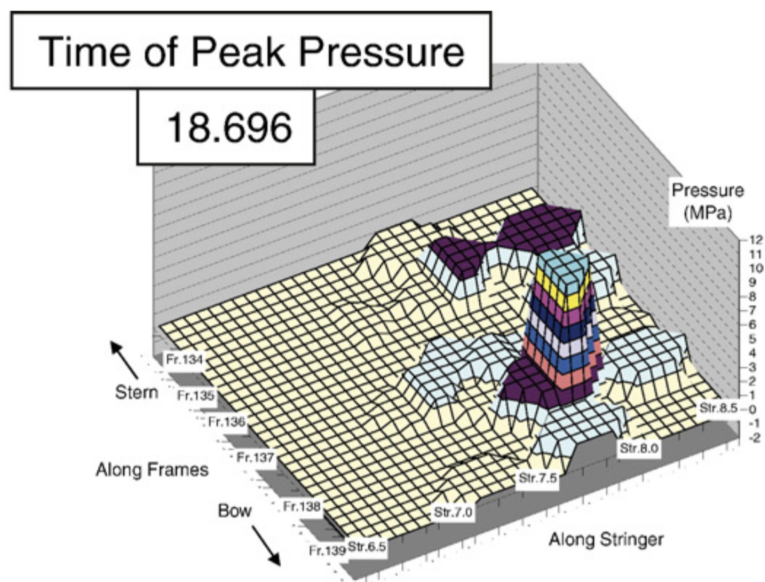


Figure 2.17: Pressure distribution on icebreaker hull during impact with bergy bit of 1900t. The size is approximately 2.4 m × 2.0 m (Ritch et al., 2008).

Table 1: Key properties of ice relevant for ship-ice impacts.

Parameter/ Characteristic:	Comment:	Importance:
Strain rate	Profound impact on strength, increasing strength with increasing strain rate in general.	High
Hydrostatic pressure	Increasing strength with increasing hydrostatic pressure. Coulombic failure for low and plastic failure for higher pressure.	High
Temperature	Increasing strength and more brittle behavior with lower temperatures. There are some discrepancies in the data, but temperature dependency seems to be rather low.	Medium to low
Pressure distribution	Highly nonuniform, with localized high pressure zones experiencing pressures many times the average. High degree of temporal and spatial variation.	High
Ductile to brittle transition	Brittle behavior most relevant for high-speed impacts. In high pressure zones, however, more ductile tendencies may be observed.	Low
Structure of ice	Affects both strength and isotropy. Stronger and anisotropic for single crystal ice.	Medium
Failure mode	Chaotic cracking pattern. Greater strength and more energy is dissipated through crushing, than through spalling off bigger pieces. Governed by, among others, confining pressure.	High



### 3 Ice Class Rules

Operation in ice infested waters exposes structures to loads they otherwise would not experience and classification societies have therefore developed specific class notations for winter navigation. Ice loading on structures have not been fully understood, so rules and standards are to some extent based on empiricism (Kim & Amdahl, 2016). One of the first rules developed was the The Finish-Swedish Ice Class Rules (FSICR). DNV GL has made rules equivalent to these, which are applicable for ships operating in the northern Baltic in winter time. The vessel assessed in this thesis is assigned with the DNV GL class notation *Ice(1A\*)*, equivalent to *1A super* in FSICR.

The philosophy behind most ice class rule design loads (including DNV GL) is that all energy is dissipated by the ice. It is assumed that when structure and ice interact, crushing of ice occurs with only elastic deformation of the structure. Design pressures are based on empirical data (Section 2.3). This is a very simple approach where the complex modeling of ice is avoided. The design loads for DNV GL class notation *Ice(1A\*)* can be calculated according to the procedure in the following paragraph (*DNV GL rules for classification: Ships (RU-SHIP)*, 2016, Part 6, Chapter 6, Section 2).

A design ice height ( $h$ ), which is smaller than the level ice height ( $h_0$ ), is assumed to be in contact with the hull. For the class notation *Ice(1A\*)*  $h$  and  $h_0$  are 0.35 m and 1.00 m, respectively. A nominal ice pressure of 5600 MPa is used as basis when calculating the design pressure,  $P$ , according to Equation (3.1).

$$P = 5600 \cdot c_d \cdot c_1 \cdot c_a \quad (3.1)$$

$c_d$  is a factor that takes into account the influence of the size and engine output of the ship, and is calculated as:

$$c_d = \frac{a_1 \cdot k_1 + b_1}{1000} \quad (3.2)$$

where:

$$k_1 = \frac{\sqrt{\Delta_f P_{min}}}{1000} \quad (3.3)$$

- $a_1$  and  $b_1$  may take on different values, but will for the ship looked into be 6.0 and 518, respectively (see the rules (*DNV GL rules for classification: Ships (RU-SHIP)*, 2016, Part 6, Chapter 6, Section 2, 7.3) and Table 3 for ship data).
- $\Delta_f$  is the displacement of the vessel in tonnes.
- $P_{min}$  is the engine output<sup>2</sup> in kW.
- $c_1$  is a factor which takes account of the probability that the design ice pressure occurs in a certain region of the hull for the ice class in question. For the bow region, which will be looked into in this thesis, it takes the value of 1.0.

---

<sup>2</sup> $P_{min}$  can be calculated according to the rules (*DNV GL rules for classification: Ships (RU-SHIP)*, 2016) or can be taken as the actual engine output of the vessel (Nyseth, n.d.).



- $c_a$  is a factor which takes account of the probability that the full length of the area under consideration will be under pressure at the same time. It is defined as in Equation (3.4) and has a maximum and minimum value of 1.0 and 0.35, respectively. When designing,  $\ell_a$  shall in general be taken as the stiffener span, but can be used as a variable (Nyseth, n.d.; *DNV GL rules for classification: Ships (RU-SHIP)*, 2016, Part 6, Chapter 6, Section 2, 4.1.4).

$$c_a = \sqrt{\frac{\ell_0}{\ell_a}}, \quad \ell_0 = 0.6 \text{ m} \quad (3.4)$$

For direct analyses the pressure to be applied shall have a value of  $1.8 \cdot P$ , and the pressure patch shall have dimensions of  $h \cdot \ell_a$ . The acceptance criterion is that the combined effects from shear and bending using the von Mises criterion is below the yield point. The location of the load patch should be chosen such that the the capacity of the structure is minimized. It is emphasized in the rules that loads shall be placed at different locations and especially at mid-spans (*DNV GL rules for classification: Ships (RU-SHIP)*, 2016, Part 6, Chapter 6, Section 2 4.1.4).

In spite of the design requirements, damages are still expected during service life for the Baltic ice classes (Storheim, 2016; Riska & Kämäräinen, 2011) and damages are frequently reported (Hänninen, Merenkulkulaitos, & Sjöfartsverket, 2005; Marchenko, 2014). The philosophy behind this is an optimization between repair costs, reduced building costs and increased payload capacity, as discussed by Kujala and Ehlers (2013). Small damages such as dents in frames and plates will in general not be a safety issue, so ULS may still be satisfied (Storheim, 2016). It is still difficult to define requirements on maximum allowable permanent deformations as this may differ between vessels. The research by Kujala and Ehlers (2013) actually indicates that it would be more economic to increase the design loads: A case study done on the bulk carrier MV Kemira showed that using design loads more than 100 % higher than the Baltic ice class design loads would have been best in an economic point of view. It should also be noted that "assistance from icebreakers is normally assumed when navigating in ice bound waters" for ships designed according to the Baltic rules (*DNV GL rules for classification: Ships (RU-SHIP)*, 2016, Part 6, Chapter 6, Section 2, 4.1.2). This means that vessels with a Baltic ice class notations are not designed to withstand loads from ramming heavy ice features such as ice ridges or icebergs.

The assumption that all energy is dissipated in the ice, is no longer valid when larger deformations occur in the structure. NORSOK (2004b) divides the distribution of strain energy dissipation for collision between two objects in three domains:

- Strength design domain
- Shared-energy design domain
- Ductility design domain

These domains are distinguished according to Figure 3.1. The ice class rules use a strength design. For normal operation in level ice it is obvious that there cannot be continuous energy dissipation in the hull of a vessel. When a structure is loaded beyond this level, deformations and energy dissipation will be significant also in



the structure (shared-energy). To assess shared-energy scenarios, accurate methods for assessing ice loading must be at hand and material models for both ice and vessel must be used. The third design approach (ductile design) assumes a rigid ice feature so that all impact energy will be dissipated in the ship. Designing and building structures based on the ductile design approach will often be costly and overconservative (Storheim & Amdahl, 2014), making the approach unfavorable in most cases.

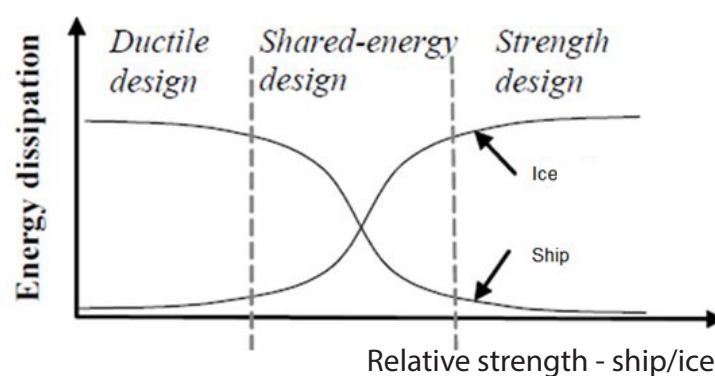


Figure 3.1: Energy dissipation for strength, ductile and shared-energy design (NORSOK, 2004b).

The residual capacity of a hull subjected to ice loading will be looked into in this thesis, which will be relevant for assessing typical ALS and ULS scenarios. A shared-energy approach should be applied if such scenarios are to be modelled properly (since both bodies will deform) which would require implementation of a material model for ice. Even though a material model for ice will not be implemented in the later analyses, a literature study on some available methods for modeling ice will be presented in the following section.



## 4 Numerical Models Representing Ice

Materials such as steels have been heavily studied and its behavior is well understood for "normal" temperatures (ISSC, 2015). For ice, however, this is not the case. Considerable research has been done on making models for ice, yet there is not agreement on a material model that captures the physical effects involved good enough to be used in impact analyses. In the following will some material models for representing ice be presented.

### 4.1 Plasticity Based Material Model for Ice

Liu et al. (2011) proposed a material model where ice is described as an elastic-perfectly plastic material. For the elastic behavior, the only input parameters needed are the Young's modulus,  $E$ , and the Poisson's ratio,  $\nu$ . An associated flow rule is used for plastic deformations. The Tsai-Wu yielding surface formulated for isotropic materials is used, and this yielding surface is dependent on the hydrostatic pressure. The yielding function,  $f$ , can be given as one of the two following expressions:

$$f(p, J_2) = J_2 - (a_0 + a_1 p + a_2 p^2) \quad (4.1)$$

$$f(p, \sigma_{eq}) = \sigma_{eq} - \sqrt{a_0 + a_1 p + a_2 p^2} \quad (4.2)$$

where:

- $J_2 = \frac{1}{2} \sigma'_{ij} \cdot \sigma'_{ij}$  is the second invariant of the deviatoric stress tensor,  $\sigma'$ .
- $\sigma'_{ij} = \sigma_{ij} - \frac{1}{3} \sigma_{kk} \delta_{ij}$  are components of the deviatoric stress tensor.
- $\delta_{ij}$  is the Kroenecker delta.
- $\sigma_{ij}$  is a component of the stress tensor,  $\sigma$ .
- $a_0, a_1$  and  $a_2$  are empirical parameters.
- $p$  is the hydrostatic pressure given as  $p = -\frac{1}{3} \sigma_{ii}$ .
- $\sigma_{eq} = \sqrt{\frac{3}{2} \sigma'_{ij} \cdot \sigma'_{ij}}$  is the equivalent (deviatoric) stress.

Einstein's summation convention is used. Yielding will only occur when the yielding function is equal to zero.

The yielding surface will under certain conditions form an ellipsoid in the 3D space of the principal stresses (Ferrari et al., 2015), with its centerline being the hydrostatic axis. The point where the hydrostatic axis crosses the yielding surface in compression defines the pressure causing the ice to melt, and the other crossing point where the ice flows in tension. However, due to difficulties in fitting the yielding surface to experimental data (Ferrari et al., 2015), a cut-off pressure,  $p_{cut}$ , is introduced for tension-loads to prevent overestimation of the tensile strength.

The model uses an element deletion/erosion technique. This means that elements that satisfy the failure criterion will instantly be removed from the body. The proposed failure criterion is based on a plastic failure strain,  $\varepsilon_f$ , which is purely empirical.

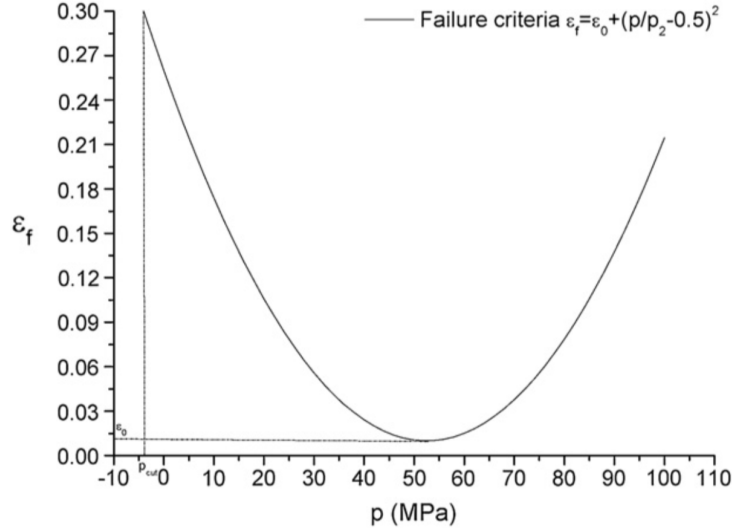


Figure 4.1: Failure strain as a function of hydrostatic pressure (Liu et al., 2011).

It has the form:

$$\varepsilon_f = \varepsilon_0 + \left( \frac{p}{p_2} - 0.5 \right)^2 \quad (4.3)$$

where:

- $p_2$  represents the melting pressure and is the largest root of the yielding function on the form  $f(J_2, p) = 0$ .
- $\varepsilon_0$  is initial failure strain, and is an empirical value.

The idea behind Equation (4.3) is to model the transition between brittle Coulombic failure and plastic failure. For low confining pressures, Coulombic faults occur. At these pressures, crushed ice will not easily be extruded, which is modeled as a high failure strain. As the pressure increases, more and more crushed ice will be extruded, modeled as decreasing  $\varepsilon_f$ . Even higher hydrostatic pressure changes the failure mode to plastic fault and stiffens the ice, which is modeled by again increasing  $\varepsilon_f$ . This failure criterion forms an U-shaped strain versus pressure failure curve, and an example is seen in Figure 4.1. Equivalent plastic strain,  $\varepsilon_{eq}^p$ , is given as:

$$\varepsilon_{eq}^p = \sqrt{\frac{2}{3} \varepsilon_{ij}^p \cdot \varepsilon_{ij}^p} \quad (4.4)$$

- $\varepsilon_{ij}^p$  are components of the plastic strain tensor,  $\boldsymbol{\varepsilon}^p$ .

Element deletion is activated when the equivalent plastic strain exceeds failure strain, the tension pressure is smaller than the cut-off pressure or when the pressure is greater than the melting pressure, summed up below:

$$(\varepsilon_{eq}^p > \varepsilon_f) \cup (p < p_{cut}) \cup (p > p_2) \Rightarrow \text{Deletion} \quad (4.5)$$

Table 2: Input parameters for yield surfaces.

Parameter	data 1 Riska and Frederking (1987)	data 2 Riska and Frederking (1987)	Kierkegaard (1993)	Derradji- Aouat (2000)
$a_0$	1.60	3.1	2.588	22.93
$a_1$	4.26	9.20	8.63	2.06
$a_2$	-0.62	-0.83	-0.163	-0.023

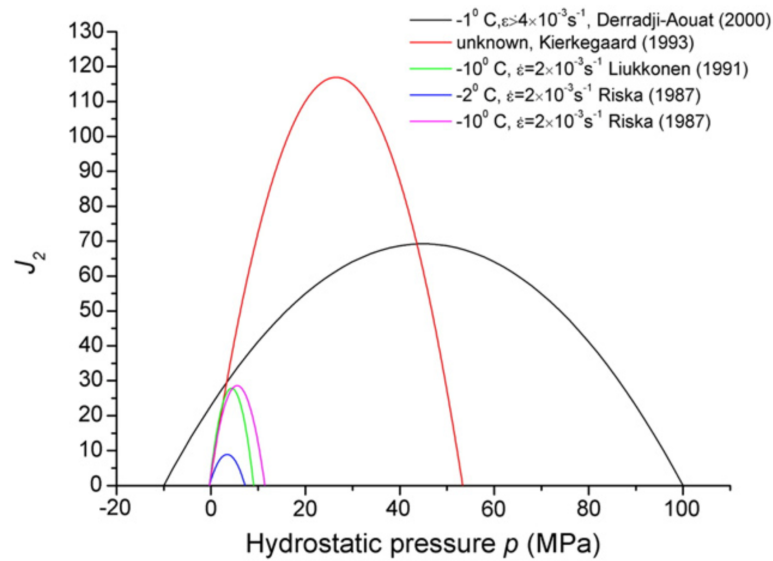


Figure 4.2: Representation of yield surfaces for different parameters(Liu et al., 2011).

The parameters  $a_0$ ,  $a_1$  and  $a_2$  should be fit to experimental data. Some research has been done on this using data from triaxial stress tests and the resulting parameters are shown in Table 2. Yield surfaces turn out quite different for the different parameters, as seen in Figure 4.2. An obvious reason for the difference is that the sets of parameters result from different experiments, with different strain rates and temperatures and possibly also structure, grain size, temperature history, density etc.. The influence of such variables can only be included implicitly through the yield surface, failure criterion, elastic constants and cut-off pressure. With sufficient experimental data, parameters as a function of the variables of interest could be made, looking like:

$$\varepsilon_0(x_1, x_2, \dots); E(x_1, x_2, \dots); a_0(x_1, x_2, \dots); a_1(x_1, x_2, \dots); a_2(x_1, x_2, \dots) \quad (4.6)$$

where  $(x_1, x_2, \dots)$  are the variables of interest. Elements in the body can then be assigned different material properties to model spatial variations, such as Liu et al. (2011) have done with a temperature gradient.

Liu et al. (2011) analyzed a conical shaped iceberg model impacting a rigid wall (Figure 4.5) using the different data sets. Recorded maximum pressure versus con-

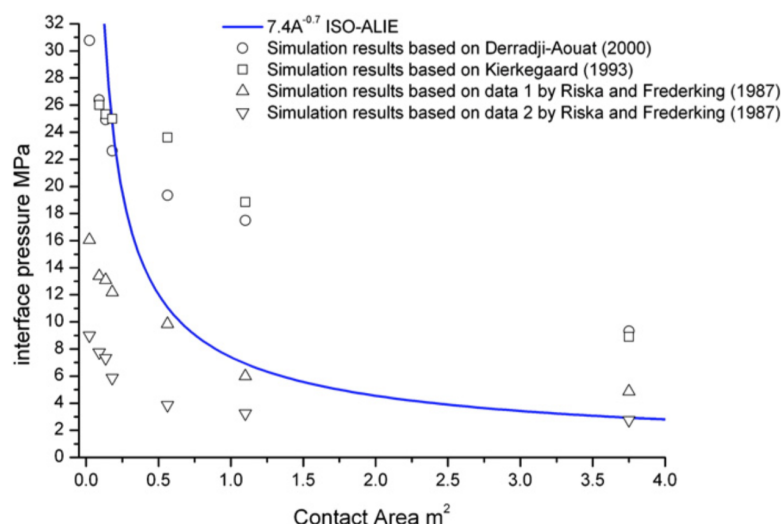


Figure 4.3: Recorded maximum pressures for different set of parameters (Table 2) (Liu et al., 2011).

tact area obtained for the different sets of parameters are presented in Figure 4.3, together with the recommended ISO<sup>3</sup> design curve (ISO, 2011). Liu et al. (2011) recommended using the parameters proposed by Derradji-Aouat (2000) for considering local deformation of ship structures. These parameters give  $p_2 \approx 100$  MPa, which is consistent with the phase diagram for freshwater ice at  $-11^\circ\text{C}$  (Ferrari et al., 2015). However, the resulting tensile strength of more than 7 MPa is not in agreement with experimental values, and thus the cut-off pressure,  $p_{cut}$ , was set to -2 MPa.

The *Pond Inlet tests* are experiments that were done by indenting a rigid hemispherical indenter into iceberg ice and measuring the pressures (Daley, 1994). Liu et al. (2011) numerically replicated the Pond Inlet indentation tests using the proposed material model. Derradji-Aouat (2000)' parameters were used for the numerical simulation and the other parameters were  $E = 9.5$  GPa,  $\nu = 0.3$ ,  $\rho = 900 \frac{\text{kg}}{\text{m}^3}$  and  $\varepsilon_0$  was by trial and error set to 1 %. The nominal pressure versus contact area is presented in Figure 4.4. For small contact areas the curve does not match the experimental data, but it is improving for larger contact areas.

Ferrari et al. (2015) analyzed a spherical iceberg impacting a rigid wall (Figure 4.7) using the proposed material model. The pressure distribution at initial impact is seen in Figure 4.8. As expected, the pressure distribution is mesh-dependent. When the central elements are deleted, contours of a circle are visible, since these are the next elements to come in contact with the wall. The force fluctuates as elements are deleted, which can be unfavorable if doing dynamic analyses. The amplitude of the force fluctuation decreases and the frequency increases as the element size decreases. Figure 4.9 shows the iceberg model at the end of the analysis where it is seen that the rigid planar impact surface makes the iceberg model have a more or less planar side itself, due to erosion. The replicated Pond Inlet tests from (Liu et al., 2011) show the same tendency: A sphere cap is "cut out" of the ice body due to erosion of elements. During the impact of the conical iceberg model (Figure 4.5) some cracking

<sup>3</sup>International Organization for Standardization.

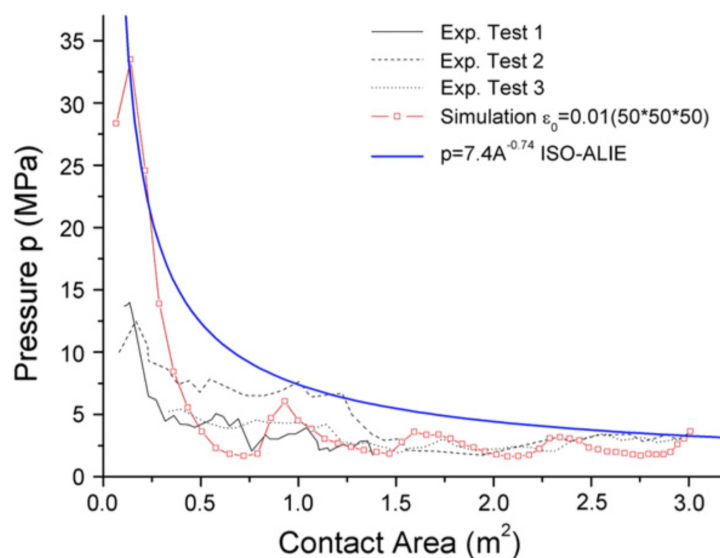


Figure 4.4: Pressure versus nominal area relation for numerical results versus experimental data (Liu et al., 2011).

took place for elements near the contact area. Whether or not this simulates "real" cracking is not verified. An example of recorded contact pressure is displayed in Figure 4.6, where a high local maximum of 81 MPa can be observed. Storheim et al. (2012) analyzed a spherical iceberg of diameter of 2 m impacting a rigid wall at  $1 \frac{m}{s}$ . The pressure distribution, though right after massive erosion (Storheim et al., 2012), is displayed in Figure 4.10. Note the circles of higher pressure, similar to the ones in Figure 4.8.

## 4.2 Other Models

Gagnon (2007) introduced a crushable foam model for ice. A user defined volumetric<sup>4</sup> strain versus volumetric stress curve describes how the foam responds to deformation. Large nonrecoverable strains can develop at a constant pressure of 0.1 MPa up to a fractional volumetric strain of 0.065. From there on, steep hardening at a rate of 4.7 GPa occurs for further deformations, until a volumetric strain of 1.0 is reached. This model does not allow much energy absorption after initial straining because of the steep hardening. To overcome this problem, cut-off values for the stress were later introduced: one for a soft layer and one for a hard layer, at 10 and 50 MPa respectively (Gagnon, 2011). Further straining will happen at constant stress, making the model less rigid.

This crushable foam model has been criticized for not having any physical explanation, which results obtained using this material model support. Some results obtained by Storheim et al. (2012) are displayed in Figure 4.11, 4.12 and 4.13. The model called "Gagnon2011" used (0.0 0.0, 0.015 25, 0.5 50, 1.0 50) as volumetric stress ver-

<sup>4</sup>"Volumetric" means the component that contributes to changing the volume. Volumetric stress is the same as hydrostatic stress or pressure.

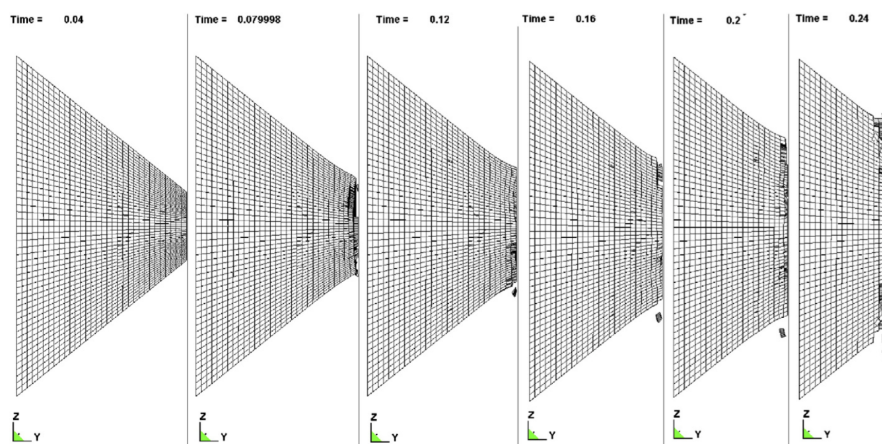


Figure 4.5: Numerical simulation of conical shaped iceberg impacting wall (Liu et al., 2011).

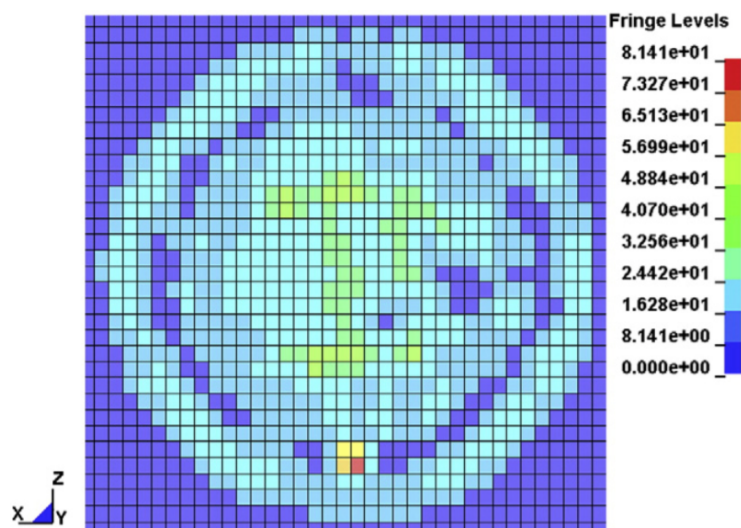


Figure 4.6: Example of pressure distribution on wall during impact with conical shaped iceberg (Liu et al., 2011).



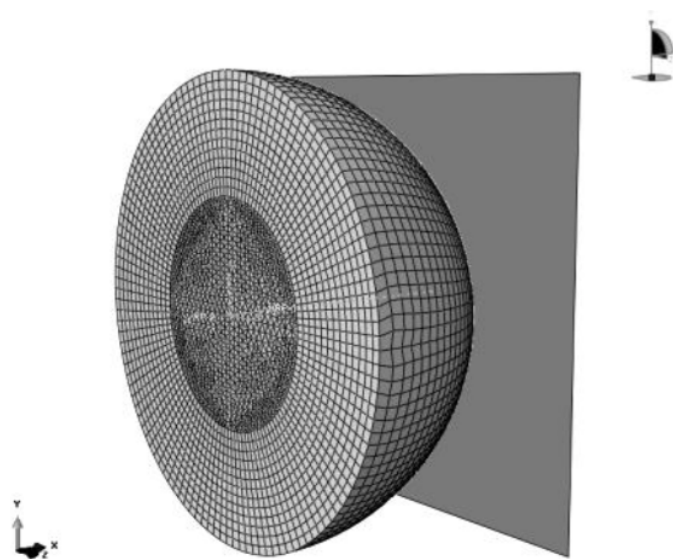


Figure 4.7: FEM model of iceberg impacting rigid wall (Ferrari et al., 2015).

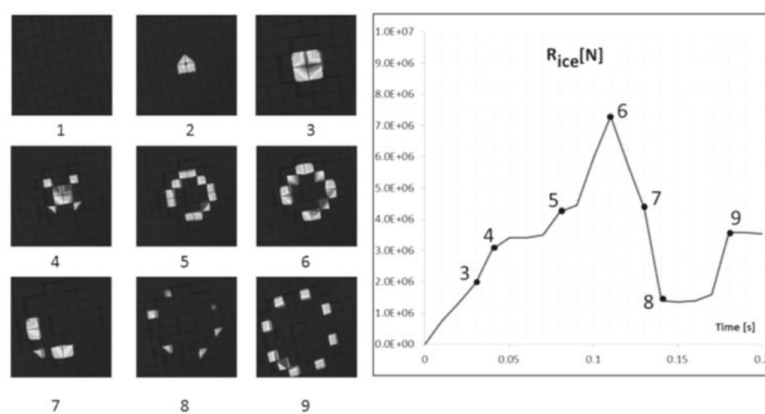


Figure 4.8: Contact pressures from initial contact (Ferrari et al., 2015).

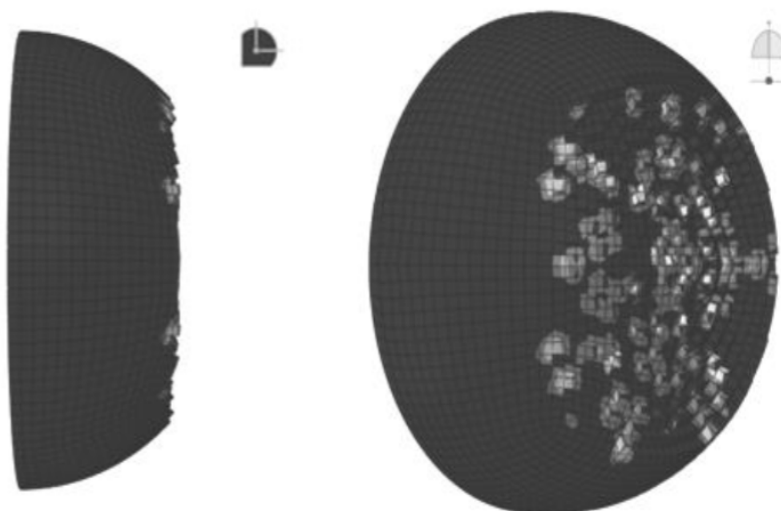


Figure 4.9: Eroded iceberg at end of impact analysis (Ferrari et al., 2015).

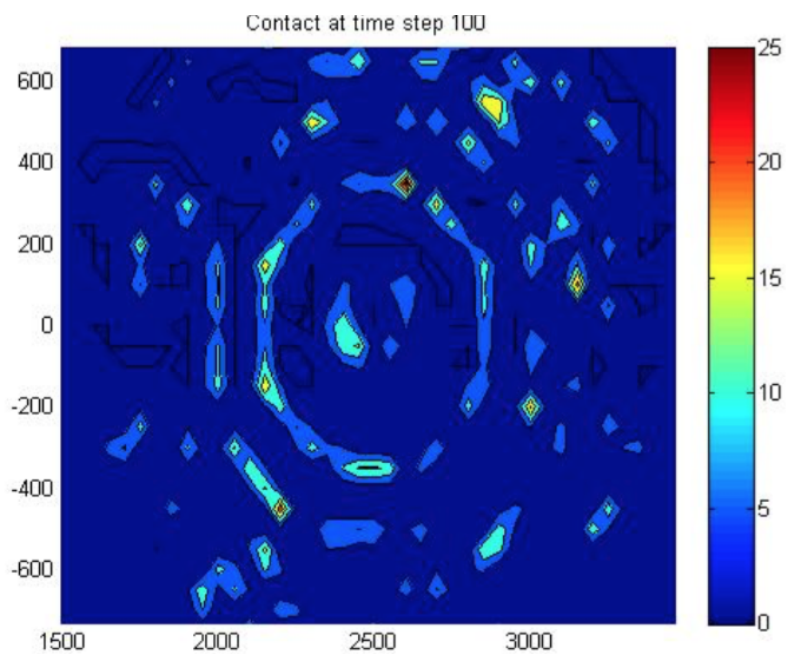


Figure 4.10: Pressure contour of iceberg colliding with rigid wall, Liu's material model. Units are mm and MPa. (Storheim et al., 2012).

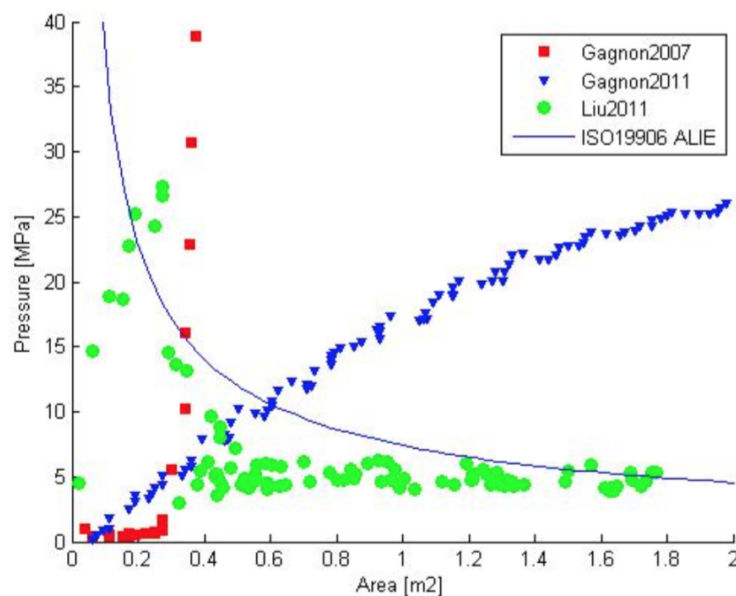


Figure 4.11: Pressure area relation of two of Gagnon's crushable foam models and the plasticity based model by Liu (Storheim et al., 2012).

sus strain curve on the form (strain[-] stress [MPa], ...), whereas "Gagnon2007" used the volumetric stress strain relation defined in the above paragraph. Nominal pressure *increases* for increasing nominal area, contrary to what is found in experiments. Pressure contours do reproduce to high pressure zones and the spatial variations seen from experiments. Also, the ice deformation shows a mismatch between what is physically expected since the ice is bending significantly at the sharp corner (Figure 4.13).

Daley (1991) developed an idealized 2D model to describe the flaking process of ice sheet indenting a flat structure. Flaking is initiated when the average shear stress on a straight plane from the middle of the contact zone exceeds the Coulomb failure criterion. Only half the contact area is left after flaking, and crushing will occur until the next Coulomb failure criterion is reached. The model achieved good results compared to experimental data (Daley et al., 1998). However, visco-elastic effects are only included implicitly and adhesive behavior is ignored (Riska, 1995). The model was developed to model level ice versus structure interaction and is more applicable for assessing ice induced vibrations in ice flow, than accidental ice feature impacts.

Gürtner, Bjerås, Kühnlein, Jochmann, and Konuk (2009) used numerical methods developed by Gürtner, Konuk, and Løset (2008) and Konuk, Gürtner, and Yu (2009) to model ice actions on a fixed lighthouse. Ice is modeled as a combination of bulk elements and cohesive elements. Rectangular bulk elements make up the mass and the ice itself, whereas cohesive elements have negligible mass and volume. Bulk elements are divided by the cohesive elements, which allows for crack propagation along the bulk elements. Cohesive elements can be assigned different properties to simulate anisotropy and different cohesive properties. Since the ice sheet can be divided by several layers of bulk elements through the thickness, this combination

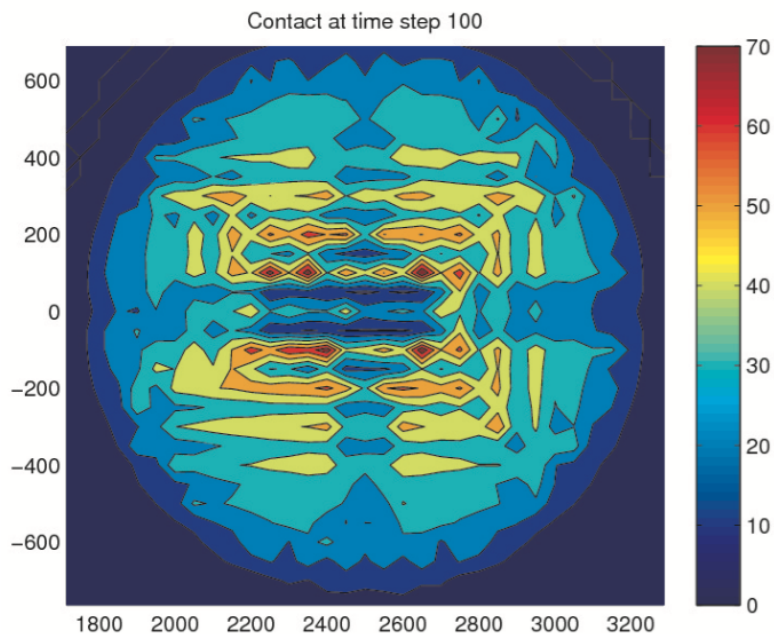


Figure 4.12: Pressure contour of iceberg colliding with rigid wall, Gagnon’s 2011 model. Units are mm and MPa (Storheim et al., 2012).

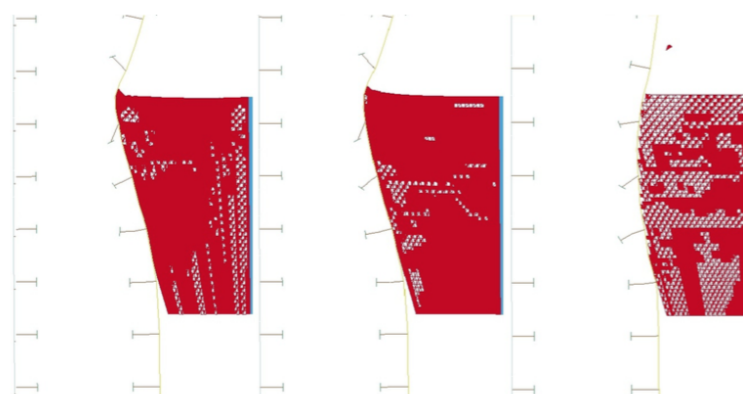


Figure 4.13: Deformation plot of impact between iceberg and deformable vessel. Gagnon’s two models are on the left, Liu’s on the right (Storheim et al., 2012).

of elements can be used to model crushing. Bulk elements are not deleted as the ice is crushed and there is frictional contact between them, so that pile up formations can be modeled. The model was developed to assess lower speed level ice versus structure interaction, so its application lies within modeling continuous ice crushing, crack propagation and pile up. Strain rate effects are not taken into account explicitly and the line-load pressure contour is not replicated, but the load pattern produced is nonuniform. Cracks can only propagate along element borders since elements cannot be divided, which is limiting. A numerical model where cracks have the ability to propagate through elements exists, making crack propagation unbiased with respect to the mesh (Belytschko & Black, 1999), but this is not dug into in this thesis.

Kwak, Choi, Park, and Woo (2009) analyzed collision between an arctic tanker and sea ice. Their approach was very different from the others described. Instead of trying to replicate physical behavior of sea ice, their material model was calibrated to match the IACS<sup>5</sup> Polar Rule loads. An interesting feature is that solid elements were connected through truss elements in order to simulate flexural failure. However, since this model is developed to reproduce rule-based loads and not necessarily to model real ice properties, no further attention is given to this model.

Daley and Kim (2010) introduced an analytical approach to assess loading in ship versus iceberg collisions. These methods are, however, more applicable for well defined contact areas, and are thus not suited for ALS assessments including possible large deformations.

Another possibility of assessing ship-ice interaction avoids the difficulties with making a material model for ice. Available data from full- and medium-scale experiments can instead be used directly. Measured pressure distributions can be painted directly on the structure, possibly including temporal and spatial variation. The size and type of the painted pressure patch must be adjusted to the impact event of interest. If the local shape of the ice feature at initial contact yields a small contact area, pressure distributions for medium-scale tests could be used. The contours from full-scale measurements should be used for larger contact areas. Ice and/or ship will deform during impact and the contact area will in most cases increase. Pressure contours could to some extent be scaled up and/or additional patches could be added. For severe damages involving deep penetration and rupture of the hull, it can be problematic modeling the load-transfer to parts such as girders. However, it may be argued that what happens after severe rupture is of less significance, since the question of interest in most cases is whether rupture happens or not.

This method of using pressure painting and impulse considerations have not, by the author's knowledge, been applied for ship-iceberg impact analysis. However, Quinton, Daley, Gagnon, et al. (2012) have already developed a method for applying pressures on a structure. Pressures varying in both 3D space and time can be applied to structure surfaces, and the method is thus called "4D Ice pressure loading method". Discrete pressure patches, uniform and nonuniform loads being either stationary or time-dependent, can be applied, making the method very flexible. If the resolution of experimental pressure-data is not satisfying, interpolation schemes are proposed for refinement, so that for example a more conservative inter-

---

<sup>5</sup>International Association of Classification Societies.

polation scheme can be used for design purposes. Painting predetermined pressure-distributions will in general not take into account interaction effects that may occur during deformation of the structure, since the ice feature is bodyless. This is a shortcoming of the method. One of the findings was that moving loads yield larger damages to structures than stationary loads, so it is important to include this in design (Quinton et al., 2012). Also, a similar approach has been done by Erceg et al. (2014), but without the time-variation of the pressure distribution. A stiffened panel was loaded with a nonuniform line load, and compared to the same panel loaded uniformly according to polar class rules (FSICR/IACS). The damage obtained by painting real pressure contours were more severe compared to the damage obtained using rule-based uniform loads, which again is emphasizing the importance of using nonuniform loading for design purposes.

### 4.3 Remarks on Material Models

Ice deformation is a highly complex process. There are so many factors affecting the properties and the failure modes of ice, making it troublesome to make material models for ice capturing all necessary physical effects. The model proposed by Liu et al. (2011) is simple, computational efficient and yield somewhat good results for larges contact areas. Pressure distributions, however, are not similar to observed ones. To better include spatial and temporal variations occurring in ice during deformation would demand many different sets of input parameters, which is not feasible. Using a conservative set of parameters makes the model somewhat applicable, but extensive verification and testing must in that case be done. The other numerical models that have been shortly introduced, also have trade-offs making them less suited for ship versus ice feature collision assessment. A general problem is that many models are tailor made to model certain aspects of ice behavior. There are so many complex processes involved in an ALS scenario (i.e. ship-ice impact) and no model seems to include the different aspects of ice deformation in a satisfactory manner.

Simply painting known pressure distributions on the hull structure (Quinton et al., 2012) has the great advantage of not relying on any material model for ice. Also, computational costly calculations of iceberg deformations are avoided. There are some issues regarding interaction of load and structure and how to choose loading pattern. Still, this method should be looked into since it might be easier to overcome these shortcomings than to make a trustworthy material model for ice.

A more detailed discussion of the material models can be found in (Mork, 2015).



## 5 Finite Element Analysis

The Finite Element Method (FEM) is a powerful tool usable for solving complex engineering problems within flux, thermo, electrical, structural analysis and other fields. The development of FEM started in the middle of the 20<sup>th</sup> century and the method is today widely used. FEM is applicable for solving boundary value problems, which are problems that can be formulated by a set of partial differential equations and associated boundary conditions (Hopperstad & Børvik, 2014). The method is based on the Principle of Virtual Work (PVW). In the ship industry, FEM is used mostly for stress and response analyses in structural engineering. The great power of FEM is that constitutive and kinematic relations for single elements can be determined in a simple manner and then be assembled to a system valid over the whole structure. Problems not solvable with analytical solutions can in this way be solved. For more in depth information on FEM, readers are referred to other literature (Wriggers, 2008; Hopperstad & Børvik, 2014; Fish & Belytschko, 2007). Some of the underlying theory will be introduced in the following, based on the lecture notes by Hopperstad and Børvik (2014, ch. 4.5). Bold symbols denote vectors, matrices or tensors and italic, non-bold symbols denote scalar valued quantities.

A continuous problem can be divided into a finite number of elements. Elements consist of and are connected through nodes. An illustration of this can be found in Figure 5.1. Displacements are only given at nodes, so elemental interpolation functions are used to interpolate displacements within elements. The displacement field,  $\mathbf{u}(\mathbf{x}, t)$ , is obtained by multiplying the matrix of elemental interpolation functions,  $\mathbf{N}_e(\mathbf{x})$ , by the element nodal displacement vector,  $\mathbf{v}_e(t)$ :

$$\mathbf{u}(\mathbf{x}, t) = \mathbf{N}_e(\mathbf{x})\mathbf{v}_e(t), \quad \mathbf{x} \in V_e \quad (5.1)$$

A relation between displacements at discrete nodal points and the continuous displacement field through the domain of an element is by this established.  $\mathbf{x}$  is the position vector and must be within the volume of the element,  $V_e$ . The subscript  $e$  denotes the element number and  $t$  is the time. Time can refer to a given state of deformation/loading, and is not necessarily actual time.

The relation between nodal ( $\mathbf{v}_e(t)$ ) and global ( $\mathbf{r}(t)$ ) displacements is found through the connectivity matrix,  $\mathbf{a}_e$ , defined so that:

$$\mathbf{v}_e(t) = \mathbf{a}_e(t)\mathbf{r}(t) \quad (5.2)$$

The global displacement field is calculated from Equation (5.3) which is valid over the volume of the whole structure,  $V$ . Continuity requirements must be fulfilled for the shape functions, but for more information readers are referred to the lecture notes by Mathiesen (2014).

$$\mathbf{u}(\mathbf{x}, t) = \sum_e \mathbf{N}_e(\mathbf{x})\mathbf{v}_e(t) = \left[ \sum_e \mathbf{N}_e(\mathbf{x})\mathbf{a}_e \right] \mathbf{r}(t) = \mathbf{N}(\mathbf{x})\mathbf{r}(t), \quad \mathbf{x} \in V \quad (5.3)$$

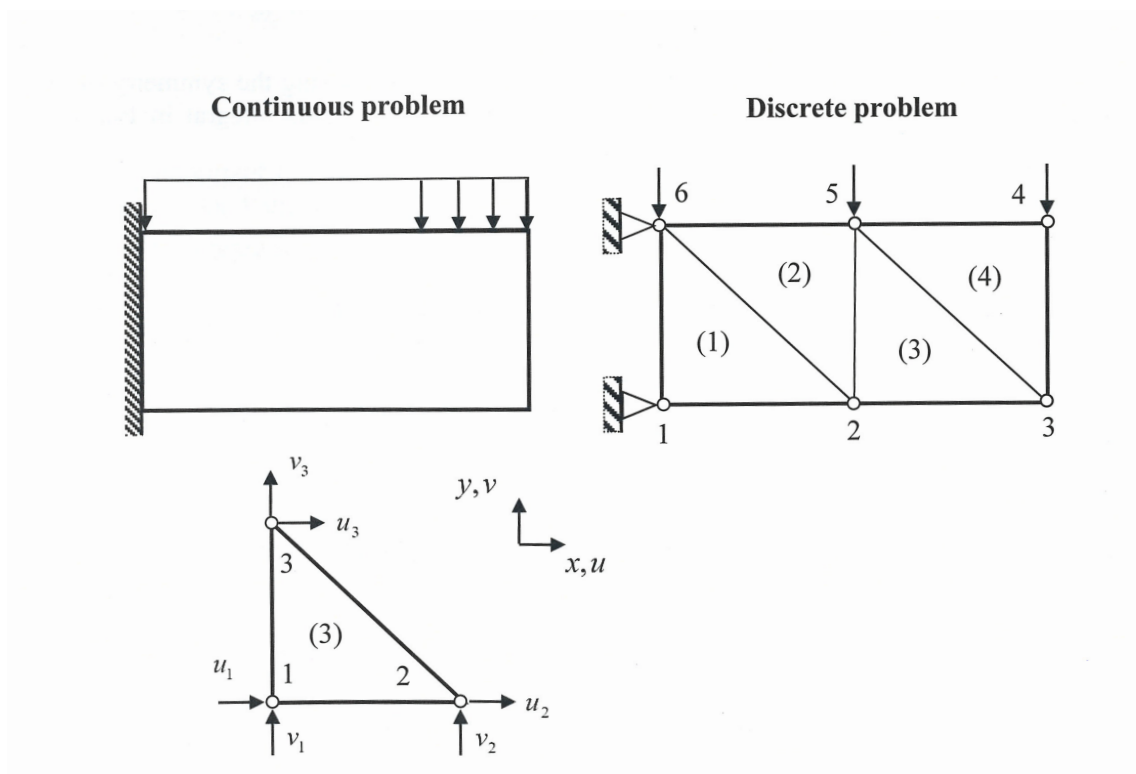


Figure 5.1: A continuous mechanical problem discretized into finite elements and nodes. Element numbers are in parentheses. Global system with global node numbers is depicted in the upper right part. Local degree of freedoms are seen for element (3) in the bottom part (Hopperstad & Børvik, 2014).



$\mathbf{N}(\mathbf{x})$  is a matrix containing the shape functions for all elements.

$\boldsymbol{\varepsilon}$  is the strain tensor on vector form and can be calculated according to Equation (5.4) where  $\boldsymbol{\Delta}$  is a differential operator.

$$\boldsymbol{\varepsilon} = \boldsymbol{\Delta}\mathbf{u}, \quad \mathbf{x} \in V \quad (5.4)$$

The strain-displacement matrix,  $\mathbf{B}(\mathbf{x})$ , in Equation (5.5) is defined so that the global strain field can be calculated based on global nodal displacements, Equation (5.6).

$$\mathbf{B}(\mathbf{x}) = \boldsymbol{\Delta}\mathbf{N}(\mathbf{x}) \quad (5.5)$$

$$\boldsymbol{\varepsilon}(\mathbf{x}, t) = \mathbf{B}(\mathbf{x})\mathbf{r}(t), \quad \mathbf{x} \in V \quad (5.6)$$

Virtual displacements, strains and global nodal displacements are introduced as  $\delta\mathbf{u}(\mathbf{x}, t)$ ,  $\delta\boldsymbol{\varepsilon}$  and  $\delta\mathbf{r}(t)$ , so that:

$$\delta\boldsymbol{\varepsilon} = \boldsymbol{\Delta}\delta\mathbf{u} = \mathbf{B}\delta\mathbf{r}, \quad \mathbf{x} \in V \quad (5.7)$$

The same interpolation functions as for the real displacements are used.

$\boldsymbol{\sigma}$ ,  $\mathbf{b}$  and  $\mathbf{t}$  are the stress tensor, body forces and traction forces, respectively, on vector form. PVW requires that the increase in virtual strain energy must be equal the virtual work done by traction and body forces. In other words: the internal and external virtual work must be equal (Equation (5.8)).

$$\int_V \delta\boldsymbol{\varepsilon}^T \boldsymbol{\sigma} dV = \int_V \delta\mathbf{u}^T \mathbf{b} dV + \int_S \delta\mathbf{u}^T \mathbf{t} dS \quad (5.8)$$

$S$  is the surface of the body.

By rewriting Equation (5.8) and extracting the global virtual nodal displacements from the integrals (as they are dependent only on  $t$ ), the following equation is obtained:

$$\delta\mathbf{r}^T \left[ \int_V \mathbf{B}^T \boldsymbol{\sigma} dV - \int_V \mathbf{N}^T \mathbf{b} dV - \int_S \mathbf{N}^T \mathbf{t} dS \right] = 0 \quad (5.9)$$

For the nodes without prescribed displacements, the following relation holds:

$$\int_V \mathbf{B}^T \boldsymbol{\sigma} dV - \int_V \mathbf{N}^T \mathbf{b} dV - \int_S \mathbf{N}^T \mathbf{t} dS = 0 \quad (5.10)$$

These are nodal forces and can be separated as external and internal nodal forces (Equation (5.11)).

$$\mathbf{R}^{int} = \int_V \mathbf{B}^T \boldsymbol{\sigma} dV, \quad \mathbf{R}^{ext} = \int_V \mathbf{N}^T \mathbf{b} dV + \int_S \mathbf{N}^T \mathbf{t} dS \quad (5.11)$$

Using a constitutive relation, for example on the form  $\boldsymbol{\sigma} = \mathbf{C}\boldsymbol{\varepsilon} = \mathbf{C}\mathbf{B}\mathbf{r}$  (where  $\mathbf{C}$  is the elasticity matrix), the internal forces can be written on the well known form:

$$\mathbf{R}^{int} = \mathbf{K}\mathbf{r} \quad (5.12)$$

where  $\mathbf{K}$  is the global stiffness matrix which in this case is given as  $\mathbf{K} = \int_V \mathbf{B}^T \mathbf{C} \mathbf{B} dV$ .

## 5.1 Linear Finite Element Analysis

The system of equations to be solved can in general be written as in Equation (5.13).

$$\mathbf{M}\ddot{\mathbf{r}} + \mathbf{C}\dot{\mathbf{r}} + \mathbf{K}\mathbf{r} = \mathbf{R} \quad (5.13)$$

$\mathbf{M}$ ,  $\mathbf{C}$  and  $\mathbf{K}$  are the mass<sup>6</sup>-, damping- and stiffness matrices.  $\mathbf{R}$  is the vector of external forces (excluding damping and inertia forces) and  $\ddot{\mathbf{r}}$ ,  $\dot{\mathbf{r}}$  and  $\mathbf{r}$  are vectors of acceleration, velocity and displacement, respectively. Nodal values for all Degrees Of Freedom (DOFs) are included in  $\mathbf{R}$ ,  $\ddot{\mathbf{r}}$ ,  $\dot{\mathbf{r}}$  and  $\mathbf{r}$ .

Problems can be divided into static and dynamic problems. In the case that the loading frequency is far away from one of the natural frequencies of a structure there is no risk of resonance. Furthermore, if inertia forces and damping forces are assumed to be negligible, transient terms can be disregarded (assuming non-viscous material behavior). Analyses done under these assumptions are called *quasi-static*. The equation of motion (Equation (5.13)) can then be reduced to the last two term as shown in Equation (5.14).

$$\mathbf{R} = \mathbf{K}\mathbf{r} \quad (5.14)$$

When deformations are assumed small and material behavior is linear elastic, linear FEM is applicable.  $\mathbf{K}$  will then be treated as constant and Equation (5.14) forms a system of linear equations. Only one increment of Equation (5.14) needs to be solved to obtain all information with respect to load versus response. Theoretically, any load magnitude can be withstood by a structure and failure will not occur. The principle of superposition holds because loading history is insignificant. Stresses, displacements and strains etc. can be scaled linearly with the initial load to obtain responses for different load magnitudes. Linear Finite Element Analysis (FEA) is widely used in structural engineering due to its simplicity and low computational cost. When assessing operational loads and fatigue, linear FEA will in most cases be the preferred technique since these typically yield small deformations in the linear range of the material. The method is also useful when assessing onset of permanent deformations (yielding).

---

<sup>6</sup>See for example the book by [Wriggers \(2008\)](#) for information on establishing the mass matrix,  $\mathbf{M}$ .

## 5.2 Nonlinear Structural Analysis

Other solution methods must be applied to simulate the structural behavior in a correct manner when nonlinear effects are influential. Different nonlinearities can take place and they are typically divided into three main categories (Wriggers, 2008; Falzon & Hitchings, 2006):

- Material nonlinearity
- Geometrical nonlinearity
- Boundary nonlinearity (contact)

### Material Nonlinearity

Materials deform according to Hooke's Law in the linear elastic domain, implying a linear relation between stresses and strains (Figure 5.2a). Hooke's law in its simplest form is defined as  $\sigma = E\varepsilon$  where  $\sigma$  is the stress,  $E$  is the Young's modulus and  $\varepsilon$  is the strain. For nonlinear material behavior the stiffness of the material (tangent modulus  $E_t$ ) varies. This is called material nonlinearity and is illustrated in Figure 5.2b. The tangent modulus will then be a function of the parameters changing the stiffness,  $E_t(a, b, c, \dots)$ . Plastic behavior and yielding is one of the most common nonlinearities included in material models, especially for steels. Note that also elastic materials can exhibit nonlinear behavior. Apart from strain, parameters such as temperature, hydrostatic pressure and strain rate could influence the tangent modulus (strain rate-dependency implies viscous behavior and would require dynamic analysis). These parameters will in most cases be a function of displacements so that the system stiffness matrix will be given as  $\mathbf{K}(\mathbf{r})$ .

### Geometrical Nonlinearity

When deformations are sufficiently large, loads and resistance can change due to a geometry change of the problem. This phenomenon is known as geometrical nonlinearity. It has nothing to do with the constitutive model of the material and can happen for elastic as well as plastic materials. For problems exhibiting geometrical nonlinearity, it is necessary to use formulations that include the exact geometry of the problem. Figure 5.3 shows some examples of geometrical nonlinearity. If a platform with a heavy top side structure is displaced horizontally, an "extra" moment from the lateral load is added. This is called the P-delta effect, and is illustrated in Figure 5.3a. A second example is a beam freely supported at both ends with a centered point load,  $P$ . An elastic-perfectly plastic material model is assumed. The response is linear until onset of yielding, from where the stiffness will decrease. The load bearing capacity increases slightly as more and more of the cross section yields. Membrane effects will start to dominate for further loading, increasing the load bearing capacity and stiffness significantly. This is illustrated in Figure 5.3b. Another example of geometrical nonlinearity is the snap-through problem in which both stiffness and load may be negative, illustrated in Figure 5.4. For more examples

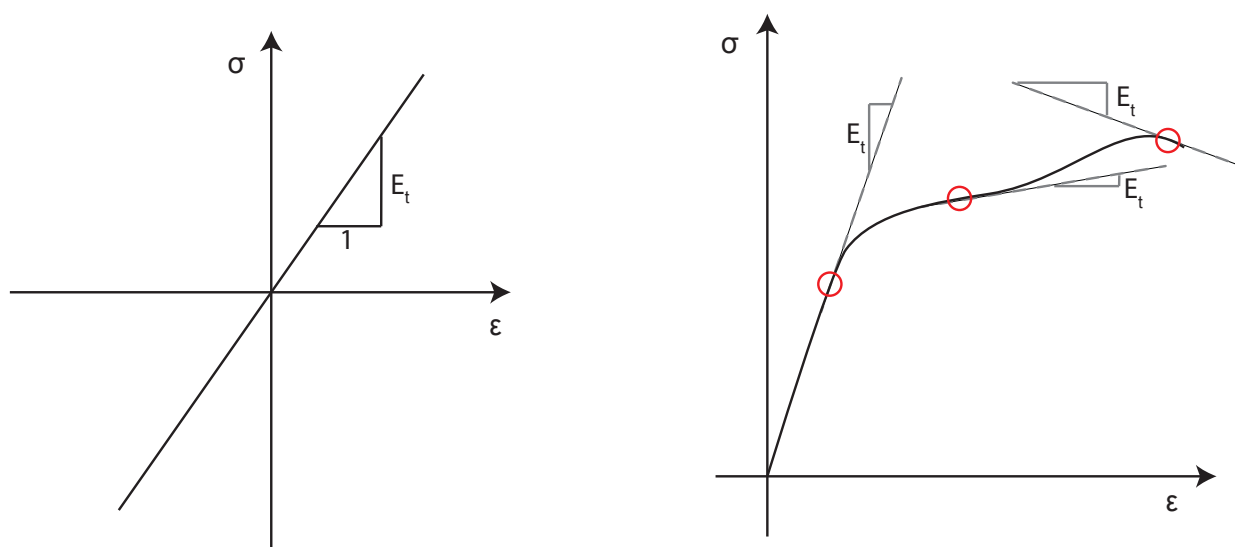
(a) Linear material -  $E_t$  is constant.(b) Nonlinear material -  $E_t$  varies.

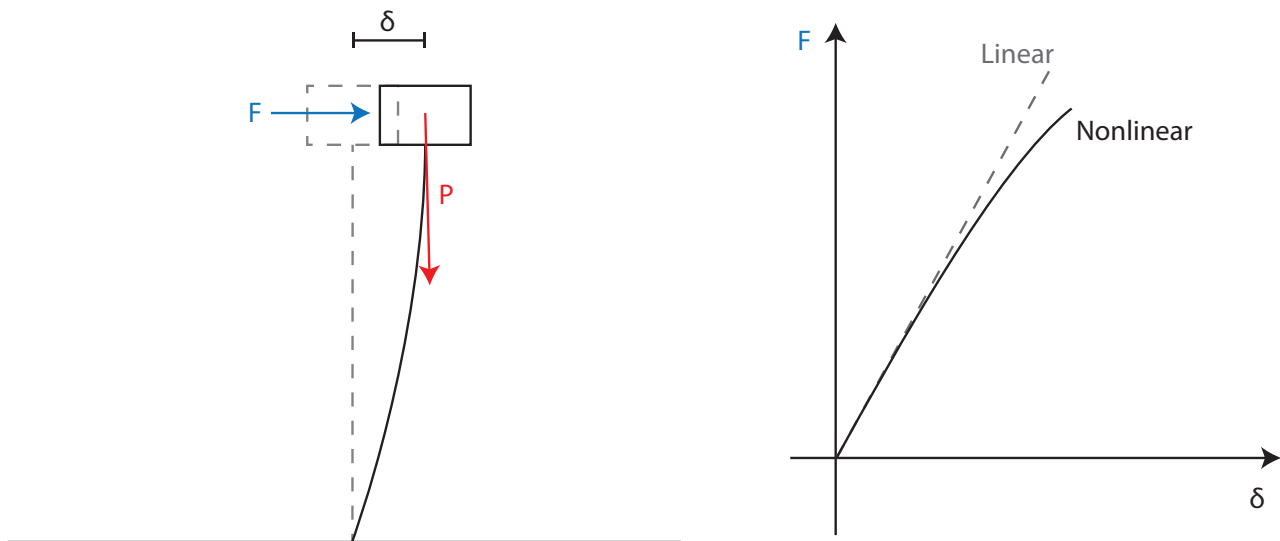
Figure 5.2: Material nonlinearity.

and other types (snap-back, bifurcation, follower load etc.) readers are referred to the books by [Wriggers \(2008, Ch. 2\)](#) and [Falzon and Hitchings \(2006\)](#). Geometrical nonlinearity makes loads and stiffness dependent on the state of deformation, so that they can be given on the forms  $\mathbf{R}(\mathbf{r})$  and  $\mathbf{K}(\mathbf{r})$ , respectively.

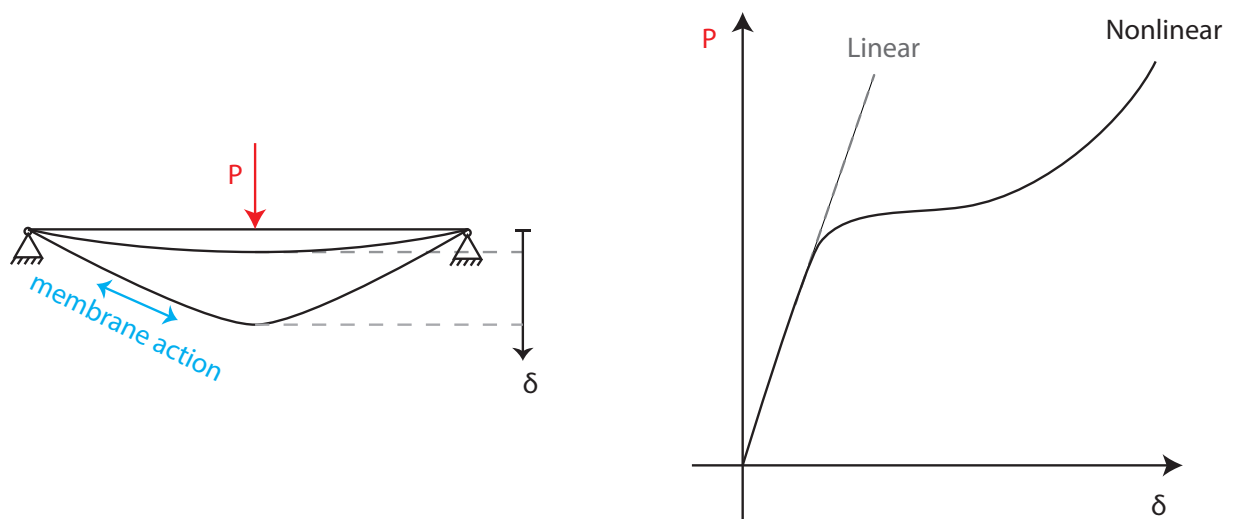
### Boundary Nonlinearity

A third source of nonlinearity is boundary conditions and contact. When a body comes in contact with either itself or the surroundings, the stiffness can change. A simple illustration of this can be found in Figure 5.5, where it is apparent that the stiffness changes as the right end of the elastic bar comes in contact with the wall. Another example of this type of nonlinearity is when a structure comes in contact with itself during deformation.

Collisions and explosions, or large elastic deformation of for instance slender structures such as pipelines, are typical scenarios where nonlinear effects are profound. Nonlinear Finite Element Analysis (NLFEA) will in these cases be required. Responses are in general history-dependent so the principle of super position does not hold. Solution schemes for NLFEA are in general complex and computationally expensive. The use of NLFEA is therefore limited compared to that of linear FEA, but as computer power is becoming cheaper the use of NLFEA is increasing. Structures often have large residual capacities after onset of permanent deformations. With



(a) P-delta effect: The weight of structure causes a moment of magnitude  $P\delta$  and will influence the response for large displacements, which is seen in the right figure.



(b) Laterally loaded beam at different stages of deformation and the nonlinear load deflection curve. Elastic-perfectly plastic material model is assumed.

Figure 5.3: Geometrical nonlinearity.

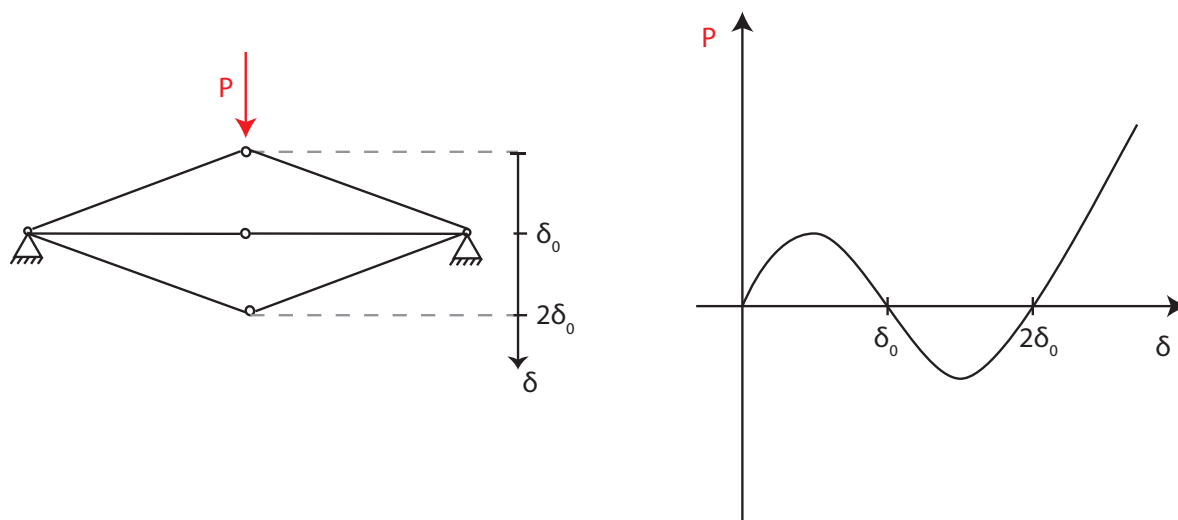


Figure 5.4: Geometrical nonlinearity. Snap-through: Instability occurs as the limit point is passed and the stiffness becomes negative. Stability is reached after "snapping through", and there is a following change from compression to tension in the rods.

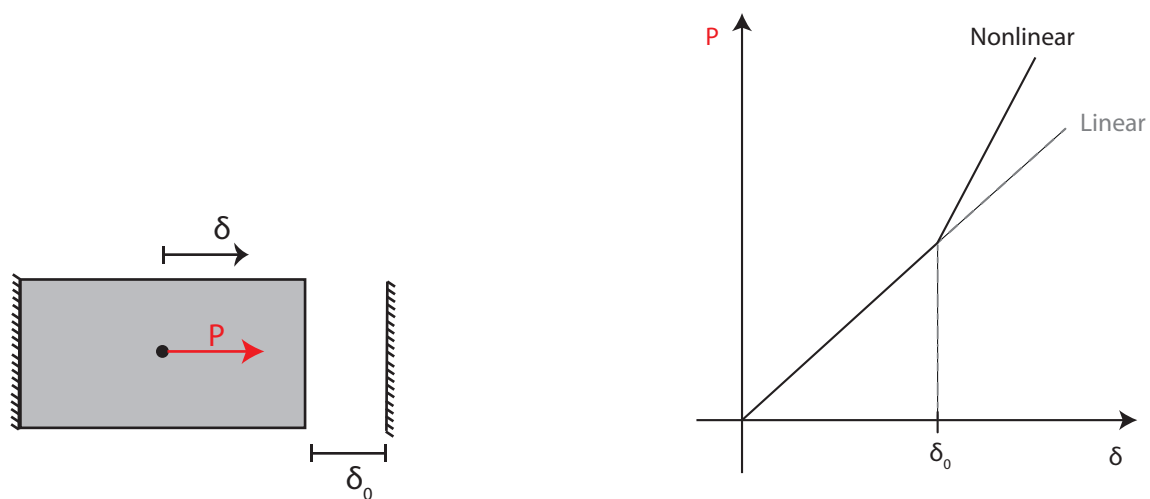


Figure 5.5: Nonlinearity due to boundary conditions and contact. When the right part of bar comes in contact with the wall, the stiffness increases. Load deformation curve is seen to the right.

NLFEA this can be taken into account when designing, allowing lighter and cheaper structures to be built.

### 5.2.1 Solution Schemes

The set of equations to be solved for nonlinear, quasi-static problems can in general be written on the form found in Equation (5.15). This equation cannot generally be solved directly, so incremental solution procedures must be used. Many different schemes have been developed, and each have its pros and cons (Wriggers, 2008; Falzon & Hitchings, 2006).

$$\mathbf{R}(\mathbf{r}) = \mathbf{K}(\mathbf{r})\mathbf{r} \quad (5.15)$$

There are two ways of applying loads: Load control means changing the load incrementally, while displacement control means changing the displacements incrementally. Which method is used, depends on the nature of problem that is looked into and on the solution method that is used for solving Equation (5.15). Because of nonlinear behavior, the load (or displacements) must in general be split up and applied incrementally. For each increment, numbered by  $n$ , the stiffness matrix is updated before applying next load (or displacement) increment. Nonlinear problems are in other words solved by approximating the nonlinear solution path with a set of smaller linear solution increments.

In an *explicit* solution scheme, unknown information is calculated directly from already known information. In practice, this means that when a new load increment ( $\Delta R_{n+1}$ ) is applied, the stiffness at the previous increment ( $K(r_n)$ ) is used when calculating current displacement increment ( $\Delta r_{n+1}$ ), see Equation (5.16), (5.17) and (5.18).

$$R_{n+1} = R_n + \Delta R_{n+1} \quad (5.16)$$

$$r_{n+1} = r_n + \Delta r_{n+1} \quad (5.17)$$

$$\Delta r_{n+1} = \frac{\Delta R(r_{n+1})}{K(r_n)} \quad (5.18)$$

The advantage of such a procedure is that iterations and equation solving are not required for each increment, making it computationally inexpensive and appropriate for models with a large number of DOFs. A drawback of the procedure is that it is only conditionally stable. If the increment size is too large, the solution will drift off from the correct solution path since there are no convergence requirements. However, when increments are small enough, the calculated solution will be close to the actual true solution. Increment size must therefore be chosen with care. Explicit solution schemes are applicable when highly nonlinear behavior is expected (buckling, material failure etc.) and is often used for dynamic analyses of explosions and collisions. Small time increments are often required when simulating high speed impacts, making long duration analyses computationally expensive. Note that when talking about time,  $r_n$  refers to the displacement at time  $t_n$ ,  $r_n = r(t_n)$ , so that actual time is not needed.

In contrast to an explicit scheme, an *implicit* solution procedure ensures that internal and external forces are (almost) equal after each increment. If this criterion is not fulfilled, iterations are done until the required accuracy is reached (convergence). This procedure is therefore unconditionally stable, and much larger increments can be used. Implicit solutions schemes calculate the response based on the current time/increment ( $n + 1$ ), and this has to be done iteratively. The advantage of the implicit method is that much larger increments size can be used, but more calculations have to be done for each increment. It is ideal for problems where nonlinearities are smooth, such as plasticity dominated problems.

A common implicit solution scheme is the *Newton-Raphson method* (called **Static, General** in Abaqus) and a brief explanation based on lecture notes by [Hopperstad and Børvik \(2014\)](#) is presented in the following. The residual nodal force vector is defined as:

$$\mathbf{G} = \mathbf{R}^{int} - \mathbf{R}^{ext} \quad (5.19)$$

and is equal to zero when a structure is in equilibrium with external forces.  $\mathbf{G}$  is in general not equal to zero after a load increment due to nonlinearities. It is assumed equilibrium has been found  $\mathbf{G}_n = \mathbf{0}$  at a previous increment,  $n$ . The residual at the next increment ( $n + 1$ ) will then be:

$$\mathbf{G}_{n+1}^{i+1} = \mathbf{R}^{int}(\mathbf{r}_{n+1}^{i+1}) - \mathbf{R}_{n+1}^{ext} \quad (5.20)$$

The superscript  $i$  denotes the iteration counter. Linearizing Equation (5.20) using Taylor expansion yields:

$$\mathbf{G}_{n+1}^{i+1} \approx \mathbf{G}_{n+1}^i + \frac{\partial \mathbf{G}_{n+1}^i}{\partial \mathbf{r}_{n+1}^i} \Delta \mathbf{r}_{n+1}^{i+1} = \mathbf{0} \quad (5.21)$$

The external forces are not a function of displacement, so the tangent stiffness matrix can be defined as:

$$\frac{\partial \mathbf{G}_{n+1}^i}{\partial \mathbf{r}_{n+1}^i} = \frac{\partial \mathbf{R}^{int}(\mathbf{r}_{n+1}^i)}{\partial \mathbf{r}_{n+1}^i} = \mathbf{K}^t(\mathbf{r}_{n+1}^i) \quad (5.22)$$

Equation (5.21) can then be rewritten to:

$$\mathbf{G}_{n+1}^{i+1} \approx \mathbf{G}_{n+1}^i + \mathbf{K}^t(\mathbf{r}_{n+1}^i)(\mathbf{r}_{n+1}^{i+1} - \mathbf{r}_{n+1}^i) = \mathbf{0} \quad (5.23)$$

Using Equation (5.11), the tangent stiffness matrix can be written as:

$$\mathbf{K}^t(\mathbf{r}_{n+1}^i) = \int_V \mathbf{B}^T \frac{\partial \boldsymbol{\sigma}(\mathbf{r}_{n+1}^i)}{\partial \mathbf{r}_{n+1}^i} dV \quad (5.24)$$

The consistent tangent operator,  $\mathbf{C}_{n+1}^{alg}$ , can be defined as:

$$\mathbf{C}_{n+1}^{alg} = \frac{\partial \boldsymbol{\sigma}_{n+1}}{\partial \boldsymbol{\varepsilon}_{n+1}} \quad (5.25)$$

so that effects of the material nonlinearity is included in the tangent stiffness matrix the following way:

$$\mathbf{K}_{n+1}^t = \int_V \mathbf{B}^T \mathbf{C}_{n+1}^{alg} \mathbf{B} dV \quad (5.26)$$



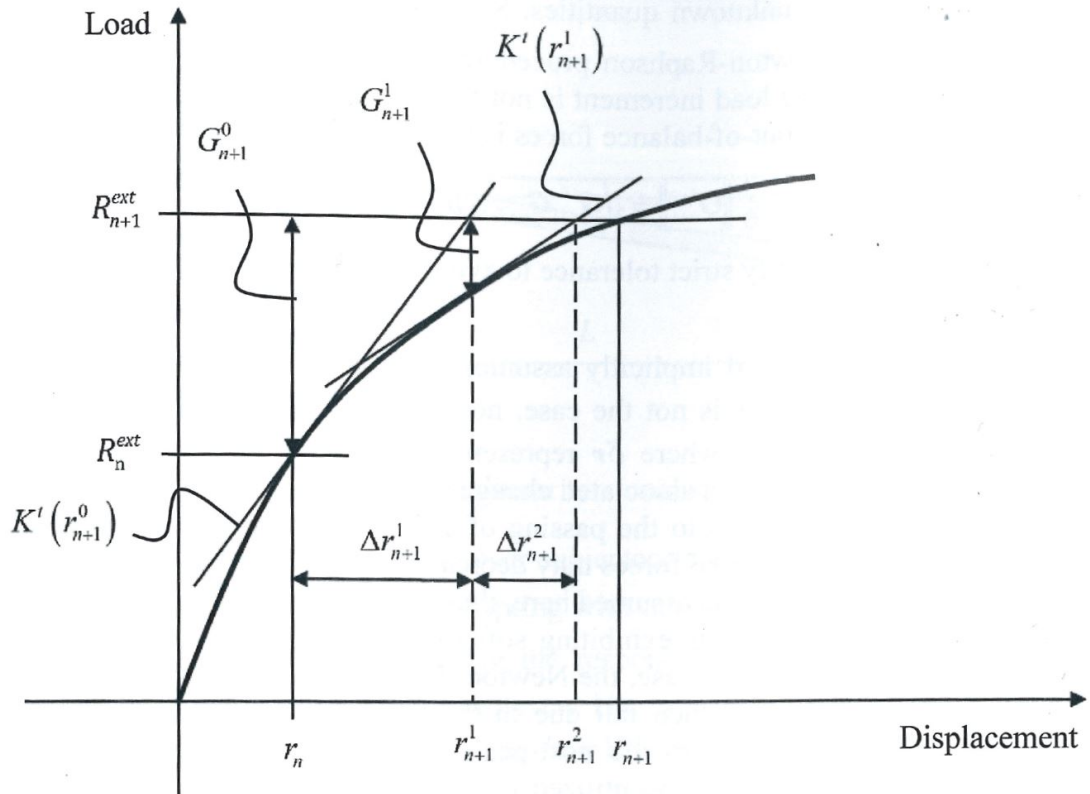


Figure 5.6: Illustration of the Newton-Raphson method (Hopperstad & Børvik, 2014).

Necessary terms are now known so that  $\mathbf{r}_{n+1}^{i+1}$  can be calculated from Equation (5.23). The iterations are stopped when convergence is reached, that is when the residual forces become below a certain limit,  $\epsilon$ .

$$\epsilon \geq \sqrt{(\mathbf{G}_{n+1}^i)^T \mathbf{G}_{n+1}^i} \quad (5.27)$$

When convergence is satisfied, a new load increment can then be applied. If the tolerance ( $\epsilon$ ) is too large, the numerical results can drift off from the actual solution. In fact, by setting  $\epsilon$  very large, iterations will not be executed and this procedure behaves as an explicit solver.

Figure 5.6 illustrates the Newton-Raphson method. Since the tangent stiffness matrix is updated at every iteration, this method is in general computational expensive. The convergence rate is, however, very high. There are other versions of this procedure where the stiffness matrix is not updated at every iteration, or not at all, in order to save computational power. These schemes will not be utilized in this thesis, so readers are referred to the book by Wriggers (2008, Ch. 5.1.2) for more information.

The Newton-Raphson method has some limitations. The tangent stiffness matrix will be singular at limit points, so there will either be problems with converging, or the solution can jump to another point on the equilibrium path. Softening behavior will not be captured. Using load control may circumvent this limitation, or alternatively use of stabilization (will not be introduced in this thesis). Snap back behavior cannot be simulated any case.

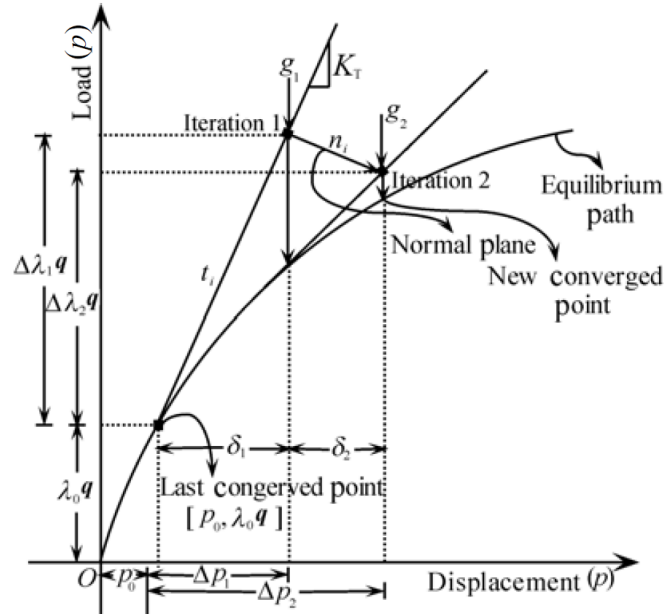


Figure 5.7: Illustration of the modified Riks method (Memon & Su, 2004).

Another type of solution schemes are the so-called arc length methods, where both load and displacement are incremented simultaneously. The great advantage of an arc length method is that all types of load deformation curves can be simulated, because decreasing displacement and/or load can be simulated (negative increments). This makes the methods suitable for analyses where highly nonlinear responses are expected, including snap-through and snap-back behavior. There are different types of arc length methods (Mathiesen, 2015; Wriggers, 2008), and Abaqus uses the modified Riks method (called `Static`, `RIKS` in Abaqus). Increment sizes are determined from a given arc length (user specified or calculated by Abaqus). By using the stiffness at last equilibrium point, load and displacement increments are calculated from a second order polynomial. An iterative algorithm corrects the solution onto the equilibrium path in a plane orthogonal to the linear load-displacement curve from the last increment, until convergence is reached. The Newton method is still the basic algorithm. This method is illustrated in Figure 5.7, but detailed explanation of symbols and algorithm will not be presented in this thesis and readers are referred to the *Abaqus Theory Guide* (Systèmes, 2016, Ch. 2.3.2) for this.

Since the incremental arc length is calculated from a second order polynomial, the wrong (negative) root may in special cases be chosen. Points on an equilibrium path where sudden change of stiffness occur (high curvature and bifurcation) are typical locations where the method will have problems with finding the correct solution. Either the equilibrium path will be followed "backwards", or no further equilibrium point will be found. Another disadvantage is that the method is relatively computational expensive, making the Newton-Raphson method preferred for simpler problems.

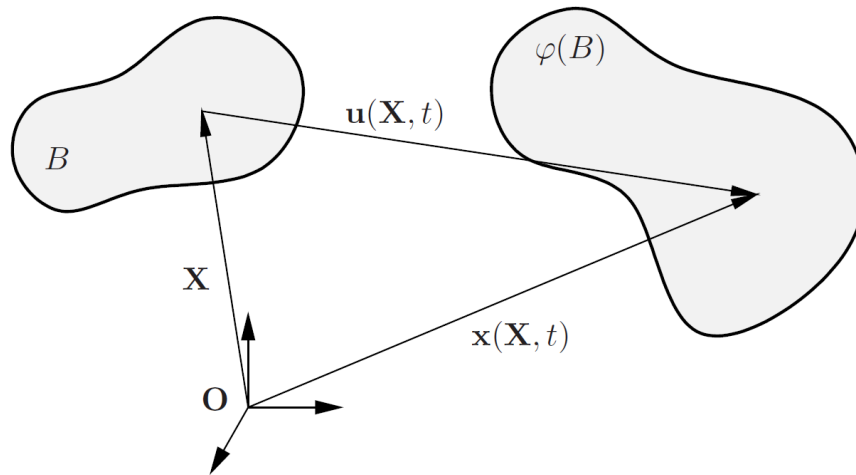


Figure 5.8: A body in undeformed ( $B$ ) and current ( $\varphi(B)$ ) configuration (Wriggers, 2008).

### 5.2.2 Tensor Analysis

The formulations for nonlinear analyses differ from those of a linear problem. In nonlinear analyses one must separate the undeformed (or *reference* or *material*) configuration of a body, from the deformed (or *current*) configuration. These are also denoted *Lagrangian* and *Eulerian* descriptions, respectively. Figure 5.8 shows a body in the undeformed,  $B$ , and in the current,  $\varphi(B)$ , configuration. Tensors referring to material configuration are written with capital letters and tensors referring to current configuration are written with lower case letters. From the same figure it is seen that a material point in the material configuration with coordinate  $\mathbf{X}$  has coordinates  $\mathbf{x}(\mathbf{X}, t)$  at a later time,  $t$ .  $\mathbf{u}$  is the displacement vector, so that:

$$\mathbf{x}(\mathbf{X}, t) = \mathbf{X} + \mathbf{u}(\mathbf{X}, t) \quad (5.28)$$

Different formulations for strains and stresses have to be used in *finite strain theory* (large deformation theory) than what is used in small strain theory. A brief example to illustrate this will be given here.

The deformation gradient,  $\mathbf{F}$ , is given as:

$$\mathbf{F} = \text{Grad}[\mathbf{x}] = \text{Grad}[\varphi(\mathbf{X}, t)] = \frac{\partial \mathbf{x}}{\partial \mathbf{X}} = \frac{\partial}{\partial \mathbf{X}}[\mathbf{X} + \mathbf{u}] = \mathbf{I} + \mathbf{H} \quad (5.29)$$

where  $\mathbf{I}$  is an identity tensor and  $\mathbf{H}$  is the displacement gradient. By looking at the change of the square of line elements in material and current configuration, a strain measure called the *Green-Lagrange strain tensor*,  $\mathbf{E}$ , can be derived:

$$\mathbf{E} = \frac{1}{2}(\mathbf{F}^T \mathbf{F} - \mathbf{I}) = \frac{1}{2}(\mathbf{H} + \mathbf{H}^T + \mathbf{H}^T \mathbf{H}) \quad (5.30)$$

The displacement gradient is small for small deformations, making the last second order term in Equation (5.30) negligible. The infinitesimal strain tensor,  $\boldsymbol{\varepsilon}$ , will then

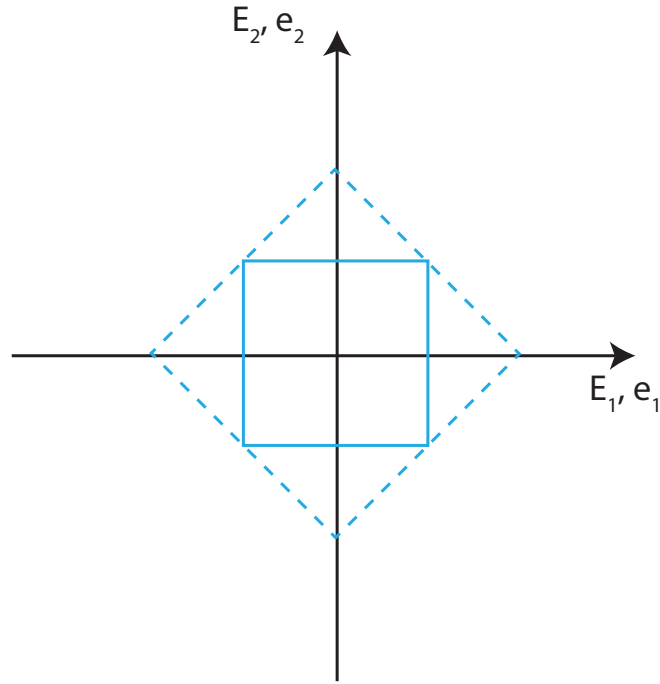


Figure 5.9: Body transformation according to Equation (5.32). The undeformed body is marked with the continuous blue line and the current configuration in blue dashed line.  $E_i$  and  $e_i$  are axes in material and current configuration.

be a good measure of strain:

$$(\mathbf{E} \approx) \boldsymbol{\varepsilon} = \frac{1}{2}(\mathbf{H} + \mathbf{H}^T) \quad (5.31)$$

In a simple 2D-example, the displacement field of a square is defined as:

$$\mathbf{u}(\mathbf{X}) = \begin{bmatrix} \mathbf{u}_1(\mathbf{X}) \\ \mathbf{u}_2(\mathbf{X}) \end{bmatrix} = \begin{bmatrix} -X_2 \\ X_1 \end{bmatrix} \quad (5.32)$$

The material and current configuration of the body is seen in Figure 5.9. It can be found from easy hand calculations that the infinitesimal strain tensor will be the zero matrix, even though it is apparent from the figure that there is straining. Similarly,  $\boldsymbol{\varepsilon}$ , will not be the zero matrix for a rigid body rotation, even though actual strains are zero. The Green-Lagrange strain tensor will, on the other hand, represent the strains correctly. From this example the need for other formulations than those of small strain theory comes clear. This applies to stresses as well as strains. Various formulations exist and each has its purpose, typically relating stresses and strains between different configurations. More details on finite strain tensor analysis are, however, not covered in this thesis. For more in depth information on the topic, see for example *Nonlinear Finite Element Methods* by [Wriggers \(2008, Ch. 4\)](#).

Formulations for finite strain theory are implemented in Abaqus when NLGEOM is turned on.

Table 3: Overview of vessel’s main characteristics.

Parameter	Value
Length (LPP)	75.6 [m]
Beam (B)	16.2 [m]
Draught (T)	5.0 [m]
Engine power (P)	6600 [kW]
Displacement ( $\Delta_f$ )	5000 [tonnes]

Table 4: Scantling data (see Figure 5.12 and 5.13 for explanations).

Parameter	Value
Skin thickness ( $t_{skin}$ )	16 [mm]
Stiffener spacing (approximate) ( $h_{stiffener}$ )	315-322 [mm]
Stiffener spacing in x-direction ( $h_{x,stiffener}$ )	300 [mm]
Web thickness ( $t_{web}$ )	10 [mm]
Web height ( $t_{web}$ )	260 [mm]
Flange thickness ( $t_{flange}$ )	27 [mm]
Flange width ( $w_{flange}$ )	47 [mm]
Stiffener length ( $\ell_{stiffener}$ )	3350 [mm]

### 5.3 Finite Element Model of Ship Hull

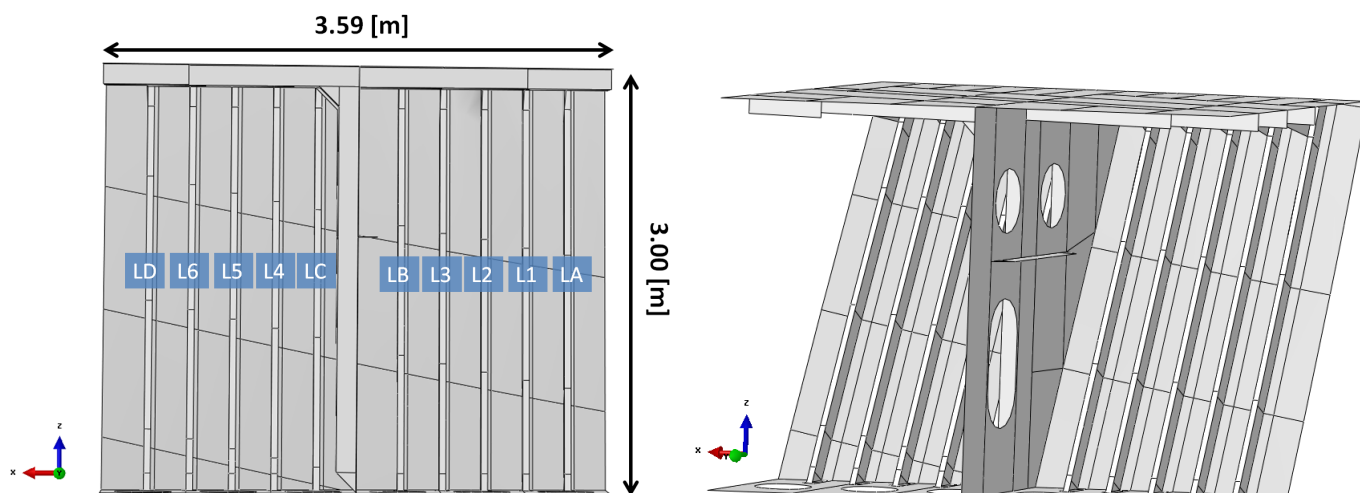
An .IGES-file which contains detailed hull geometry was used as a basis when developing the Finite Element (FE) model. Hull shape and curvature of the skin was obtained from this file, while other features, such as stiffeners and thicknesses, were obtained using hull drawings. It can be tricky to model and mesh double-curved surfaces in Abaqus, which are typical for ship hulls. A model previously developed by DNV GL was therefore provided. The model used in this thesis is based on this, but changes and fixes were done when necessary.

Some relevant information of the vessel is found in Table 3. Only local loads were to be assessed in this work, so only a small the FE model was needed. The part lies in the water line area in the bow, more specifically on the starboard side between the tween deck and the main deck. Geometry and main dimensions can be found in Figure 5.10 and an overview of the model’s location on the ship can be found in Figure 5.11. Outer skin, stringers<sup>7</sup>, a transverse bulkhead and parts of the decks are included. Stringers have a length of approximately 3.35 m (Figure 5.12) and HP-profiles are represented as L-profiles in the model. Detailed geometry can be seen in Figure 5.13. Each stiffener is named according to Figure 5.10a and these names will be frequently used throughout this thesis.

#### Material

The hull is made of AH-36 and NV-NS steel, and the material data can be found in Table 5. Both are high tensile steels, and the class notation requirements for the

<sup>7</sup>”Stringer”, ”stiffener” and ”frame” are used interchangeably throughout this thesis.



(a) Name of stiffeners along with the model's extension in x- (longitudinal) and z-direction.

(b) Geometry of model.

Figure 5.10: Overview of FE model.

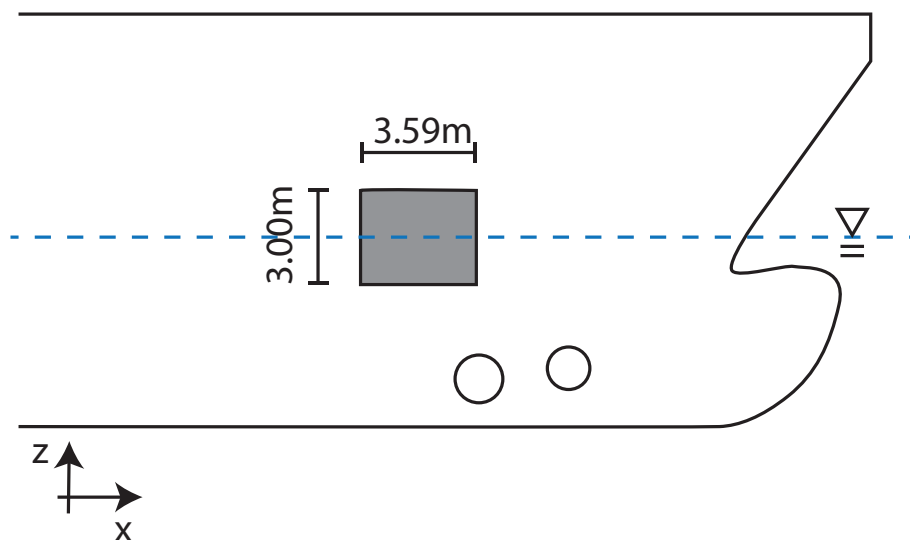


Figure 5.11: The gray box marks the location of the FE model. Outline is based on hull drawings.

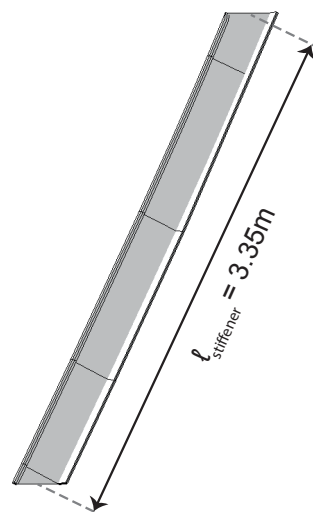


Figure 5.12: Approximate length of stiffeners, taken as the distance between the midpoint of the web at both ends.

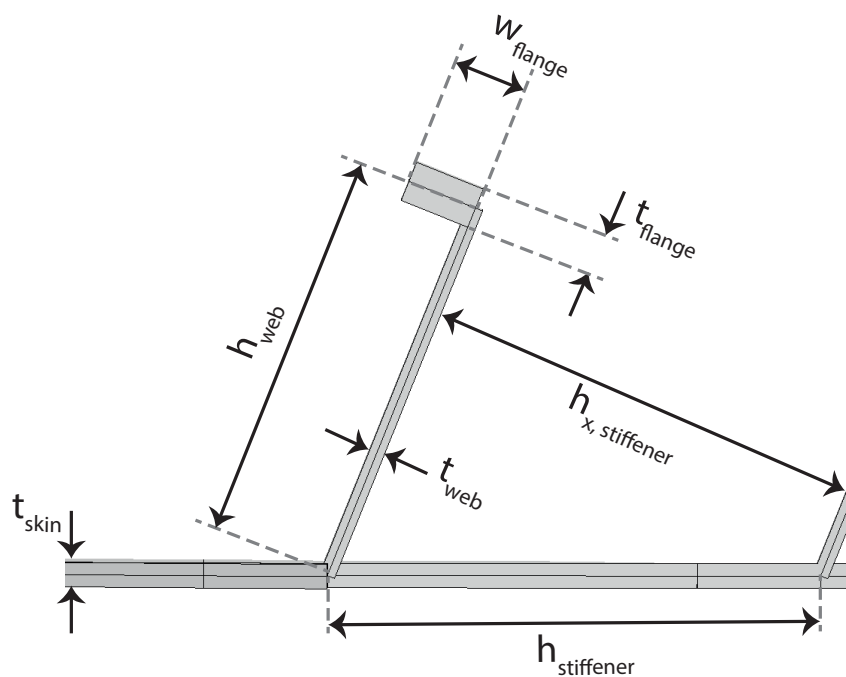


Figure 5.13: Cross section of stiffeners and hull skin. Dimensions corresponding to this figure are found in Table 4.

materials indicate that the values used are conservative (*DNV Ships / High Speed, Light Craft and Naval Surface Craft, 2011*): Actual required ultimate tensile strength is minimum 490 MPa and minimum elongation (strain) is 0.16 for the relevant plate thicknesses and at a temperature of zero degrees.

The von Mises flow rule is used, where yielding occurs as the yield function,  $f$ , is equal to zero:

$$f(\boldsymbol{\sigma}) = \sqrt{3J_2} - \sigma_Y = \sqrt{\frac{3}{2}\sigma'_{ij}\sigma'_{ij}} - \sigma_Y = 0 \quad (5.33)$$

$\sigma_Y$  is the yield stress and  $\sigma'_{ij}$  is a component of the deviatoric stress tensor, and Einstein's summing convention is used. The von Mises flow criterion is pressure invariant, unlike the flow rule introduced in Section 4.1, and forms a circular cylinder along the hydrostatic axis in the principle stress space. It is commonly used for modeling flow of metals.

Linear isotropic hardening was added. It is defined in terms of plastic strain,  $\varepsilon^p$ , see Table 6. The yield function will then be on the form:

$$f(\boldsymbol{\sigma}) = \sqrt{3J_2} - (\sigma_Y + H(\varepsilon_{acc})) = 0 \quad (5.34)$$

where the hardening variable,  $H$ , is a function of the accumulated plastic strain,  $\varepsilon_{acc}$ . The material behaves perfectly plastic for plastic strains larger than 0.05. An illustration of the rheological model of the materials is seen in Figure 5.14, along with an explanatory stress-strain curve. No material failure criterion is implemented in the model, because tearing, rupture, fracturing etc. are not assessed. The load levels and damages that will be looked into will be well below those kind of loads.

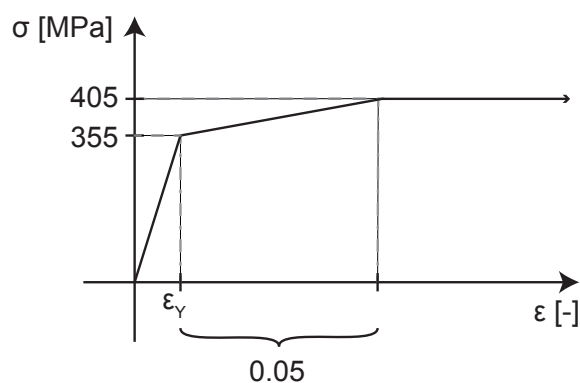


Table 5: Material constants.

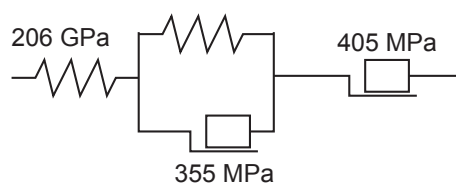
Material name	Young's modulus [GPa]	Yield stress [MPa]	Poisson's ratio [-]
AH-36	206	355	0.3
NV-NS	206	355	0.3

Table 6: Hardening rule.

Yield stress [MPa]	$\varepsilon^p$ [-]
355	0
405	0.05



(a) Linear elastic - plastic with linear hardening - perfect plastic behavior. True stress and strain.



(b) Rheological model consisting of friction elements and linear springs (not valid for unloading).

Figure 5.14: Material model for AH-36 and NV-NS steels.

### 5.3.1 Elements

There are many element formulations available, and each has its pros and cons. Membrane elements are used when the bending action is negligible, i.e. when modeling an air balloon. Plate formulations account for the bending resistance in plates. Elements combining both membrane and bending action, are called shell elements. They are applicable when the thickness of a structural component is much smaller compared to its extension in the two other dimensions. Stiffened panels are typical structural components where shell elements are applicable. Linear four-node quadrilateral conventional shell elements are used in the FE model of the hull<sup>8</sup>. These are called **S4R** in Abaqus, where the **S** stands for shell, **4** is the number of nodes and the **R** for reduced integration. "S4R is a robust, general-purpose element that is suitable for a wide range of applications" as stated in the Abaqus user manual (Systèmes, 2016, Ch. 29.6.2), and they are applicable for both thick and thin shells. In later analyses, Simpson's rule with 5 integration points will be used when integrating over the element thickness, which is sufficient for normal nonlinear applications (Systèmes, 2016, Ch. 29.6.5). Using Simpson's rule will give more accurate results at the element surfaces compared to when using a Gauss quadrature.

*Locking* is a phenomena resulting in elements behaving too stiff. For linear quadrilateral shell elements this is a problem when exposed to bending, and it is called shear locking. A four noded quadrilateral element cannot represent bending according to beam theory due to development of spurious shear strains. These shear strains demand energy and result in that the element becomes too stiff and "locks". A way of preventing this is to use *reduced integration*. When numerically integrating over a four noded element, a Gaussian quadrature rule with four integration points is used for what is called full integration. For reduced integration the quadrature order is reduced by one, resulting in only one integration point for 2D elements, located in the center of the element where shear strains are zero. This, in fact, increases the accuracy and performance in many cases, and at the same time reduces the computational cost of the calculations. However, another problem that may occur when using reduced integration is so-called zero energy modes (also called hourglassing and spurious modes). Since the (reduced) integration point is located at the center for the four noded quadrilateral element, no energy is recorded in pure bending and energy-free straining can occur. Elements deform and become distorted and this can propagate through the mesh. Zero energy modes tend to be a bigger problem for point loads than for distributed loads, but visual inspection should in any ways be done to ensure that potential hourglassing is within acceptable limits. Commercial FE codes often have built-in algorithms to handle hourglassing, and default hourglassing control will be used when doing analyses in Abaqus.

---

<sup>8</sup>Triangular elements are also used in a limited number by automatic mesh generation in Abaqus (see Appendix B for examples). These are called **S3R** and only have one integration point (triangular elements have one integration point for full integration, and cannot be reduced).

### 5.3.2 Mesh Convergence Study

It has been mathematically proven that FEM converges to the exact solution to given partial differential equations as the mesh is refined (Fish & Belytschko, 2007). However, if the mesh is too coarse or in other ways poor, results can be far from reliable. It is therefore of great importance to ensure that the mesh refinement level is adequate. When the element size is such that additional refinement does not significantly change the results, mesh convergence is said to be achieved. Any further refinement will then have little influence and will in most cases be a waste of computational power. In general, a mesh that just fulfills the convergence criterion is therefore preferable in order to make analyses as efficient as possible. For special purposes, however, there can be cases where additional mesh refinement after convergence is beneficial.

The most common way to conduct a mesh convergence study is to simply solve the problem at hand repeatedly with increasing number of elements. Mesh refinement can be done either for the whole model or only locally where stresses are large. The size and complexity of the problem looked into will affect which option is more beneficial. If accurate stresses only need to be simulated in certain regions, it is sufficient to do local mesh refinement while elements can be considerably larger in other regions (NAFEMS, 2016a). High efficiency will then be ensured. Similarly, if the structure consists of almost identical components subjected to similar loads, it will be sufficient to perform a mesh convergence study at one of these specific components (NAFEMS, 2016a, 2016b). An alternative to decreasing the element size is to increase the elemental order and keeping the mesh. This method can be advantageous for complex problems where remeshing is tedious, but for simple problems reducing element size is in general more efficient (COMSOL, 2016). There are also solution procedures that do not allow the use of higher order elements, making mesh refinement the only possibility. It is important to use loads and magnitudes in the mesh convergence study similar to the ones that will be used for the actual analyses. If convergence is achieved for one load magnitude, it does not necessarily make the mesh convergent for an increased load.

For the current model, the highest stress levels occurred in the stiffeners. Since the loads on the different stiffeners are similar, an FE model of a single stiffener including plate flange was considered in the mesh sensitivity study. Scantlings are equal to those found in Table 4 and Figure 5.13, and the material model from Figure 5.14a was used. The subtle curvature of the stiffeners was not included and ends were cut "straight". Ends were fixed (translational DOFs are set to zero:  $U1=U2=U3=0$ ) and the plate flange sides were constrained from translating in the direction of the plate and from rotating around the axis in stiffener direction because of symmetry ( $U1=U5=0$ ). A pressure patch of 33 cm height was applied at the center of the plate, as this will be similar<sup>9</sup> to the cases that will be looked into later. The FE model including the loaded surface can be seen in Figure 5.15. The **Static, general** solution procedure (Newton-Raphson method) was used, as it is efficient and suitable

<sup>9</sup>The heights of the patches used in the later analyses are somewhat larger (409cm and 818cm), but one could argue that a finer mesh is needed for a more concentrated load. Mesh convergence is thus assumed to be valid for later analyses.

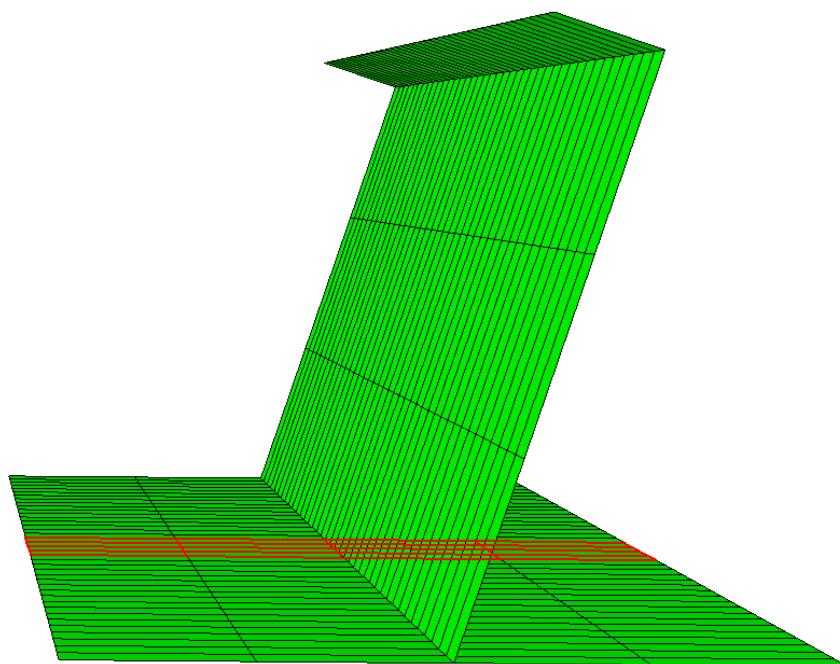


Figure 5.15: FE model used for mesh convergence study. The loaded surface is marked in red. Three elements over the web height are used in this example.

for NLFEA without unloading (for load control) or negative displacements (for displacement control). Two load magnitudes were assessed, based on trial and error. A load of 5 MPa barely resulted in yielding, while a load of 6.25 MPa resulted in formation of a plastic hinge and larger deformations. Convergence was checked for stresses and displacements. Stresses were evaluated at the midspan in the top of the web. Displacements were evaluated at the midspan of the stiffener in the joint between plate and web, in the direction perpendicular to the plate. See Figure 5.15 for an illustration. Convergence was assessed for the linear quadrilateral elements **S4** and **S4R** (Section 5.3.1).

Figure 5.17 and 5.18 display results for 5 MPa and 6.25 MPa loads, respectively. Already with two elements over the web height the stress has converged for **S4R** for the 5 MPa load, whereas **S4** converges at five elements, approximately. Displacements converged a little slower, in contrast to what was expected since displacements have a higher convergence rate (Mathiesen, 2014, Ch. 12). **S4R** performed better than **S4** since convergence was faster and the stress field obtained using **S4** was more uneven and stress gradients were larger. **S4R** was used in all later analyses due to its high performance and convergence rate. For the higher load level and larger deformations, convergence was slower since more nonlinear effects took place. 10 elements over the web height was sufficient to give good results, but the results had completely converged when more than 20 elements were used. The models used in later analyses have 21 elements over the web height. The element size in other parts of the model varies and is larger in regions where large deformations and stresses were not expected or observed. Some of these mesh details can be seen in Appendix B. The mesh is regular in the plate and the stiffeners, with a few exceptions. A

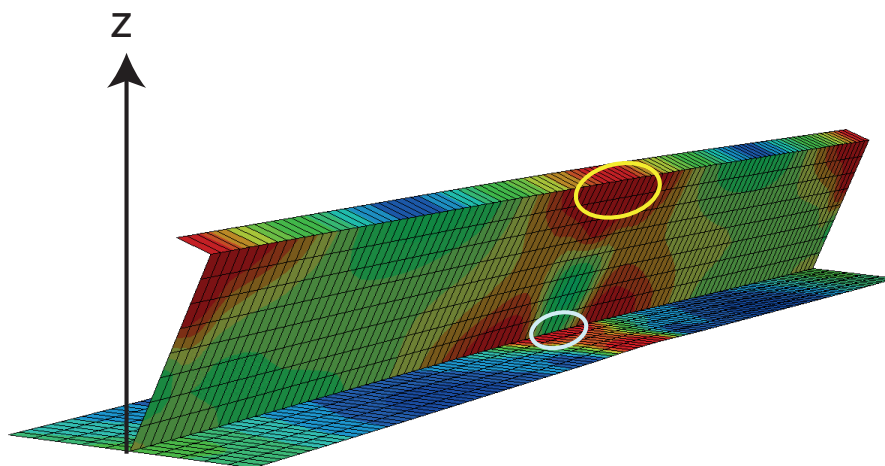
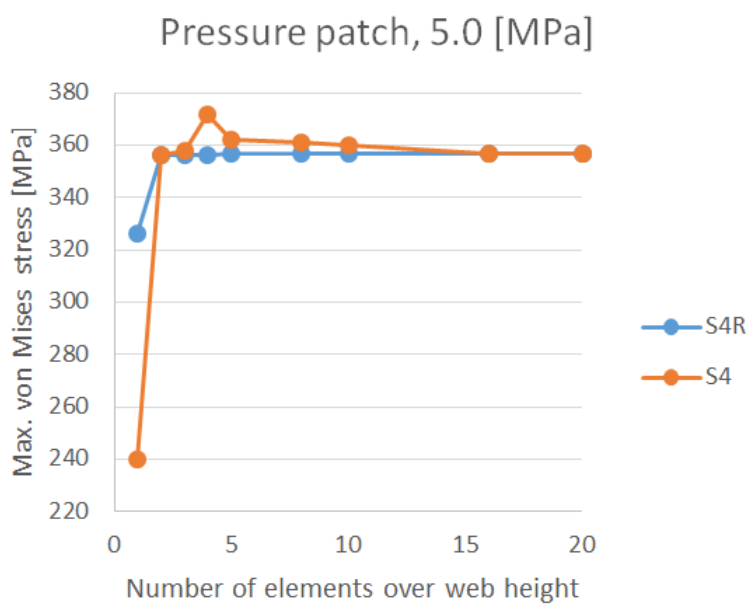
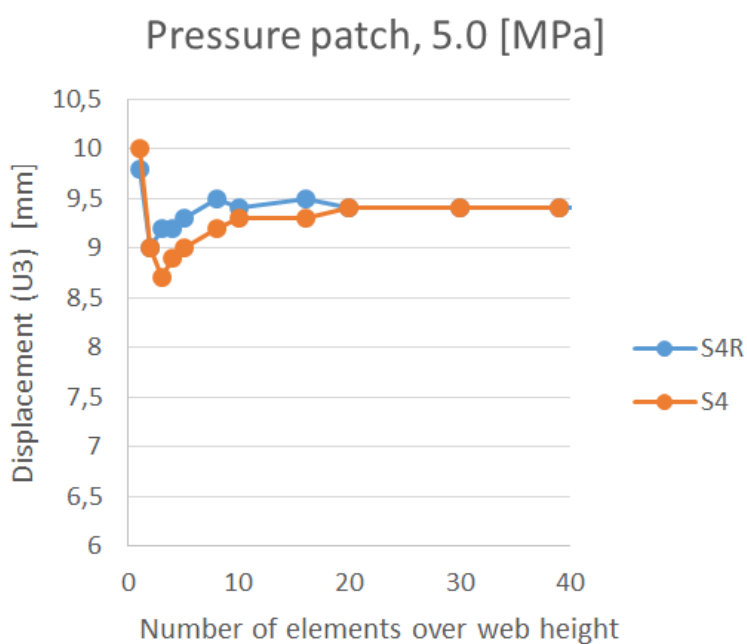


Figure 5.16: FE model used for mesh convergence study. The yellow ellipse marks the location where stresses were extracted and the white ellipse marks the location where displacements were extracted (in direction of  $z$ ).

coarser mesh is used in the top and bottom deck, and more elements are distorted. Distorted elements are in general unfavorable, but since strains and stresses will not be looked into in these regions it will be of less importance. Mesh convergence was not assessed for the plate (skin) because stress levels were smaller than in the frames. The refinement was about the same as for the frames, which in any way is finer than what is normal for laterally loaded plates.

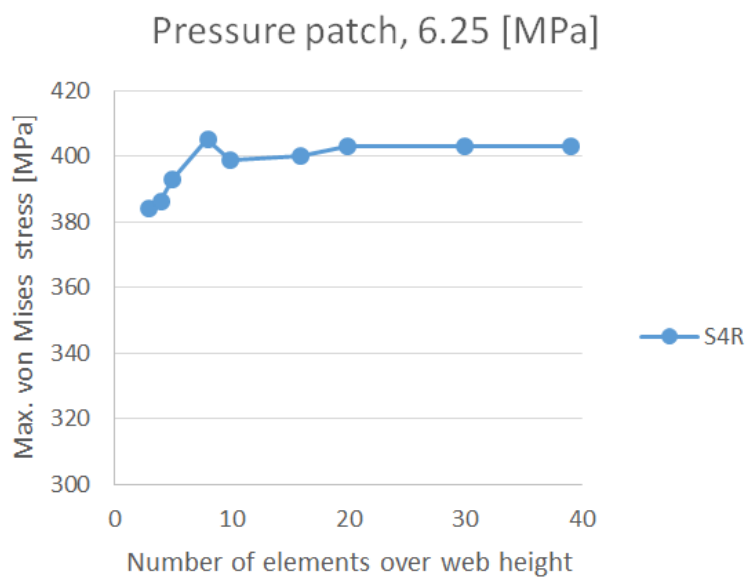


(a) Maximum von Mises stress at midspan.

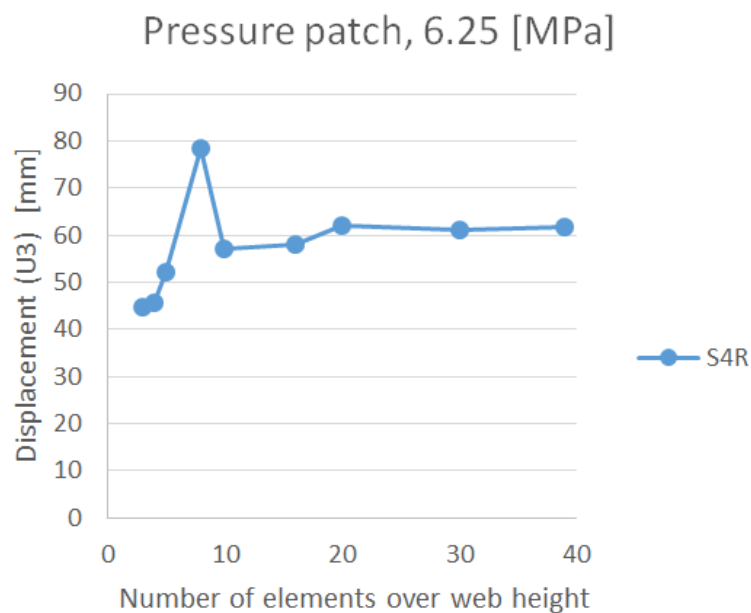


(b) Maximum lateral displacement in joint between web and plate at midspan.

Figure 5.17: Mesh convergence with a 5 MPa load. S4R and S4 elements were assessed.



(a) Maximum von Mises stress at midspan.



(b) Maximum lateral displacement in joint between web and plate at midspan.

Figure 5.18: Mesh convergence with a 6.25 MPa load. S4R elements were assessed.





## 6 Analyses and Results

In this section the analysis-procedures and results will be explained in detail. Various load cases with different solution procedures were to be assessed in this thesis. Python-scripting was therefore used extensively and Abaqus analyses were mostly done in batch mode to efficiently be able to generate a lot of analyses and data. The scripts that have been developed are attached in Appendix A.

### Loads

One of the goals with this thesis was to analyze uniform pressure loads of different widths and heights, and at different locations. A script was made to isolate the hull skin from the transverse frames and to create an element surface (Appendix A.1). In this way rectangular<sup>10</sup> patches of arbitrary sizes, located at arbitrary positions could easily be made. These surfaces were loaded with an uniform pressure (load control). The elements subjected to an uniform load patch will not deform uniformly, so it would not have been feasible to use displacement control. Furthermore, by deciding step sizes for width and height, input files for multiple load cases could be generated. All job-files were named with, as an example, "(...)-W2-H0" at the end. The number behind W and H denotes the number of step widths/heights that is added to the "default" width. These names will be used when presenting results later on. The initial values and step sizes used throughout this thesis are found in Table 7. Thus, the width and height in the example above will be 0.94 m and 0.41 m, respectively. Figure 6.1 shows how load width is increased.

Table 7: Load patch dimensions

	Initial value [m]	Step value [m]
W	0.312	0.312
H	0.409	0.409

### Boundary Conditions

Ideally, the Boundary Conditions (BCs) of the model should have been a combination of springs with different stiffnesses along the model's boundary, in order to represent the surrounding structures exactly. This was not feasible since detailed analyses of the whole hull would have had to be done in order to determine these stiffnesses. An alternative would have been to extend the model in all directions and make, for example, fixed BCs at the outer boundaries. The longer the relative distance from the BCs, the smaller the influence of the BCs will be, which is known as the *St. Venant's principle* (Timoshenko, 1934; Love, 2013). It would, however, not be feasible to take such measures because modeling is time consuming and the computational costs of

<sup>10</sup>Since the box is defined by two corners in the global x,y,z-space, it is only the projection of the patch onto the y,z-plane that is rectangular. Because the ship side in the bow area is inclined, the actual shape of the load patch differs some from that of a perfect rectangle

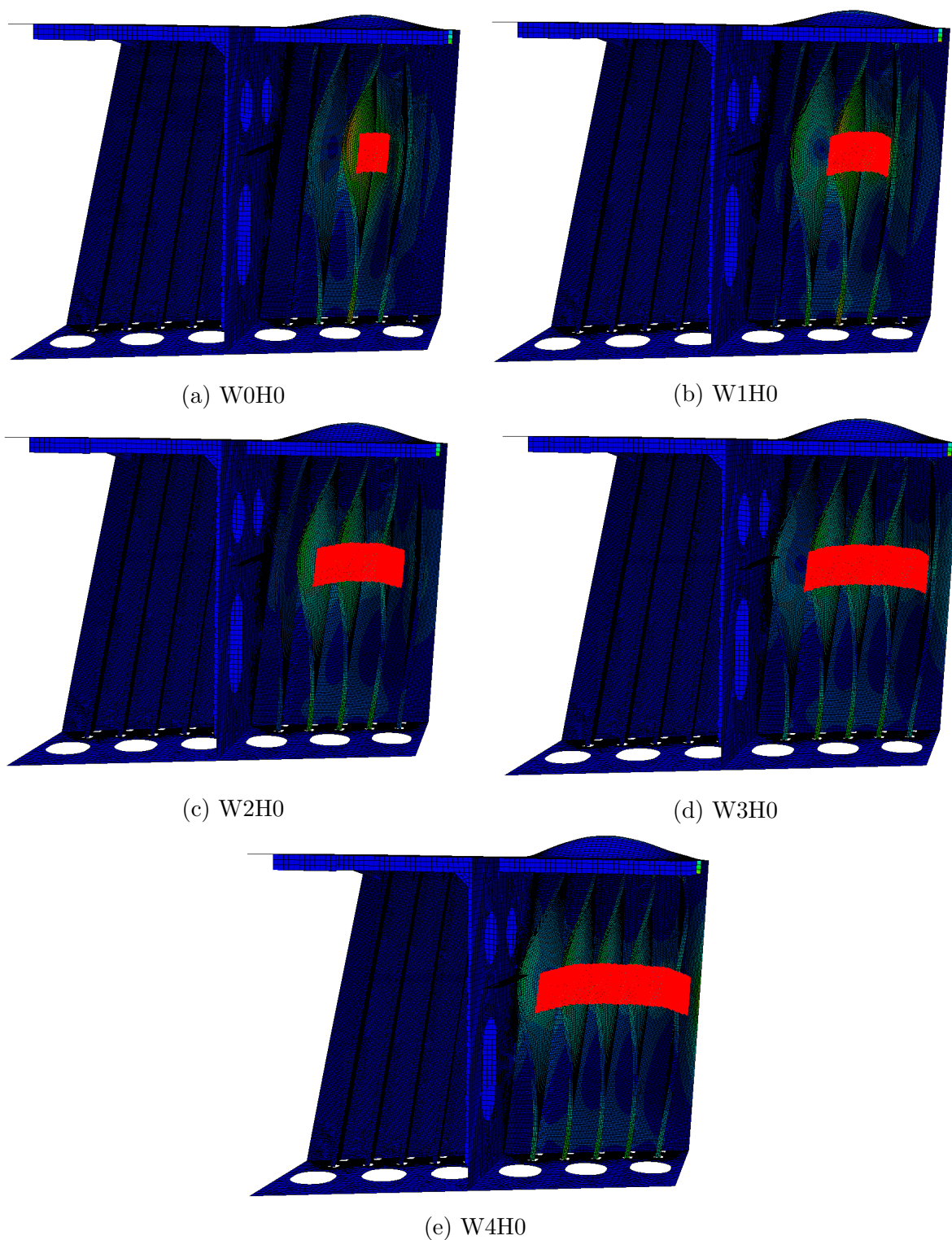


Figure 6.1: Examples of resulting deformations for increasing load patch width, obtained from linear analyses and presented with a large deformation scale factor. Load patches are marked in red. More stiffeners are activated as the load patch width increases.

the analyses would increase. Stress data have not been extracted directly at the boundaries of the model in order to reduce the influence of the BCs. Furthermore, two different BCs have been evaluated.

Because the hull has extra ice strengthening in the waterline area, half of the transverse stiffeners do not continue to the deck above. To compensate for an otherwise low moment bearing capacity at the top ends of these stiffeners, brackets are connected to the deck stringers making the hull stiffeners capable of transferring moments at the top end. These brackets can be seen in the top right region of Figure 6.9. All stiffeners continue through the deck below and they can therefore transfer moments to some extent at the bottom ends. Shear forces in stiffeners will mainly be transferred to the deck through brackets at the top and through lug plates at the bottom ends of the stiffeners.

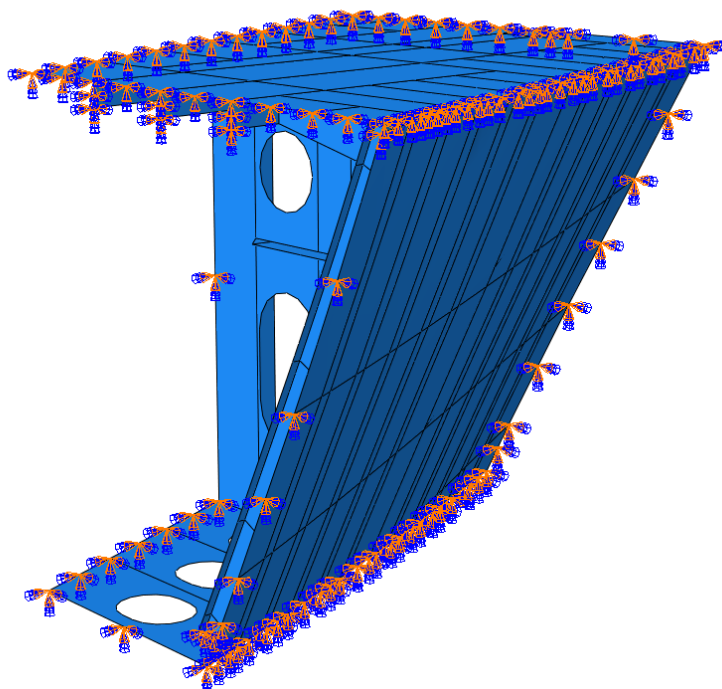
The first set of BCs is called "all fixed". All outer edges, in addition to the lower stiffener ends, are fixed in translational and rotational DOFs ( $U_1=U_2=U_3=U_4=U_5=U_6=0$ ). Figure 6.2 shows these BCs.

Since only the outer edges are fixed on the top, moments will mainly be transferred to the top deck through the brackets. The top ends of the stiffeners therefore exhibit more rotational flexibility than the bottom ends. The top ends of the stiffeners which continue to the deck above will with these BCs be more free to rotate than in reality. This will result in that more load is carried by the bottom half of the stiffener, which is a conservative assumption. What is more concerning are the fixed lower ends of the frames. In reality the shear forces from the stiffeners are transmitted to the lower deck through the lug plates connecting them. This is not simulated with the current BCs. Surrounding structure will provide some rotational stiffness at the boundaries of the skin, but fixed is somewhat unconservative. However, only limited extra rotational stiffness is given because it is only the nodes along the outer edges that are restrained from rotating. Bulkheads in front and back will carry a very limited part of the load on the plates. Stringers therefore carry the main part, especially when the loads are located at the center of the plate. The rotational BCs at the skin edges will therefore not have a big influence on the capacity.

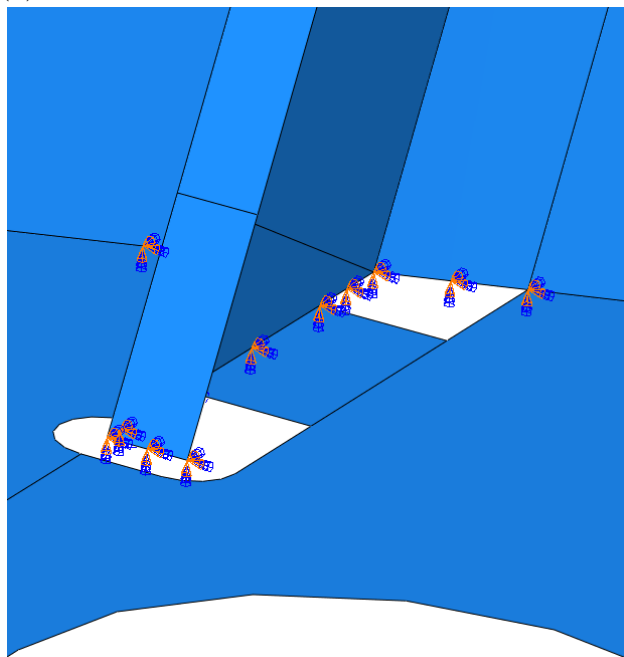
The second set of BCs is called "partly fixed". BCs are shown in Figure 6.3 and explained in the following list.

- No rotational BCs are introduced.
- The lower ends of the stiffeners are free to move in the transverse direction (y-direction), ensuring that shear forces will mainly<sup>11</sup> be transferred to the bottom deck ( $U_1=U_3=0$ ).
- The top and bottom edges of the skin are only fixed in the global z-direction ( $U_3=0$ ).
- The fore and aft edge of the skin, along with fore and aft deck edges, are fixed in all three translational DOFs to represent the bulkheads ( $U_1=U_2=U_3=0$ ).

<sup>11</sup>Because of the ship side's inclination, a component of the stiffeners' shear forces will still be carried by the BCs.

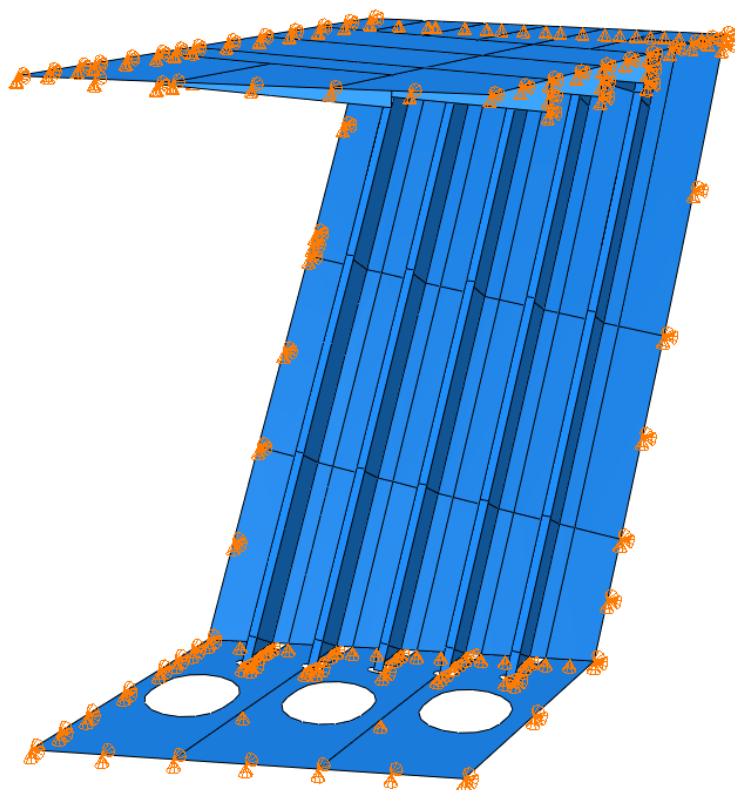


(a) "All fixed" boundary conditions seen from aft.

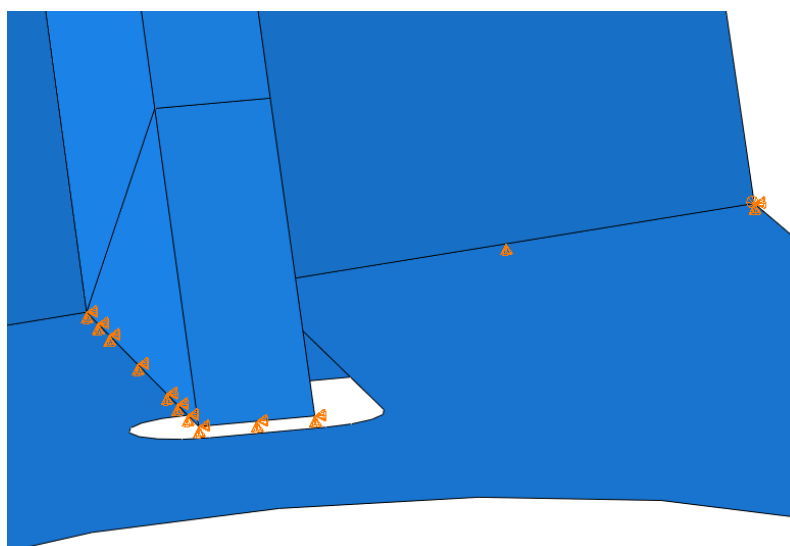


(b) "All fixed" boundary conditions at lower ends of stiffeners.

Figure 6.2: "All fixed" boundary conditions. Orange arrowheads indicate that translational DOFs are fixed in the direction of the arrow; blue double arrowheads indicate that rotational DOFs are fixed around the axis of the arrow.



(a) "Partly fixed" boundary conditions seen on the "half model".



(b) "Partly fixed" boundary conditions at lower ends of stiffeners.

Figure 6.3: "Partly fixed" boundary conditions. Orange arrowheads indicate that translational DOFs are fixed in the direction of the arrow.

- Lines in the bottom (tween) deck at the location of deck stiffeners are fixed in z-direction ( $U_3=0$ ) (Figure 6.3a).
- The inner edges of the decks are free to translate in the longitudinal direction of the ship ( $U_2=U_3=0$ ).

The idea was to mimic the stiffness from the surrounding structure in a more realistic manner. These are more conservative since not all DOFs are fixed, because moments will be "moved" to the center of the plate field. One should be aware that moving moments may increase shear load in some elements because of load carrying redistribution.

## Reduced FE Model

Storage space limitations turned out to be a problem when conducting the analyses. Measures had to be taken and resulted in an FE model of reduced size. Only loads centered between the rear two bulkheads were to be assessed for the nonlinear analyses, so the front region, including the bulkhead, was removed. This reduced FE model is referred to as the "half model", because of it spanning half the length of the original model in the longitudinal direction. The original FE model is referred to as "whole model" in the following results. For the linear analyses, storage space and computational time was not an issue, so the "whole model" was used exclusively.

The "whole model" consists of approximately 180 000 elements and nodes, while the "half model" consists of approximately 80 000 elements and nodes. The analyses were run on NTNU's "imtmal09" remote server. More than 30 nonlinear analyses were executed. Multiple CPUs (10) were used (for nonlinear analyses), and the run time for each job was in the ballpark of three hours. Some of the scripts used for post-processing were equally time consuming, so running time was an issue.

## 6.1 Linear Analyses

Linear FE analyses were conducted to calculate the load at first yield. The set of BCs named "all fixed" was used for all the linear analyses. Since a linear elastic material model is used, only the Young's modulus,  $E$ , and the Poisson's ratio,  $\nu$ , from Table 5 were needed to define the material. Uniform loads with a magnitude of 1 MPa were used. Stresses in the the whole model were looked into at first, both in top, middle and bottom section points of the elements. The stress levels in the plates and in other regions were in general smaller than stress levels in the stiffeners. Because of this, yielding in stiffeners was used as capacity criterion for first yield.

For laterally loaded beams, first yield will occur either at the center of load or at the supports. Since a load centered in the midspan of a stiffener will result in the largest (bending) stresses, load patches are centered at stiffener midspan for all load cases (see Figure 6.1 for an illustration of the location of the loads). The longitudinal (x-direction) position of the load patches were applied at three different locations: either centered on the middle frame aft of the bulkhead, the frame fore of that or the frame in the middle, fore of the bulkhead. These frames are named L2, L3 and L5,



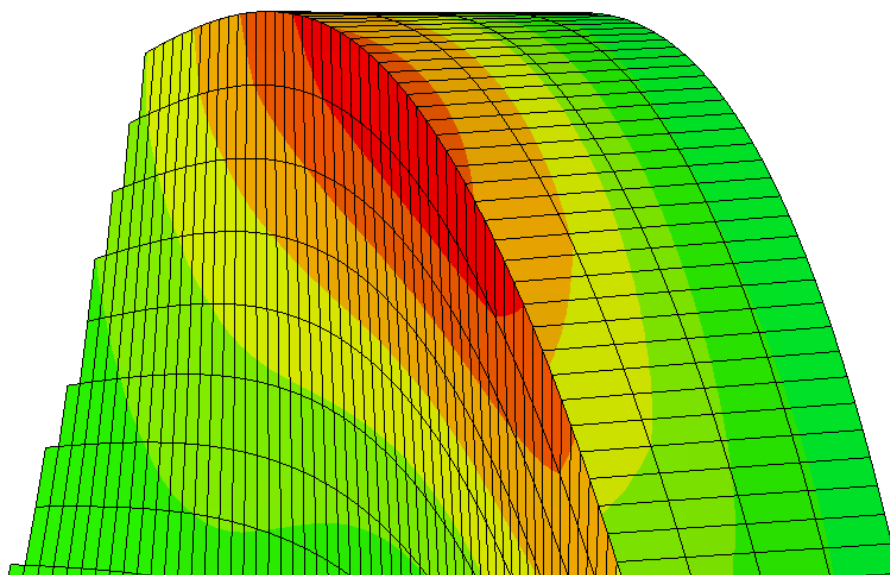


Figure 6.4: Illustration of stress distribution in a stiffener at midspan. Higher stress values are marked in red and it is seen that the web covers the regions with the highest values.

respectively, according to Figure 5.10a. The frames will yield due to shear, bending or a combination of these. The most critical regions are at the supports and at the center of the load, where plastic hinges would occur with excessive loading (not assessed in linear analyses).

Onset of tripping<sup>12</sup> of the stiffeners tends to move the stresses towards the junction between web and flange, making the web cover the regions of the stiffeners with highest stress values. This was confirmed by visual inspection in the post-processor of Abaqus (see Figure 6.4) and it was therefore concluded that stresses only need to be evaluated in the web to find the maximum values. Local coordinate systems were made near the top and bottom ends of each stiffener, aligned such that the  $x,y$ -plane is the web and the  $y$ -axis is perpendicular to the plate. A path in Abaqus is a user defined line aligned with element edges, from which different data outputs can be made. Such paths were made through the height of the webs, aligned with the  $y$ -axes of the local coordinate systems. Local coordinate systems and a path can be seen in Figure 6.5. An additional path and coordinate system was made at the midspan of the middle girder, L2. This is the stringer subjected to the most severe stresses since it is farthest away from the bulkheads. A total of 21 paths were assessed. One of the reasons why the mesh had to be regular in the web was to be able to make straight paths.

The normal stress ( $S11$ ), shear stress ( $S12$ ) and von Mises stress ( $Mises$ ) were extracted from these paths. The von Mises stress is invariant to coordinate transfor-

<sup>12</sup>Tripping is a phenomenon where stiffeners rotate about the plate junction, and is a form of lateral torsional buckling. See for example the deformation modes of the stiffeners in Figure 6.1.

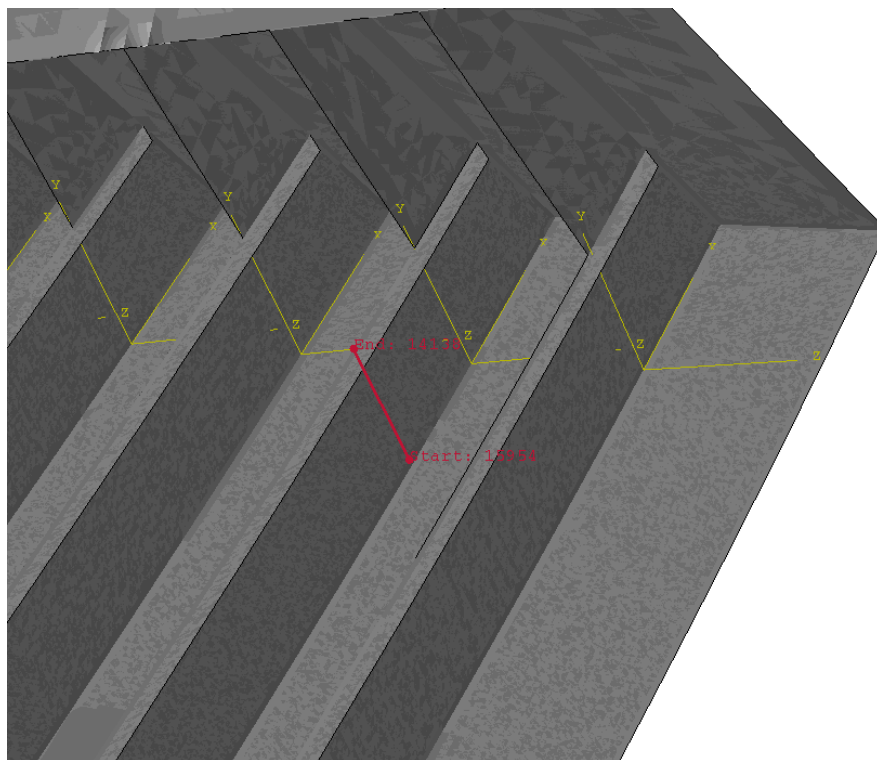


Figure 6.5: Local coordinate systems are marked in yellow and the upper path for stress extraction on stiffener L1 is marked in red.

mation and could be extracted directly, while coordinate transformations had to be done for obtaining the other two components with correct values. Plots of stress distribution as a function of the web height were made to confirm that stresses developed as expected. A quadratic distribution was observed for the shear stresses and a linear distribution for the axial stresses, which can be seen in Figure C.1 in Appendix C.1. This was also a reason for why 21 elements were used over the web height in the FE model. With fewer elements, curves would not have been as smooth, especially not using linear elements. The reason for looking into the different components was partly because it was interesting to see which stress component dominates (i.e. if failure occurs due to bending or to shear). Another factor is that full scale ice load measurements are scheduled for the vessel in the winter of 2017. The strain gauges cannot measure von Mises stress directly, so preparing scripts and analyses data for looking into separate stress components makes the work of this thesis more applicable for later use.

”Local” bending action in the web causes stresses at the two sides to have different values, illustrated in Figure 6.6. A single check was done for the WOH0 load distribution at the location of the highest stresses, and a difference in von Mises stress of 7 % between the two sides was found. For the planned full scale measurements this must be taken into account, for example by using strain gauges on both sides and taking the average. Stresses at the mid-section point will be used in later analyses, in order to exclude the effect of local bending. The reason for this is that the local bending can be seen as a secondary effect which will not affect the load bearing capacity of the stiffener. Figure 6.7 illustrates how the bending contribution can be excluded by



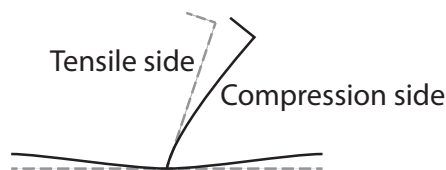


Figure 6.6: Local bending action in web due to lateral deformation of stiffeners.

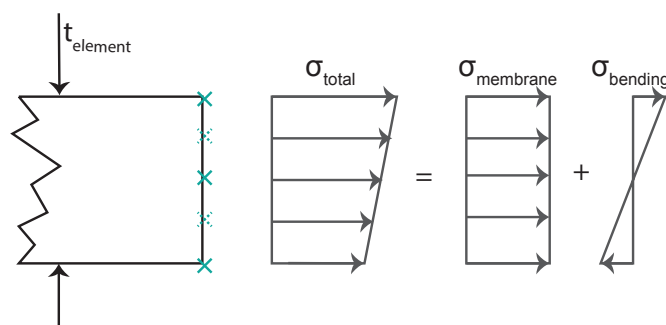


Figure 6.7: Shell element with rendered thickness ( $t_{element}$ ). Section integration points are marked with blue crosses, and the dashed crosses indicate that data for these section points were not written to the result files. Using the value at the mid-section point will exclude the bending contribution  $\sigma_{bending}$ , leaving only the membrane stress,  $\sigma_{membrane}$ .

using the mid-section integration point. Note that the membrane stress in Figure 6.7 represents the bending stress (S11) for the stiffener.

The maximum values of stress components over each path were evaluated. A script was made to do the following (found in Appendix A.2):

- Open `.odb`-files (Abaqus result files).
- Create paths and local coordinate systems.
- Change coordinate system and create data output.
- Evaluate the maximum value of the respective stress components over the cross section.
- Write data to a `.csv`-file.

The utilization with respect to yielding,  $\eta_Y$ , was determined as follows:

$$\eta_Y = \frac{\sigma_{max}}{\sigma_Y} \quad (\text{For shear: } \eta_Y = \frac{\tau_{max}}{\frac{\sigma_Y}{\sqrt{3}}} = \frac{\tau_{max}}{\tau_Y}) \quad (6.1)$$

The capacity with respect to yielding,  $C_Y$ , was determined as follows:

$$C_Y = \frac{\sigma_Y}{\sigma_{max}} \quad (\text{For shear: } C_Y = \frac{\tau_Y}{\tau_{max}}) \quad (6.2)$$

$\tau_{max}$  is the maximum measured shear stress (S12),  $\sigma_{max}$  is the maximum measured stress (Mises or S11),  $\sigma_Y$  is the yield stress and  $\tau_Y$  is the yield stress for pure shear.

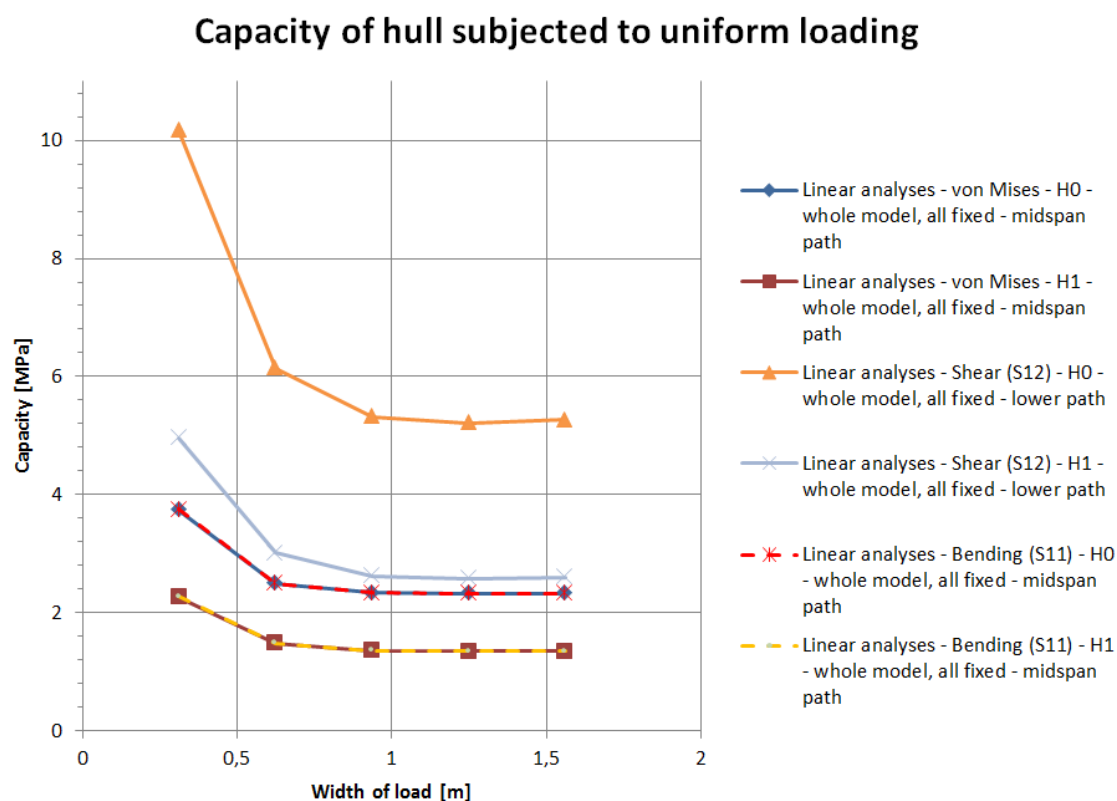


Figure 6.8: Load capacity as a function of load patch width. First yield is used as failure criterion.

## Results from Linear FEA

Microsoft Excel was used for post-processing the obtained maximum values and an illustrative Excel document organizing the data was made. Since the Excel format is not ideal for presenting in paper, only the most important results will be presented here, but the Excel sheet is also electronically attached, see Appendix D.

In all, the response for 30 different load distributions was analyzed. Five load patch widths (W0-W4), two heights (H0-H1) and three load-locations (L2, L3 and L5) were used. Loads located farthest away from the bulkheads yielded the lowest capacities and for that reason, only the loads centered at the L2-stiffener will be analyzed, assessed and discussed further in the thesis. Capacity curves obtained from the linear analyses are presented in Figure 6.8, and the capacities were calculated according to Equation (6.2).

It comes clear from the curves that bending stresses will be dimensioning and determine the overall capacity. Bending stresses were most critical in the midspan of the L2 stiffener, and the shear stresses were largest at the lower end. Note that the shear force in the stiffener is more or less constant below and above the load patch. The maximum capacity was 3.7 MPa and the pressure curve converges to 1.3 MPa as the width of the load increases.

## 6.2 Nonlinear Analyses

In order to determine the ultimate strength of the hull, NLFEA was executed. One of the goals with this thesis was to estimate the residual strength after onset of yielding. Only load patches centered at the L2-stiffener were assessed, with the same patch sizes used for the linear analyses (Section 6.1). Analyses for other load locations were conducted, but they yielded larger capacities and were therefore not of interest. Both the "whole model" (used in linear analyses) and the "half model" were utilized. Due to tripping of the stiffeners, a reduction of strength was experienced for some load cases. Since the `Static, General` procedure (Newton-Raphson method) cannot simulate unloading using load control, the arc length method `RIKS` was used. 1 MPa was used as a reference load as it was seen from the linear analyses that the capacities were well above this level for all load cases looked into. Strains, stresses, reaction forces and more were requested as field and history outputs from the analyses. For more detailed analysis-data, see the input files in the electronic attachments (Appendix D). The material model used is the one described in Section 5.3 and material data can be found in Table 5. Input files for analyses were generated using of the script found in Appendix A.3. To see how the BCs influence the results, both "partly fixed" and "all fixed" were utilized. Note that if not explicitly stated in figures and results, "all fixed" BCs have been used. Additional results that have not been presented in the thesis can be found in the electronic attachments (Appendix D).

### 6.2.1 Load-Displacement Curves

Load versus displacement curves were made and loads are represented as pressure<sup>13</sup> or force. Force was taken as the total reaction force along the boundaries of the model. Displacement was taken as the lateral displacement of the node located at the center of the load. A local coordinate system was created at that node and the z-component of the displacement is used as the displacement in the load-displacement curves. This can be seen in Figure 6.9, where the local coordinate system is marked in red. A script which automatically writes the relevant data output for multiple analyses to a file was written (Appendix A.4). Load-displacement curves are shown in Figure 6.10, 6.11 and 6.12. Note that since failure is not implemented in the material model, load displacement curves can not be trusted at very large displacements due to excessive straining.

To be able to see how load is distributed to different stiffeners, shear stresses at each path were numerically integrated over the web height and thickness. Then, by summing the shear force in upper and lower path for a stiffener, the total load carried by the stiffener was obtained. Coordinate transformation had to be done at every path to get correct values of shear stress. This had to be done for every increment, which turned out to be computationally costly. For that reason, only the three central stiffeners (L1, L2 and L3) were evaluated for shear force. The script developed for this purpose can be found in Appendix A.5 and some resulting load

<sup>13</sup>LPF is the Load Proportionality Factor. "LPF" and "pressure" is used interchangeably in some of the plots because the two take the same value since the reference load was 1 MPa.

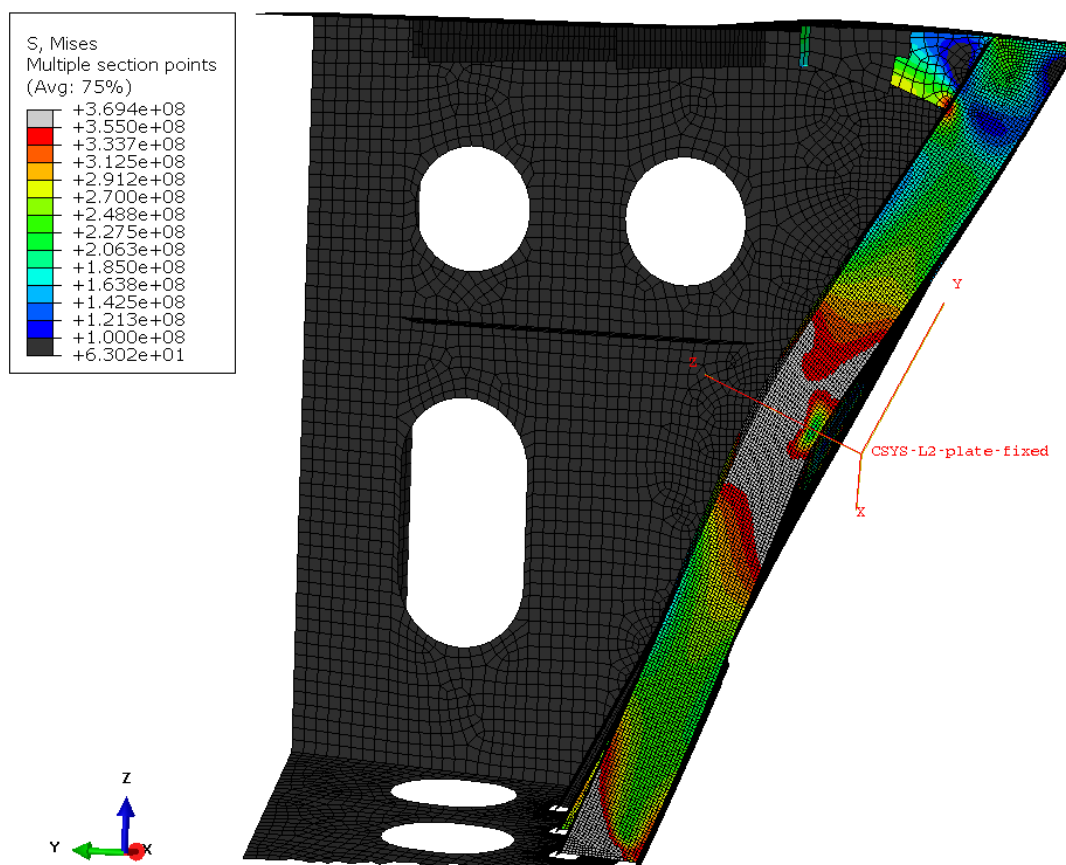


Figure 6.9: Deformation is measured at the center of the load (origin in the coordinate system CSYS-L2-plate-fixed), in the direction of the load (z-axis of CSYS-L2-plate-fixed). Note the plastic hinges at the midspan and at the lower end of the load, marked in light gray.

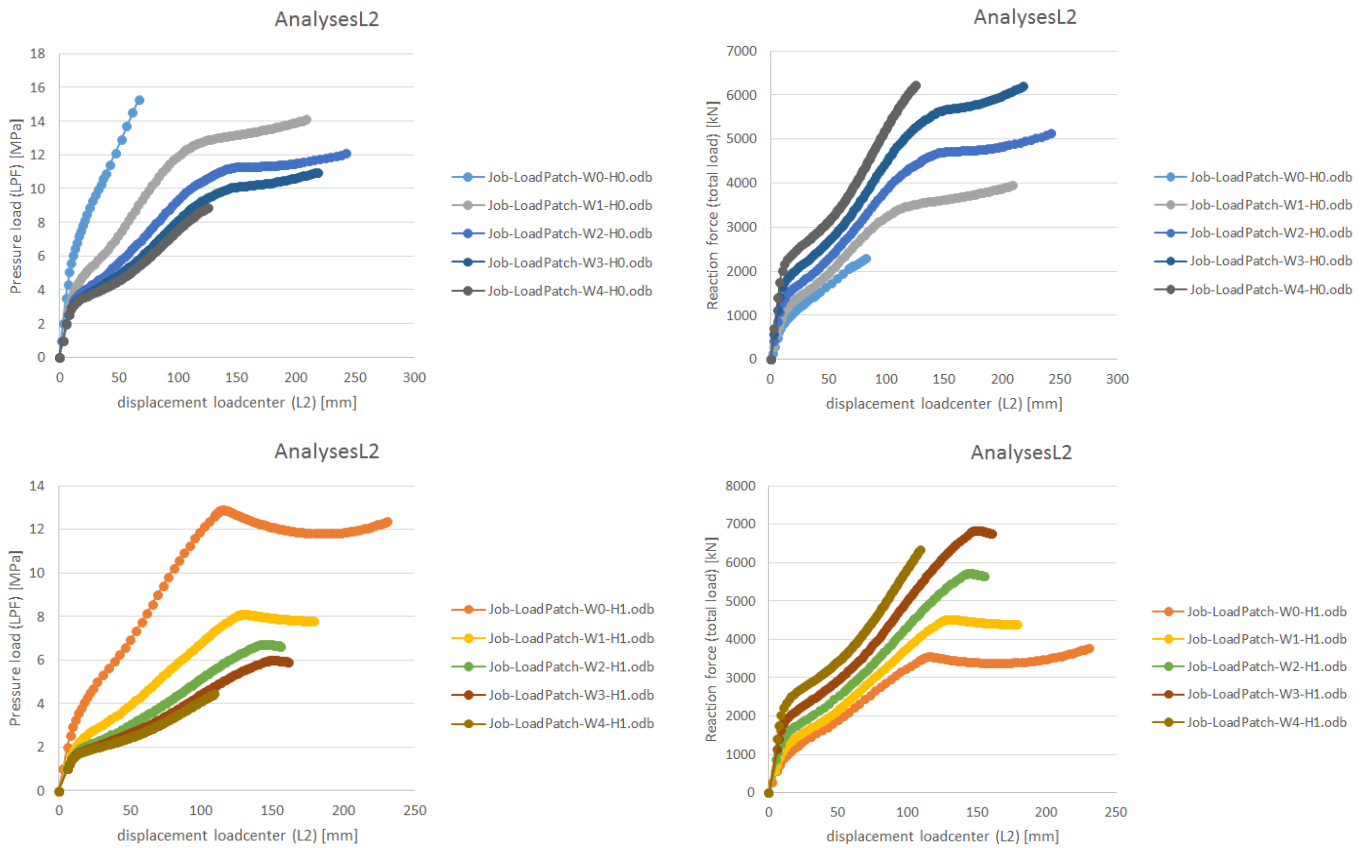


Figure 6.10: Load-displacement curves for large deformations.

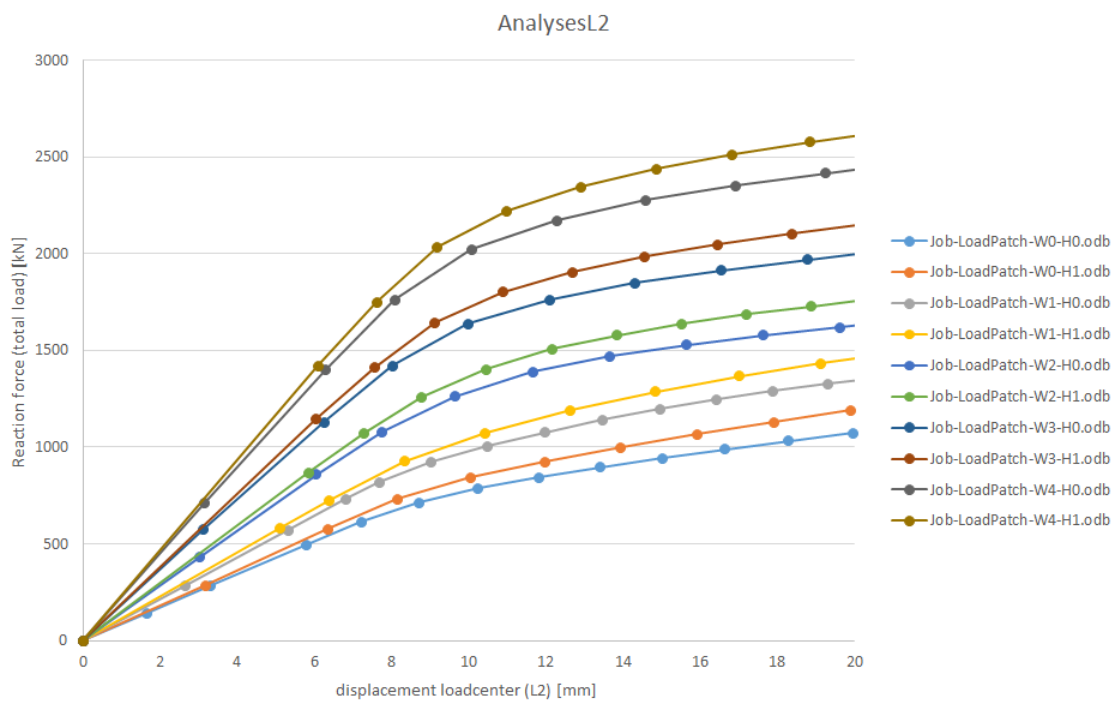


Figure 6.11: Load-displacement curves at onset of yielding. Reaction force on the second axis.

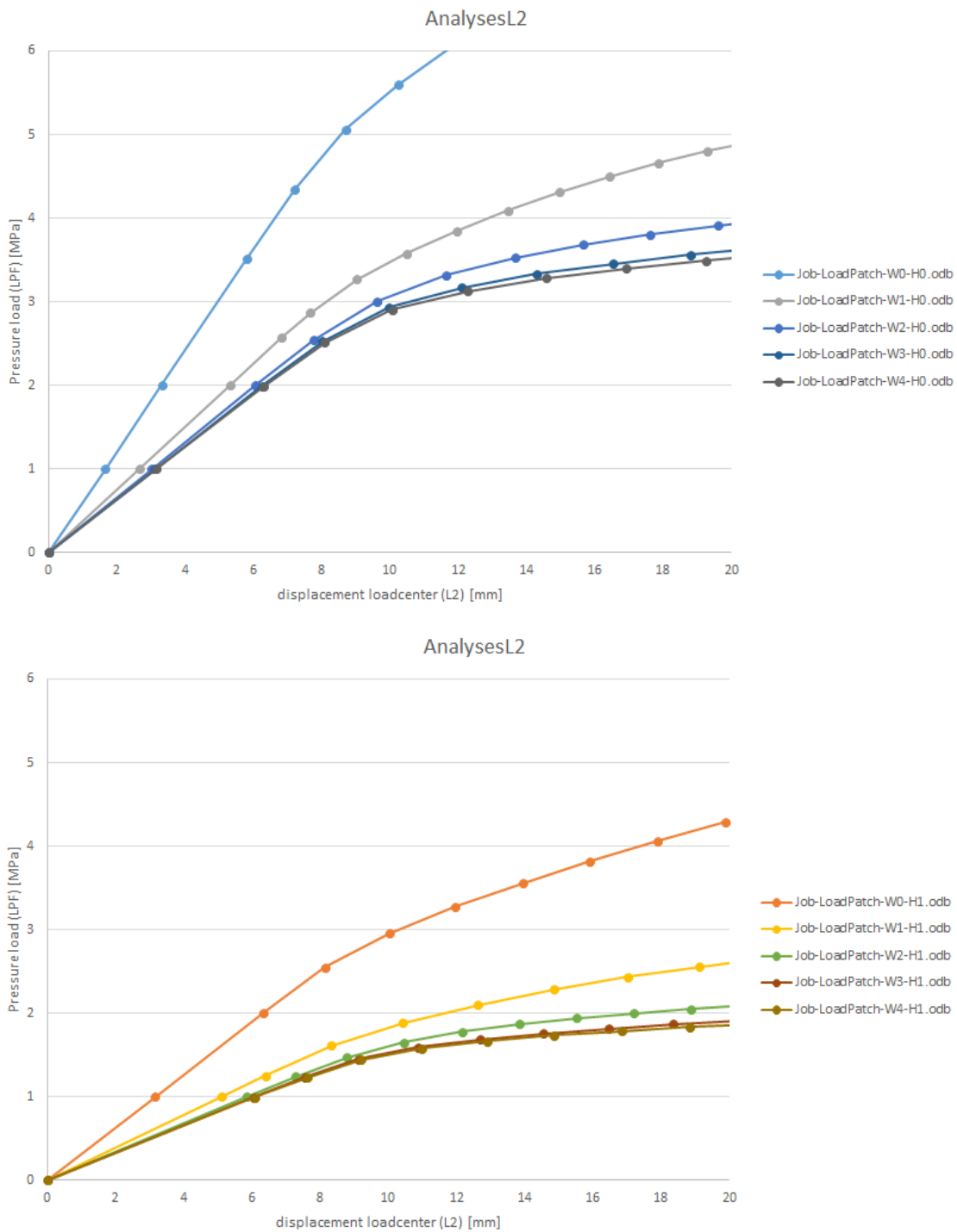


Figure 6.12: Load-displacement curves at onset of yielding. Pressure load on the second axis.

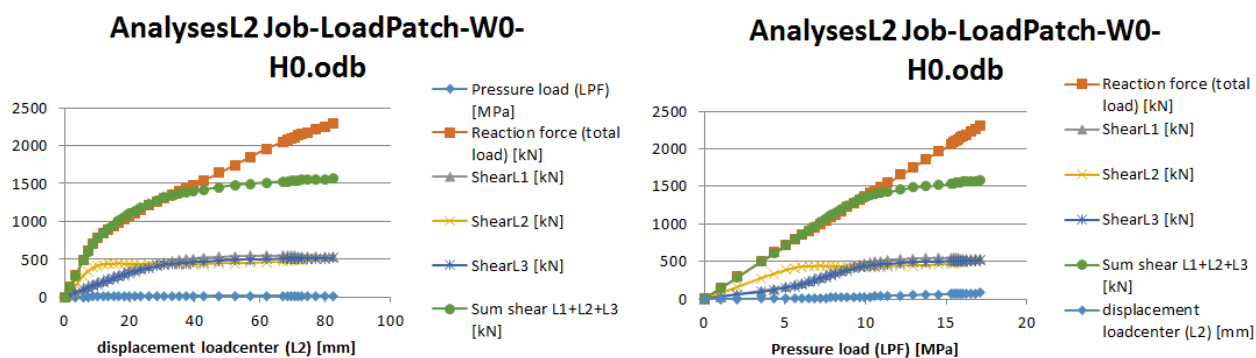


Figure 6.13: Load-displacement and "load-load" curves for large deformations.

deformation curves can be seen in Figure 6.13 and 6.14. "Reaction force" is the total reaction force on the model's boundaries, which is the same as the total applied force on the model. "ShearLX" is the shear force carried by stiffener LX. "Sum shear" is the sum of shear forces carried by the three central stiffeners. In Figure 6.13 it is seen that all the load is carried by the three central stiffeners for small loads. As plastic hinges are formed in the three stiffeners, other stiffeners are activated and the "Reaction force" and "Sum shear" curves split up.

## 6.2.2 Ultimate Strength

Since material failure was not implemented, an alternative "failure" criterion had to be defined. A criterion based on allowable permanent sets was made and is given as a maximum lateral deformation ( $\delta_{permanent}$ ) of the stiffener midspan.  $\delta_{permanent}$  is given in a percentage of the stiffener's span, and the percentages evaluated are 0.5 % and 1.0 %, corresponding to 16.75 mm and 33.5 mm with a stiffener span of 3.35 m. These values were agreed upon after a discussion between the author and the supervisors at DNV GL (Nyseth & Hareide). It was seen from the analyses that the equivalent plastic strain,  $\varepsilon_{eq}^p$ , was no more than 0.045 at the worst locations, which is well below the minimum strain requirements (Section 5.3). The steel material is also assumed to have a steeper hardening than what is used in the material model, so the criterion is assumed to be on the conservative side. The idea is that these are deformations that can be acceptable for a ship without having an urgent need for repair. The deformations are also in line with what was categorized as "typical ice-induced damages" by Kujala and Ehlers (2013). Capacities calculated from these requirements will be referred to as "ultimate strength", even though the true ultimate strengths presumably are larger.

A simple way of simulating unloading is illustrated and described in Figure 6.15. The initial stiffness (in the linear range) from a load displacement curve is used to make a tangent line. This line is then parallel shifted so that it crosses the displacement-axis at wanted allowable deformation ( $\delta_{permanent}$ ). The point where the two curves intersect defines the capacity, or ultimate strength in this case. It is here assumed that the unloading curve is linear with the same stiffness as the linear stiffness, which have been shown to be a good approximation. Curves like the ones seen in

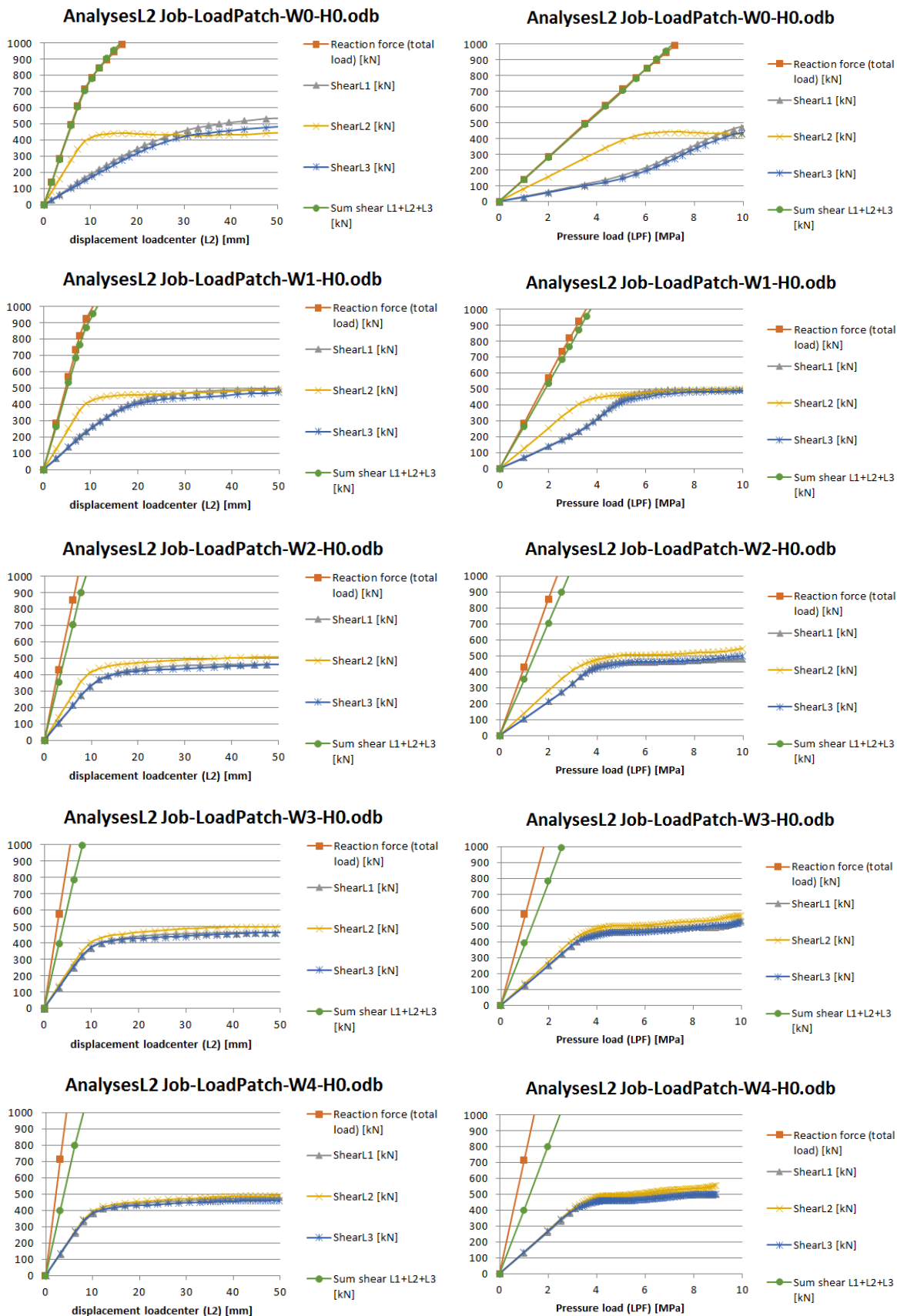


Figure 6.14: Load-displacement and "load-load" curves showing load carrying distribution for the three central stiffeners for an increasing load width.



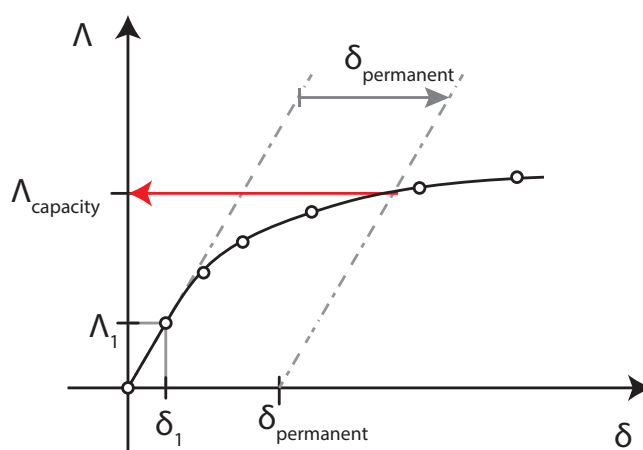


Figure 6.15: Procedure for obtaining capacities.  $\Lambda$  represents load,  $\delta$  represents displacement and the dots represent data points.

1. Create a tangent to the load-displacement curve based on the origin and the first data point  $(\delta_1, \Lambda_1)$ .
2. Parallel shift the tangent curve so that it crosses the x-axis at the allowable permanent deformation  $(\delta_{permanent})$ .
3. The capacity  $(\Lambda_{capacity})$  is found from the intersection of the two curves.

Figure 6.16 were made for all nonlinear analyses and can be found in the electronic attachments, see Appendix D. An excel macro was used to extract the exact location of the intersections so that the capacities could be determined.

Capacity curves similar to the ones presented for the linear analyses (Section 6.1) can be found in Figure 6.17, and capacities for both BCs are presented. The obtained capacities can also be found in Table 8 and 9 in Appendix C.2. The residual capacity for each load case is illustrated in Figure 6.18, being in the range of 50 % to 260 % of the linear capacity.

The "half model" was primarily used with the "party fixed" BCs. A single analysis of the "half model" with the "all fixed" BCs was done to verify that the results are comparable to the results obtained using the "whole model". The influence of the BCs is assumed to be greater the wider the load is as explained previously, so the W4H0-load (Figure 6.1e) was used for this purpose to be on the conservative side. The "half model" was slightly stiffer, but the difference was negligible. For allowable permanent deformation at midspan of 0.5 % and 1.0 % of the stiffener length, the increase in capacity was 2.2 % and 3.4 %, respectively.

### 6.3 Rule Design Loads

The rule design loads were calculated for comparison purposes. Procedure and equations are as presented in Section 3, while relevant input parameters for the ship used in the calculations can be found in Table 3 (Section 5.3). A script was utilized for the calculations (Appendix A.6). The design loads are presented in Figure 6.19, along

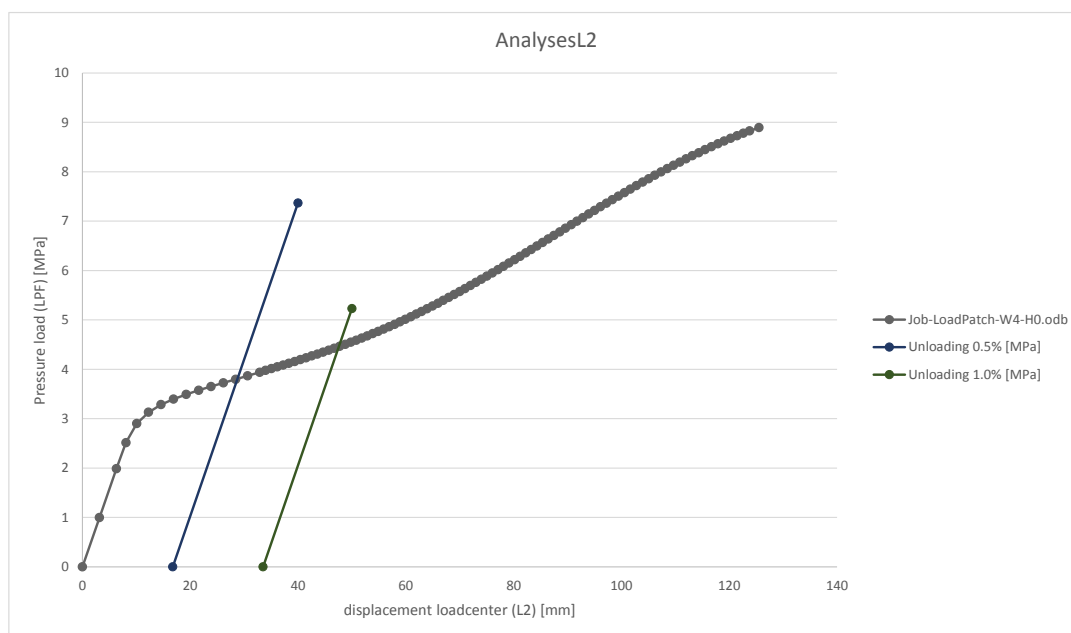
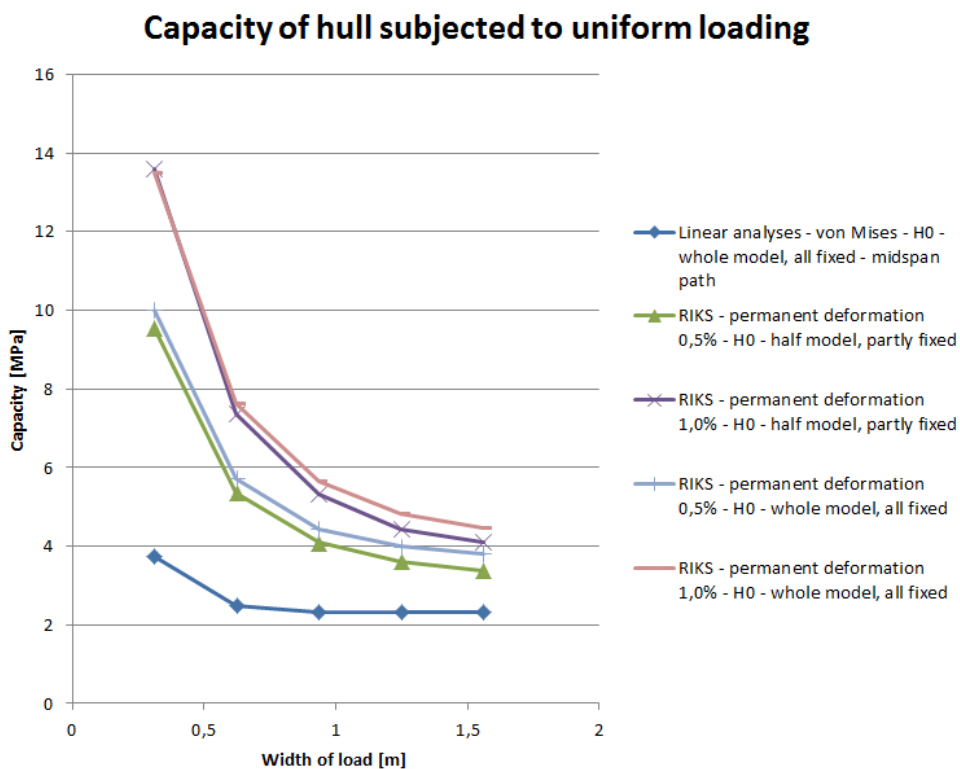
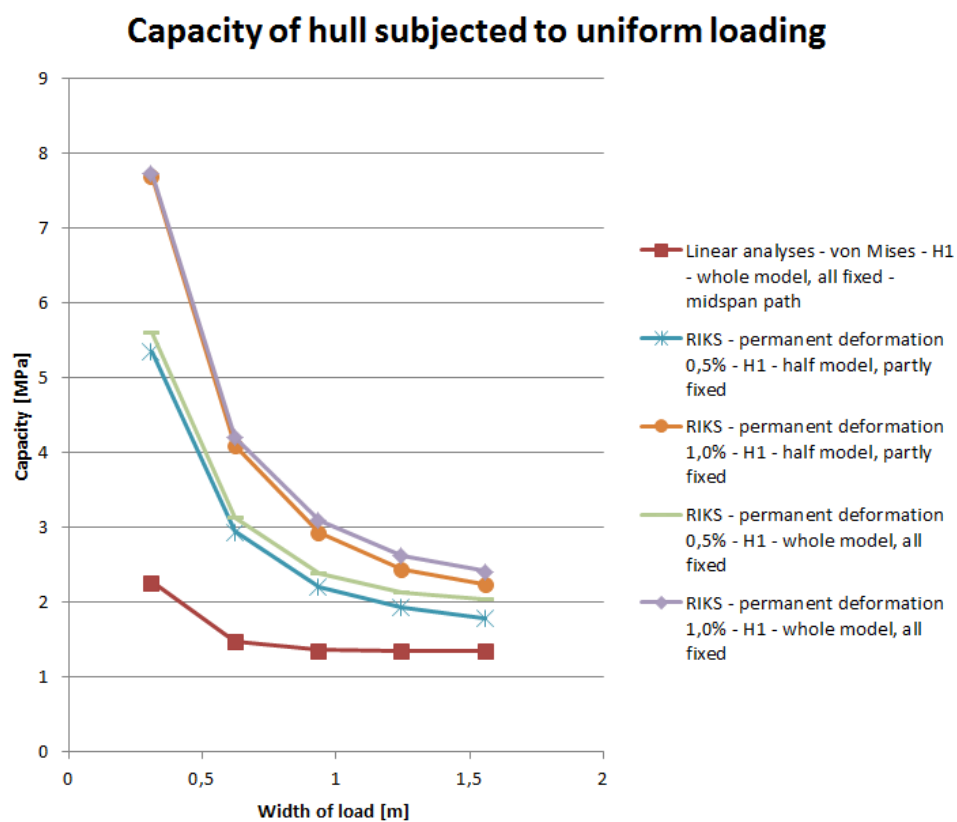


Figure 6.16: Example of "unloading-curves" along with load-displacement curve used for obtaining capacities.

with the capacity curves for load height  $H_0$ . Note that the class notations use an ice height ( $h$ ) of 0.35 m which is a little less than the ones used for the FE analyses ( $H_0 = 409$  cm in global z-direction).



(a) Load patch height H0.



(b) Load patch height H1.

Figure 6.17: Ultimate and linear capacity a function of load patch width.

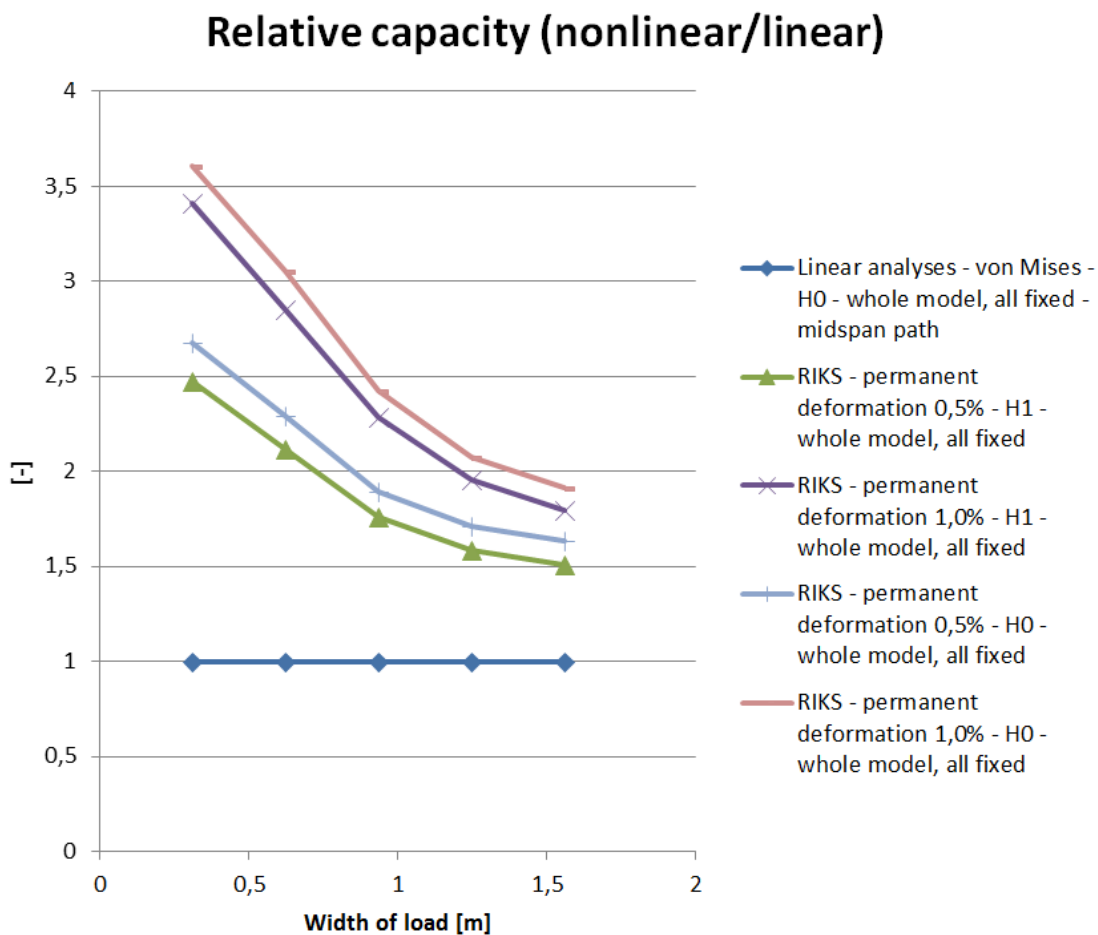


Figure 6.18: Illustration of residual strength, taken as the nonlinear capacity divided by the linear capacity.

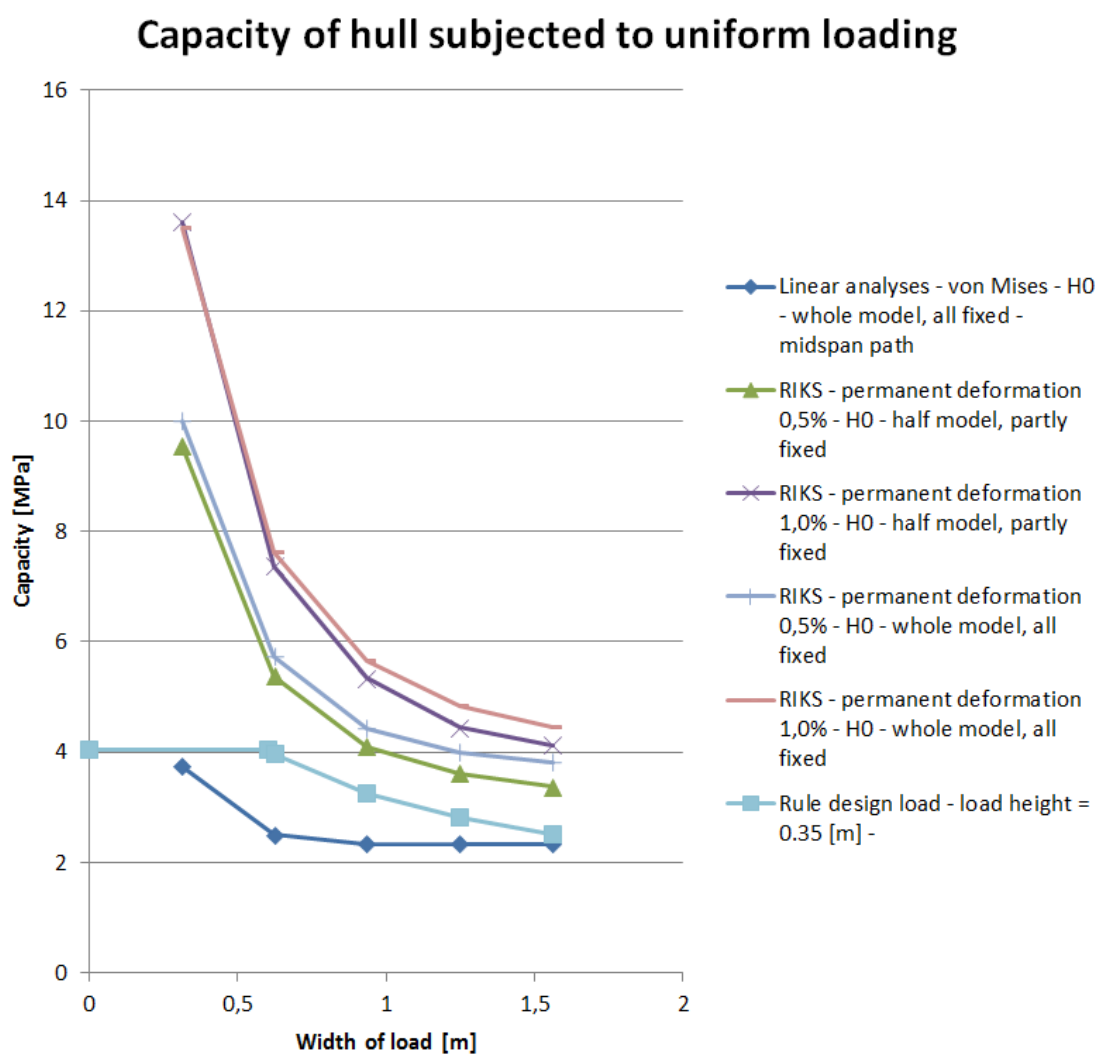


Figure 6.19: Ultimate capacity, linear capacity and rule design load as a function of load patch width.



## 7 Discussions

In this section the approach, assumptions and results presented will be discussed.

### 7.1 Finite Element Model

The FE model assessed in this thesis is located on the outskirts of the bow region of the ship. One would expect that the most severe loads will be experienced in the very front of the bow, but there are reasons why that might not be the case. The class notations for the Baltic ice classes specifies that assistance from ice breakers is expected, meaning that vessels will mainly interact with ice at the edges of the open channel. Hull inclination will also be larger at the very front, apart from at the bulbous bow, which in general tend to reduce the loads due more to initiation of bending failure modes. It can therefore be assumed that the most severe loading will occur on the sides of the bow region. Design requirements are in any case the same for the whole bow region (*DNV GL rules for classification: Ships (RU-SHIP)*, 2016).

From the mesh convergence study it came clear that reasonable results (maximum stresses and displacements) were obtained if ten or more elements were used over the web height, and fewer elements were needed for the smaller loads in the linear range. 21 elements were still used, so it may be argued that a somewhat coarser mesh would have been sufficient, especially for the linear analyses. The main reason for having such a fine mesh was to acquire a better resolution when plotting stress distributions over the cross section of the stiffeners. Smooth and detailed curves were in this way obtained and the simple numerical integration of the shear stress over the web cross section became more accurate. The use of **S4R** elements can be justified by the results from the mesh convergence study: It was seen that the performance of **S4R** was somewhat better than that of **S4** elements, and **S4R** is at the same time less computationally costly. Higher order elements were not checked for convergence, as reducing element size is in general more efficient than increasing element order. Hourglassing tendencies was not observed from visual inspection of the mesh. It was not expected either since loads and BCs were distributed over many nodes and the default hourglassing control in Abaqus was used, so hourglassing was assumed to not be a problem. It was also seen from visual inspection of the model that the mesh looks fine in most regions. A limited number of elements are distorted in certain areas (Appendix B), but these elements were not critically loaded or deformed, so it was concluded that this will not be a problem.

Two boundary conditions were evaluated and they are only slightly different: For "all fixed" there is more moment bearing capacity at the outer edges of the model, whereas "partly fixed" is more conservative since moments will be somewhat "moved" to the center where the loads are applied. From Figure 6.17 it was seen that the difference in capacity for the two BCs was limited, but was in general larger when the load patch was wider. This is because the rotational constraints in the hull skin will be more influential when loads are applied close the boundaries of the model. It was not feasible to make more realistic BCs, for instance by expanding

the model with more bulkheads and decks. This would at the same time have made the computations more costly. The analyses were already quite computationally expensive, and together with the fact that extending the model would have been time consuming itself, this option was discarded. As long as load levels are such that stresses and strains along the boundaries are small, the BCs used are assumed to be a reasonable representation of the surrounding structure, as discussed in Section 6. Any of the two will give good indications of the capacities, but "partly fixed" is slightly more conservative.

Another reason for introducing the "partly fixed" BCs was to see how the shear load will distribute to the bottom deck through the lug plates. It turned out that the stress level in the lug plates (along with the rest of the deck) was small compared to the stress levels in other regions. The stiffener ends were constrained in the z-direction so a part of the shear load was admittedly carried by the BCs (due to the inclined ship side), but it is assumed that lug-plates would not be critically loaded in any case.

The "half model" was introduced to save storage space. It was necessary to verify that the two models actually are comparable for the load cases looked into. The comparison of the "half model" and "whole model", with both using "all fixed" BCs, showed that the capacities differed only 2-3 % in a load case which was assumed to be conservative. The use of the "half model" can therefore be justified, and the results obtained with the different models are therefore comparable. This can also be used as argument for saying that increasing the overall model size will not have a great impact on the calculated capacities: It is unlikely that expanding the "whole model" will change the response significantly when reducing the size has little influence.

A challenge with NLFEA is that a failure criterion have to be defined, in contrast to the case of linear analyses where first yield in most cases can be taken as the failure criterion. The material model used in the NLFEA has no failure criterion implemented so infinite strains can in theory be sustained, while tearing and fracturing would occur in reality for excessive straining. The criterion that was made (Section 6.2.2) gives a conservative estimate of the hull strength, as discussed. Since the vessel assessed is considered for operation on more severe ice conditions than it was initially designed for, the ultimate capacity obtained using the criterion will thus not be the true ultimate capacity, but is rather an estimate of a maximum acceptable load level. The equivalent plastic strains were well below minimum requirements for the material using this criterion and the magnitude of the allowable deformations are in line with what engineers at DNV GL with and research say is acceptable. For operation in extreme cold the steel temperature above the waterline may sink below freezing, reducing the ductility of the steel. As the utilized strain level is less than a third of the minimum required material capacity it is assumed that the failure criterion in any case will be on the safe side.

A material model with slightly steeper hardening could have been used, giving a ultimate stress closer to the material minimum requirement on ultimate tensile strength of 490 MPa (see Section 5.3). This was not done, however, because DNV GL supervisors recommended using the model described in Section 5.3. Since plastic strain levels were small for the loads assessed, it can also be argued that implementing an-



other hardening rule would be of minor significance. Taking into account that both the material model used is softer than the minimum material requirements (in the plastic regime) and that the strain levels were relatively modest, it is safe to assume that the ultimate capacity criterion used is on the conservative side.

## 7.2 Loads

Since the model is located in the waterline area, it is assumed that stresses from hydrostatic pressure will be negligible compared to the loads applied. The same is assumed for bodyforces due to gravity. Furthermore, the model is located in the neutral axis of the ship<sup>14</sup> so stresses due to global bending of the hull girder will be small, which is also assumed to hold true for stresses due to global shear forces<sup>15</sup>. The assumption of zero prestresses in the model is therefore justifiable.

The ice loading applied on the structure is, however, more questionable. In Section 2.1 an in-depth discussion on ice loading was presented. Ice loading on ship hull is in general highly nonuniform. High pressure zones experience pressures many times larger than the surrounding regions, while some regions of the nominal contact area will not come in contact with the ice at all. This is to some extent taken into account by the rule loads, since a load patch height of 0.35 m is used which is smaller than the assumed ice height of 1.0 m. Erceg et al. (2014) showed that damages on a stiffened panel are more severe when using a realistic nonuniform pressure distribution than when using uniformly distributed pressures according to polar rules (FSICR/IACS). Moreover, the load distribution changes significantly during impact as parts of the ice crush and spall off. It has been shown that this time-varying load distribution has an influence on the response (Quinton et al., 2012).

The big issue when modeling ice loading is that the deformation processes in ice are so complex and chaotic of nature, making it almost impossible to model in an exact manner. As discussed in Section 4, the numerical methods developed for representing ice all have their shortcomings and none has yet been verified. The material models have problems reproducing the nonuniform pressure distributions seen from experiments, in particular. An alternative to using FE models for ice for applying loads is to simply paint measured pressure distributions on the structure. It was pointed out in Section 4 that it may be easier to overcome difficulties with this method of applying loads, than to overcome the problems of making a material model.

However, these methods were not investigated or utilized in this thesis, due to time limitations. Uniform pressure patches were used instead. This is a simplified way of applying ice loading, where it is assumed that the pressure distribution of ice is smeared out uniformly on a pressure patch. Ideally, other load distributions should have been assessed as well since it is expected that nonuniform load distributions will yield larger damages. An advantage of using uniform load distributions, apart from being simple to apply, is that comparing capacities will be comparable with the uniform rule design loads. It can also be noted that there will be a frictional

<sup>14</sup>Information provided by DNV GL supervisors.

<sup>15</sup>Information provided by DNV GL supervisors.

component of the ice loading on the hull side because of forward motion of the vessel. This was not taken into account in the calculations, because the frictional forces are assumed to be of minor importance.

### 7.3 Solution Scheme and Procedure

Ice loading on a ship hull will in general be distributed over an area and the loaded surface will deform differently at different locations. The use of displacement control in the FE analyses is therefore problematic, so load control was used. Tendencies of tripping of the stiffeners were observed from the linear analyses. Since tripping can result in loss of stiffness, the arc length method **RIKS** was used for the nonlinear analyses. However, it was seen in retrospect that using a load incremental procedure with Newton-Raphson iterations (**Static**, **General**) would have been sufficient. The load levels looked into in this thesis were reached before limit points were reached and nonlinearities were smooth and plasticity-based. Computer power and time would have been saved if the more efficient Newton-Raphson method was used, but results would of course still have been the same. Some of the load cases looked into did indeed show softening (Figure 6.10), and for these cases **Static**, **General** with load control<sup>16</sup> would not have been able to capture the response following the limit points. An alternative measure for reducing computational cost would have been to reduce the maximum number of increments for each analysis. With some experience of how the problems behaved, a more reasonable number of increments could have been determined. It was on the other hand interesting to observe that tripping actually occurred, even though the results for large displacement are less trustworthy because of large strains.

A quasi-static approach was chosen because the influence of dynamic effects was assumed to be small, in line with the requirements listed in Section 5.1: There is no repeated loading. Steels tend to have a rather modest strain rate hardening, so viscous material behavior was not modelled. Also, a stiffened panel is a relatively lightweight structure, so the mass forces will be small compared to the ice loads. If, however, an ice feature were to be numerically modelled, it would have been important to implement the profound strain rate dependencies of ice discussed in Section 2. Furthermore, discontinuous nonlinear behavior would have been expected due to fracturing and cracking of ice, making an explicit dynamic analysis a better choice.

### 7.4 Results

The linear analyses showed that the most critical loading location was loads centered at the central stiffener (L2). This was expected since the support from surrounding structure is smaller farther away. The highest stresses were experienced at the midspan of this stiffener and the bending component dominated. Shear stresses were largest at the lower ends of the stiffeners, due to the more rigid support. This can

---

<sup>16</sup>General static with stabilization would have been able to simulate softening, but stabilization was not considered in this thesis.

be confirmed by looking at Figure 6.9 where it is seen that plastic hinges have been formed at the midspan and at the lower end, but not at the top. Even if loads were centered closer to the lower end, it is doubted that yielding due to shear stresses will be more critical than stresses due to bending in the current load case, because of the large difference seen between the two in Figure 6.8. Loads were for that reason located at the midspan for all analyses.

The load (pressure) capacity was significantly larger for the narrow loads compared to the wider ones (not true in terms of force). The capacity curve converges for wide loads because an increased width will only activate new stiffeners and not increase the load on stiffeners already activated. This is not the case for narrow loads, where the load is mainly carried by one stiffener which makes it sensitive to the load width. The capacities for narrow load patches is therefore high. In Figure 6.1 it is clearly visible how more stiffeners are activated when the load patch width increases.

The design loads of the vessel were calculated and they were higher than the linear capacities (Figure 6.19). It may appear as though the vessel has not fulfilled its design requirements, but this is not necessarily the case. The load cases are not directly comparable. First of all, the design height used in the class notation is fixed at 0.35 m, unlike the 0.41 m used for the height denoted  $H_0$ . Another aspect is that the widths and heights used in the FE analyses is not the actual width and height, but rather the longitudinal- and z-component of the load patch. If visualizing a "capacity surface" in the width- and height-space one would probably find that the capacities will be in line with the design loads. The most important conclusion to be taken from the rule design loads is that the values are in the same ballpark as the linear capacity, which is reassuring.

The nonlinear analyses were conducted to assess the response after yielding. The curves in Figure 6.14 were made for visualizing the load distributions for the different load cases looked into. It is seen that the loads carried by the three stiffeners become more and more equal the wider the load patch is, just as discussed above for the linear results. Note also that there is a significant difference in the total load and the load carried by the three stiffeners for the widest load patches, whereas for smaller load patches all the load is carried by the three central stiffeners as the curves for "Sum shear" and "Reaction force" are perfectly aligned. The load-displacement curves (Figure 6.12) can also be used to verify that the capacities calculated from the linear analyses (Figure 6.8) were correct, as it is seen that capacities from the linear analyses coincide with the load levels at the end of the linear regime. The same can be seen from Figure 6.14, though it is not clear to see where yielding first occurs in the stiffener.

A significant residual capacity was found for all load cases. For the criterion allowing 0.5 % of the stiffener span in permanent deformation the residual capacities ranged between 50 % and 160 % of the linear capacity, while ranging between 80 % and 260 % of the linear capacity when allowing 1.0 % of the stiffener span in permanent deformation (Figure 6.17 and 6.18). The residual strengths for narrow load patches are many times larger than those of the wide loads. A similar type of argumentation used above can explain this: For narrow loads, surrounding structural components will be activated and both their linear and plastic capacity will be "available". For

wide loads, however, the linear capacity of adjacent stiffeners have already been utilized so that only the "plastic capacity minus the linear capacity" is remaining, so to say.

Even though a profound residual strength was found for the various load cases, it is questionable whether this alone can be used as an argument for allowing the ship to operate in more severe ice conditions than it was initially designed for. As discussed in Section 3, the ice class rules take into account that larger loads than design loads will be encountered. By allowing modest permanent deformations, some of the residual capacity is therefore already utilized as it is. Damages on ice class vessels are relatively frequent and the bulk carrier that was analyzed by [Kujala and Ehlers \(2013\)](#) does actually have the same ice class and similar scantlings as the vessel looked into in this thesis. There it was found that doubling the design load would be the best in an economic point of view. It is not unlikely that a similar relation would be found for the current vessel, taking into account that class notation and scantlings are similar. Furthermore, the ice conditions described by the class notation are somewhat vague. Ice thickness of 1.0 m can mean so much in terms of loading because of the varying properties of ice. As mentioned in the introduction, it is no simple task for a vessel operator to determine the severity of the ice conditions as properties, thickness or presence of ice ridges cannot be determined easily by visual inspection, so the risk for human error is prominent. The above arguments indicate that one in general should be very careful when allowing for operation in more severe ice conditions only based on residual capacity of design loads. Note that also other factors than hull strength must also be taken into account (fatigue, propeller strength, engine power etc.), but that is outside the scope of this thesis.

## 8 Conclusions

The aim of this thesis was to investigate the hull response when subjected to ice loading. Ice as a material is very complex and difficult to model. Factors such as strain rate, hydrostatic pressure, crystal structure, salinity etc. influence material properties such as strength and failure mode. Fracturing, spalling and crushing of ice make load distributions in general highly nonuniform, and research has shown that these nonuniform loads invoke more severe damages than uniform ones. It has therefore been of interest to have a material model for ice usable for FE analyses for quite some time. As of now no such material model has been verified, since all seem to have trouble reproducing realistic pressure distributions. An alternative to using numerical FE models for ice is to directly paint known load distributions onto structures.

Ice loading was simulated in a simple manner by using uniform pressures for the analyses done in this thesis. This approach is in general unconservative, but for the purpose of comparing linear and ultimate capacity the approach is assumed to be adequate. The load capacities found from the linear analyses range between 1.3 MPa and 3.7 MPa for the different load cases (Figure 6.8).

A self-made failure criterion was made for use with the nonlinear analyses. The midspan of stiffeners are allowed to permanently deform 0.5 % or 1.0 % of the stiffener span. Strain levels in the structure were seen to be well within the material requirements. The choice of this failure criterion was not based on exact calculations, but was rather an engineering decision based on what is assumed to be acceptable permanent deformations. These deformations also coincided well with what have been mentioned by other research.

The hull exhibits additional residual capacities in the range of 50 % to 260 % of the load at first yield, according to the failure criterion used. These numbers are assumed to be conservative since the material model used is somewhat softer in the plastic regime than what is required by the rules, and because the strain levels were relatively modest. Thus, it can be concluded that the hull exhibits a profound residual strength for all load cases looked into, and that catastrophic failure will not occur the moment the load level exceeds the design loads.

It was however questioned whether this alone can justify giving a permission for operation of the ship in more severe ice conditions than it was initially designed for. From the discussion in Section 3, it comes clear that loads higher than design load are expected during winter navigation. Ice class rules assess ice loading in a very simple manner using uniform pressure patches. Only a single design point at first yield is used, while small permanent deformations are accepted at the same time. So even though a large residual capacity was found, it does not necessarily mean that it is safe to allow the vessel operate in more severe ice conditions.



## 9 Recommendations for Future Work

Full scale measurements for the upcoming winter season is already planned and it is recommended that these are done. As stated repeatedly in the thesis, ice as a material is so complex that methods available for assessing ice loads are not reliable. Doing measurements will provide necessary strain data. Experienced loads can be estimated by the use of strain gauge data, for example by taking advantage of response calculations from this thesis. Ideally, a long-term distribution can then be fit to the load data and a design load corresponding to some sort of ULS requirement can be determined, similar to what has been done by [Kujala and Ehlers \(2013\)](#). It would be interesting to compare this with the design load given by the class notations, and to see how the experienced loads compares to the nonlinear capacities. The calculated ULS-load can be compared with the nonlinear capacities from this thesis and a decision on whether the hull strength is sufficient for operation in more severe ice conditions can be made. Other factors must also be assessed (fatigue, propulsion etc.) for a general conclusion.

It would also be interesting to do response analyses with nonuniform pressure distributions in a similar manner as done by [Erceg et al. \(2014\)](#) and proposed by [Quinton et al. \(2012\)](#). One can then get an idea of how these damages compare to damages obtained using uniform pressures with equal force. It can be investigated whether a scaling factor can be determined in order to relate different response properties (stresses, strains, deformations) obtained using uniform pressures to corresponding values using more realistic ice loading pressure distributions. Such factors may be useful when assessing response to ice loading in a simplified manner using uniform load distributions.





## References

- Arakawa, M., & Maeno, N. (1997). Mechanical strength of polycrystalline ice under uniaxial compression. *Cold regions science and technology*, 26(3), 215–229.
- Belytschko, T., & Black, T. (1999). Elastic crack growth in finite elements with minimal remeshing. *International journal for numerical methods in engineering*, 45(5), 601–620.
- COMSOL. (2016). *Finite Element Mesh Refinement*. <https://www.comsol.com/multiphysics/mesh-refinement>. (accessed June 25, 2016)
- Daley, C. (1991). Ice Edge Contact-A Brittle Failure Process Model.
- Daley, C. (1994). *MSI Ice Loads Data: Compilation of Medium Scale Ice Indentation Test Results and Comparison to ASPPR*. Daley R&E.
- Daley, C., & Kim, H. (2010). Ice collision forces considering structural deformation. In *Asme 2010 29th international conference on ocean, offshore and arctic engineering* (pp. 817–825).
- Daley, C., Tuhkuri, J., & Riska, K. (1998). The role of discrete failures in local ice loads. *Cold regions science and technology*, 27(3), 197–211.
- Derradji-Aouat, A. (2000). A unified failure envelope for isotropic fresh water ice and iceberg ice.
- DNV GL rules for classification: *Ships (RU-SHIP)*. (2016). Retrieved 2016-04-11, from <https://rules.dnvgl.com/docs/pdf/DNVGL/RU-SHIP/2016-01/DNVGL-RU-SHIP-Pt6Ch6.pdf> (Part 6, Chapter 6, Section 2)
- DNV Ships / High Speed, Light Craft and Naval Surface Craft. (2011). Retrieved 2016-07-04, from <https://rules.dnvgl.com/docs/pdf/DNV/ruleship/2012-07/ts202.pdf> (Part 2, Chapter 2, Section 2)
- Erceg, B., Taylor, R., & Ehlers, S. (2015). Structural Response Comparison using different Approaches to Account for Ice Loading. In *Port and ocean engineering under arctic conditions, june 14-18, 2015 trondheim, norway*.
- Erceg, B., Taylor, R., Ehlers, S., & Leira, B. J. (2014). A Response Comparison of a Stiffened Panel Subjected to Rule-Based and Measured Ice Loads. In *Asme 2014 33rd international conference on ocean, offshore and arctic engineering* (pp. V010T07A031–V010T07A031).
- Falzon, B., & Hitchings, D. (2006). *An introduction to modelling buckling and collapse*. NAFEMS.
- Ferrari, N., Rizzuto, E., & Prestileo, A. (2015). Modelling ice characteristics in iceberg-ship collision analyses. *Towards Green Marine Technology and Transport*, 305.
- Fish, J., & Belytschko, T. (2007). *A First Course in Finite Elements*. John Wiley & Sons.
- Gagnon, R. (2007). Results of numerical simulations of growler impact tests. *Cold regions science and technology*, 49(3), 206–214.
- Gagnon, R. (2011). A numerical model of ice crushing using a foam analogue. *Cold regions science and technology*, 65(3), 335–350.
- Gold, L. W., & of Building Research, N. R. C. C. D. (1977). *Engineering properties of fresh-water ice*. National Research Council Canada, Division of Building Research.
- Gürtner, A., Konuk, I., & Løset, S. (2008). A computational cohesive element

- model for the simulation of ice drift on arrangements of ice protection piles. *Computers Struct*, 131–141.
- Gürtner, A., Bjerås, M., Kühnlein, W., Jochmann, P., & Konuk, I. (2009). Numerical simulation of ice action to a lighthouse. In *Asme 2009 28th international conference on ocean, offshore and arctic engineering* (pp. 175–183).
- Hänninen, S., Merenkulkulaitos, & Sjöfartsverket, R. (2005). *Incidents and accidents in winter navigation in the baltic sea, winter 2002-2003*. Finnish Maritime Administration. Retrieved from <https://books.google.no/books?id=FmmGAgAACAAJ>
- Hopperstad, O., & Børvik, T. (2014). *Lecture Notes Materials Mechanics Part 1*. Lecture notes for course TKT4135 Materials Mechanics.
- Høyland, K. V. (2015). *Module I Sea ice features and properties*. Lecture notes for course AT-334 Arctic Marine Measurements Techniques, Operations and Transport held at The University Centre in Svalbard (UNIS).
- ISO. (2011). ISO 19906-An international standard for arctic offshore structures. In *Proceedings of the International Conference on Port and Ocean Engineering Under Arctic Conditions*.
- ISSC. (2015). Committee v.6 arctic technology. *19th INTERNATIONAL SHIP AND OFFSHORE STRUCTURES CONGRESS*, 2(2), 799–800.
- Jordaan, I., Li, C., Sudom, D., Stuckey, P., & Ralph, F. (2005). Principles for local and global ice design using pressure-area relationships. In *Proceedings of 18th international conference on port and ocean engineering under arctic conditions* (Vol. 1, pp. 375–386).
- Jordaan, I. J. (2001). Mechanics of ice–structure interaction. *Engineering Fracture Mechanics*, 68(17), 1923–1960.
- Kierkegaard, H. (1993). *Ship collisions with icebergs*. Danmarks Tekniske Højskole, Instituttet for Skibs-og Havteknik.
- Kim, E., & Amdahl, J. (2016). Discussion of assumptions behind rule-based ice loads due to crushing. *Ocean Engineering*, 119, 249–261.
- Konuk, I., Gürtner, A., & Yu, S. (2009). A Cohesive Element Framework for Dynamic Ice-Structure Interaction Problems—Part I: Review and Formulation. In *Asme 2009 28th international conference on ocean, offshore and arctic engineering* (pp. 33–41).
- Kujala, P., & Ehlers, S. (2013). Limit State Identification for Ice-Strengthened Hull Structures Using Measured Long-Term Loads. In *Proceedings of the International Conference on Port and Ocean Engineering Under Arctic Conditions*.
- Kwak, M.-J., Choi, J.-H., Park, J.-H., & Woo, J.-H. (2009). Strength assessment for bow structure of arctic tanker (107k) under ship-ice interaction. In *International conference on ship and offshore technology: Ice class vessels* (pp. 28–29).
- Langleben, M., & Pounder, E. (1961). *Elastic parameters of sea ice* (Tech. Rep.). DTIC Document.
- Liu, Z., Amdahl, J., & Løset, S. (2011). Plasticity based material modelling of ice and its application to ship–iceberg impacts. *Cold regions science and technology*, 65(3), 326–334.
- Løset, S. (1993). Thermal energy conservation in icebergs and tracking by temperature. *Journal of Geophysical Research: Oceans* (1978–2012), 98(C6), 10001–

- 10012.
- Love, A. E. H. (2013). *A Treatise on The Mathematical Theory of Elasticity* (Vol. 1). Cambridge University Press.
- MANICE. (2005). Manual of standard procedures for observing and reporting ice conditions. revised ninth edition.
- Marchenko, N. (2014). Floating Ice Induced Ship Casualties. In *The 22nd iahr international symposium on ice* (pp. 908–915).
- Mathiesen, K. M. (2014). *Lecture notes*. Lecture notes for course TMR4190 Finite Element Method in Structural Analysis.
- Mathiesen, K. M. (2015). *Lecture notes*. Lecture notes for course TKT4197 Nonlinear Finite Element Analyses.
- Memon, B.-A., & Su, X.-z. (2004). Arc-length technique for nonlinear finite element analysis. *JOURNAL-ZHEJIANG UNIVERSITY SCIENCE*, 5(5), 618–628.
- Mork, H. (2015, December). *Properties of ice, physics of ship-iceberg impact and available analyses methods* [Unpublished]. Project thesis, The Norwegian University of Science and Technology. (Written and supervised at Hamburg University of Technology)
- NAFEMS. (2016a). *The Importance of Mesh Convergence - 1*. <https://www.nafems.org/join/resources/knowledgebase/001/>. (accessed June 26, 2016)
- NAFEMS. (2016b). *The Importance of Mesh Convergence - 2*. <https://www.nafems.org/join/resources/knowledgebase/002/>. (accessed June 26, 2016)
- NORSOK. (2004a). Standard N-001. *Structural Design, Rev, 2*.
- NORSOK. (2004b). Standard N-004. *Structural Design, Rev, 4*.
- Nyseth, H. (n.d.). personal communication, 2016-05-13. (external supervisor at DNV GL)
- Quinton, B. W., Daley, C. G., Gagnon, R. E., et al. (2012). Realistic moving ice loads and ship structural response. In *The twenty-second international offshore and polar engineering conference*.
- Riska, K. (1995). Models of ice-structure contact for engineering applications. *Studies in Applied Mechanics*, 42, 77–103.
- Riska, K., & Frederking, R. M. W. (1987). *Ice load penetration modelling* (Vol. 1).
- Riska, K., & Kämäräinen, J. (2011). A Review of Ice Loading and the Evolution of the Finnish-Swedish Ice Class Rules. In *Proceedings of the SNAME Annual Meeting and Expo. November* (pp. 16–18).
- Riska, K., Rantala, H., & Joensuu, A. (1990). *Full scale observations of ship-ice contact: Results from tests series onboard ib sampo, winter, 1989* (Tech. Rep.).
- Ritch, R., Frederking, R., Johnston, M., Browne, R., & Ralph, F. (2008). Local ice pressures measured on a strain gauge panel during the ccgs terry fox bergy bit impact study. *Cold Regions Science and Technology*, 52(1), 29–49.
- Sanderson, T. (1986). A pressure-area curve for ice. In *Proc of the 8th mi symposium on ice*.
- Sanderson, T. J. (1988). Ice mechanics and risks to offshore structures.
- Sawhill, S. (n.d.). personal communication, 2016-03-01. (Previously worked as chief officer (captain) at the US Coast Guards’s icebreaker Polar Sea, now employed at DNV GL)
- Schulson, E. M., & Duval, P. (2009). *Creep and Fracture of Ice*. Cambridge University

- Press Cambridge.
- Sodhi, D. S., Takeuchi, T., Nakazawa, N., Akagawa, S., & Saeki, H. (1998). Medium-scale indentation tests on sea ice at various speeds. *Cold Regions Science and Technology*, 28(3), 161–182.
- Storheim, M. (2016). Structural Response in Ship-Platform and Ship-Ice Collisions.
- Storheim, M., & Amdahl, J. (2014). Design of offshore structures against accidental ship collisions. *Marine Structures*, 37, 135–172.
- Storheim, M., Kim, E., Amdahl, J., & Ehlers, S. (2012). Iceberg shape sensitivity in ship impact assessment in view of existing material models. In *Asme 2012 31st international conference on ocean, offshore and arctic engineering* (pp. 507–517).
- Systèmes, D. (2016). *Abaqus documentation v.6.13*. <http://129.97.46.200:2080/v6.13/books/stm/default.htm?startat=ch02s03ath18.html#stm-anl-modifiedriks>. Abaqus. (accessed June 28, 2016)
- Takeuchi, T., Akagawa, S., Kawamura, M., Sakai, M., Nakazawa, N., Terashima, T., ... others (2000). Examination of factors affecting total ice load using medium scale field indentation test data. In *The tenth international offshore and polar engineering conference*.
- Timco, G., & Sudom, D. (2013). Revisiting the Sanderson pressure–area curve: Defining parameters that influence ice pressure. *Cold regions science and technology*, 95, 53–66.
- Timco, G., & Weeks, W. (2010). A review of the engineering properties of sea ice. *Cold Regions Science and Technology*, 60(2), 107–129.
- Timco, G. W., & Frederking, R. (1984). An investigation of the failure envelope of granular/discontinuous-columnar sea ice. *Cold Regions Science and Technology*, 9(1), 17–27.
- Timco, G. W., & Frederking, R. M. (1986). Confined compression tests: outlining the failure envelope of columnar sea ice. *Cold Regions Science and Technology*, 12(1), 13–28.
- Timoshenko, S. (1934). *Theory of Elasticity. 1st*. McGraw-Hill Book Company, Inc.; New York.
- Tuhkuri, J. (1995). Experimental observations of the brittle failure process of ice and ice-structure contact. *Cold regions science and technology*, 23(3), 265–278.
- Weeks, W. (1962). Tensile strength of nacl ice. *Journal of Glaciology*, 4, 25–52.
- Wriggers, P. (2008). *Nonlinear Finite Element Methods*. Springer Science & Business Media.

# Appendices



## A Python Scripts

All scripts presented in Appendix A are made by the author for the purpose of this thesis. Some of the variable names, for-loops etc. are, however, based on scripts made by DNV GL-colleague Ole J. Hareide. Variable names revealing the identity of the ship have been changed, so scripts may not work with the electronically attached input files.

### A.1 Create Input Files (Linear Analyses)

This script generates input files for linear analyses. For a chosen load location multiple input files with different load patch sizes will be made.

```
import shutil, os, sys, string, numpy
from abaqus import *
from abaqusConstants import *

outputFolder='AnalysesL2'

# Create output folder if it does not already exist:
outFolder=os.path.join(os.getcwd(),outputFolder)
if not os.path.exists(outFolder):
    os.mkdir(outFolder)

# Batfile for running analyses
batName = 'runme.bat'
fout = open(os.path.join(outFolder, batName), 'w')

#Location of load patch-center
CenterL54=[61.500004,-5.109043,6.016752]
CenterL24=[59.700005,-5.846021,6.015892]
CenterL34=[60.000004,-5.846021,6.015892]
CenterLB=[60.300004,-5.846021,6.015892]
Center=CenterL24

Width=312.122E-03 # initial width load patch (in x-direction) (approx)
StepW=Width/2
Height=409.228E-03 # initial height load patch (in x-direction) (approx
)
StepH=Height/2

oldJobName = mdb.jobs.items()[0][0]
for i in range(0, 5):
    #number of widths for loads
    for j in range(0,2):
        #number of heights for loads
        a = mdb.models['Model-1'].rootAssembly
        f1 = a.instances['NONAME-TweenDeckBallast-1'].surfaces['Skin']

        # create surface for loadpatch
        elements11=f1.elements.getByBoundingBox(Center[0]-(Width/2 +
        StepW*i),
        -10,Center[2]-(Height/2+StepH*j),Center[0]+(Width/2 + StepW
        *i),10,Center[2]+(Height/2+StepH*j))
```

```
a.Surface(sidelElements=elements11, name='LoadPatchTot') #
    create element surface for load

#Load (1MPa)
region = a-surfaces['LoadPatchTot']
mdb.models['Model-1'].Pressure(name='Load-LoadPatch',
    createStepName='Step-1',
    region=region, field='', magnitude=1000000.0)

# create jobs
newJobName = 'Job-LoadPatch-W%s-H%s' % (i, j)
mdb.jobs.changeKey(fromName=oldJobName, toName=newJobName)
mdb.jobs[newJobName].writeInput(consistencyChecking=OFF)
oldJobName = newJobName

# write to .bat-file
fout.write('call abaqus job=%s interactive\n' % newJobName)

#move input-files to outputfolder
currentdir=os.getcwd()
files_arr=os.listdir(currentdir)
files_arr.sort()
for file in files_arr:
    if str.endswith(file, ".inp") == 1:
        shutil.move(currentdir+"./"+file, outputFolder+"./"+
            file)
fout.close()
```



## A.2 Write Data to File (Linear Analyses)

This script determines the maximum shear-, axial- and von Mises stress over cross sections of the stiffeners, and writes them to a file.

```

from abaqus import *
from abaqusConstants import *
from abaqusExceptions import *
import os

def main():          #define function

    #region INPUT
    instanceName = r'NONAME-TweenDeckBallast-1'.upper()
    csvFileName = 'NONAME-Results.csv'
    elementLength = 0.01238
    elementThickness = 0.01
    #endregion

    outputFolder='AnalysesL2'

    # Create output folder if it does not already exist:
    outFolder=os.path.join(os.getcwd(),outputFolder)

    #region OPEN ODB
    # Find odb files in current folder
    odbNames = []
    for file in os.listdir(outFolder):
        if file.endswith('.odb'):
            odbNames.append(file)

    # If odb files were found
    if len(odbNames) != 0:
        try:
            fout = open(os.path.join(os.getcwd(), csvFileName), 'w')
        except IOError as e:
            print 'ERROR in opening ' + csvFileName + ' : ' + e.args[1]
            return

    printHeader = True
    for odbName in odbNames:
        filePath = os.path.join(outFolder, odbName)
        try:
            odb = session.odbs[filePath]
        except KeyError:
            try:
                odb = session.openOdb(filePath)
                session.viewports['Viewport: 1'].setValues(
                    displayedObject=odb)
            except OdbError:

```

```

        print 'ERROR: No odb-file with the name ' + odbName
            + ' was found in the current folder'
#endregion

#region CREATE VARIABLES
ass = odb.rootAssembly
inst = ass.instances[instanceName]
nSets = inst.nodeSets
#endregion

#region CREATE PATHS
frameNames = ['A', '1', '2', '3', 'B', 'C', '4', '5', '6',
              'D']
if len(session.paths) == 0:
    print "yes"
    session.Path(name='PATH-L2-M', type=NODE_LIST,
                 expression=(('NONAME-TWEEDECKBALLAST-1', (22994,
23000, )), )) #Path at center of L2-load
    for i in range(len(frameNames)):
        # Lower path
        myNode1 = nSets['PATHL%s-L-1' % frameNames[i]].
            nodes[0].label
        myNode2 = nSets['PATHL%s-L-2' % frameNames[i]].
            nodes[0].label
        session.Path(name='PATH-L%s-L' % frameNames[i],
                     type=NODE_LIST, expression=((instanceName, (
myNode1, myNode2, )), ))
        # Upper path
        myNode1 = nSets['PATHL%s-U-1' % frameNames[i]].
            nodes[0].label
        myNode2 = nSets['PATHL%s-U-2' % frameNames[i]].
            nodes[0].label
        session.Path(name='PATH-L%s-U' % frameNames[i],
                     type=NODE_LIST, expression=((instanceName, (
myNode1, myNode2, )), ))
#endregion

# CREATE LOCAL CSYS for every path
scratchOdb = session.ScratchOdb(odb)
scratchAss = scratchOdb.rootAssembly

for i in range(len(frameNames)):
    # Lower CSYS
    csysName = 'CSYS-L%s-L' % frameNames[i]
    originNode = nSets['XNODE-L%s-L0' % frameNames[i]].
        nodes[0]
    node1 = nSets['XNODE-L%s-L1' % frameNames[i]].nodes[0]
    node2 = nSets['XNODE-L%s-L2' % frameNames[i]].nodes[0]
    scratchAss.DatumCsysByThreeNodes (name=csysName,
                                       coordSysType=CARTESIAN,
                                       origin=
                                           originNode
                                           ,
                                           point1
                                           =
                                           node1
                                           ,

```

```

point2
=
node2
)

# Upper CSYS
csysName = 'CSYS-L%s-U' % frameNames[i]
originNode = nSets['XNODE-L%s-U0' % frameNames[i]].
nodes[0]
node1 = nSets['XNODE-L%s-U1' % frameNames[i]].nodes[0]
node2 = nSets['XNODE-L%s-U2' % frameNames[i]].nodes[0]
scratchAss.DatumCsysByThreeNodes (name=csysName,
coordSysType=CARTESIAN,
origin=
originNode
,
point1
=
node1
,
point2
=
node2
)

#CSYS for middlepoint of L2 (bending)
csysName = 'CSYS-L2-M'
originNode = inst.nodes[22993]
node1 = inst.nodes[24936]
node2 = inst.nodes[22999]
scratchOdb = session.ScratchOdb(odb)
scratchOdb.rootAssembly.DatumCsysByThreeNodes (name=csysName
, coordSysType=CARTESIAN,
origin=
originNode
,
point1
=
node1
,
point2
=
node2
)

#-----region CREATE XYOUTPUTS

#Choose S12 OR S11
#session.viewports['Viewport: 1'].odbDisplay.
setPrimaryVariable(variableLabel='S', outputPosition=
INTEGRATION_POINT, refinement=(COMPONENT, 'S12'))
session.viewports['Viewport: 1'].odbDisplay.
setPrimaryVariable(variableLabel='S', outputPosition=
INTEGRATION_POINT, refinement=(COMPONENT, 'S11'))

# Set to mid-plane section points
session.viewports['Viewport: 1'].odbDisplay.
setPrimarySectionPoint (
sectionPoint={'shell < AH-36 > < 5 section points >':(

```

```

'Mid, (fraction = 0.0)', 'SPOS, (fraction = 1.0)'), '
    shell < NV-NS > < 5 section points >': ('Mid, (
    fraction = 0.0)',
'SPOS, (fraction = 1.0)'), 'beam < rectangular > < elset
    = ASSEMBLY.NONAME-TWEENDECKBALLAST-1.BEAMS-DECK >'
    :(
'Bottom Left Corner', 'Bottom Right Corner'))})

for path in session.paths.items():
    #change to local CSYS
    dtm = scratchAss.datumCsyses['CSYS-' + path[0][-4:]]
    session.viewports['Viewport: 1'].odbDisplay.
        basicOptions.setValues(transformationType=
            USER.SPECIFIED, datumCsys=dtm)
    #create xyData #use only one of the following (S11 or
    S12):
    #xyName = 'S12-' + path[0] #
    #session.XYDataFromPath(name=xyName, path=session.paths
    [path[0]], includeIntersections=True,
    projectOntoMesh=False,
    # pathStyle=UNIFORM_SPACING, numIntervals=18,
    projectionTolerance=0, shape=UNDEFORMED, labelType=
    TRUE.DISTANCE)
    xyName = 'S11-' + path[0] #
    session.XYDataFromPath(name=xyName, path=session.paths[
    path[0]], includeIntersections=True, projectOntoMesh
    =False,
    pathStyle=UNIFORM_SPACING, numIntervals=18,
    projectionTolerance=0, shape=UNDEFORMED,
    labelType=TRUE.DISTANCE)
#endregion

#region WRITE TO CSV FILE
xyoutputs = session.xyDataObjects
# print header
if printHeader:
    for xyout in xyoutputs.items():
        name = xyout[0][-4:]
        fout.write(', ' + name)
    fout.write('\n')
    printHeader = False

fout.write(odbName)
while len(xyoutputs) > 0:
    xyout = xyoutputs.items()[0]
    data = xyout[1]
    #extract largest stress over path
    stressMax=abs(data[0][1])
    for i in range(len(data)):
        if abs(data[i][1]) > stressMax:
            stressMax=abs(data[i][1])

    fout.write(', ' + str(stressMax))
    del xyoutputs[xyout[0]]
odb.close()
fout.write('\n')

```

```
        #endregion
        fout.close()
# If no odb files were found
else:
    print "No ODB-files found in the specified folder"

main()          #run function
```

### A.3 Create Input Files (Nonlinear Analyses)

This script generates input files for nonlinear analyses. For a chosen load location multiple input files with different load patch sizes will be made.

```
import shutil, os, sys, string, numpy
from abaqus import *
from abaqusConstants import *

outputFolder='AnalysesL3'

# Create output folder if it does not already exist:
outFolder=os.path.join(os.getcwd(),outputFolder)
if not os.path.exists(outFolder):
    os.mkdir(outFolder)

# Batfile for running analyses
batName = 'runme.bat'
fout = open(os.path.join(outFolder, batName), 'w')

#Surface for loading
CenterL54=[61.500004,-5.109043,6.016752]
CenterL24=[59.700005,-5.846021,6.015892]
CenterL34=[60.000004,-5.846021,6.015892]
CenterLB=[60.300004,-5.846021,6.015892]
Center=CenterL34

Width=312.122E-03 # initial width load patch (in x-direction) (approx)
StepW=Width/2
Height=409.228E-03 # initial height load patch (in x-direction) (approx
)
StepH=Height/2

oldJobName = mdb.jobs.items()[0][0]
for i in range(0, 5): #number of widths for loads
    for j in range(0,2): #number of heights for loads
        a = mdb.models['Model-1'].rootAssembly
        f1 = a.instances['NONAME-TweenDeckBallast-1'].surfaces['Skin']

        # create surface for loadpatch
        elements11=f1.elements.getByBoundingBox(Center[0]-(Width/2 +
            StepW*i),
            -10,Center[2]-(Height/2+StepH*j),Center[0]+(Width/2 + StepW
                *i),10,Center[2]+(Height/2+StepH*j))
        a.Surface(sidelElements=elements11, name='LoadPatchTot') #
            create element surface for load
        a = mdb.models['Model-1'].rootAssembly

        #Load (1MPa)
        region = a.surfaces['LoadPatchTot']
        mdb.models['Model-1'].Pressure(name='Load-LoadPatch',
            createStepName='Step-2_staRIKS',
            region=region, field='', magnitude=1000000.0)

    # create jobs
```

```
newJobName = 'Job-LoadPatch-W%s-H%s' % (i, j)
mdb.jobs.changeKey(fromName=oldJobName, toName=newJobName)
mdb.jobs[newJobName].writeInput(consistencyChecking=OFF)
oldJobName = newJobName

# write to .bat-file
fout.write('call abaqus job=%s interactive\n' % newJobName)

#move input-files to outputfolder
currentdir=os.getcwd()
files_arr=os.listdir(currentdir)
files_arr.sort()
for file in files_arr:
    if str.endswith(file, ".inp") == 1:
        shutil.move(currentdir+"./"+file, outputFolder+"./"+
                    file)
fout.close()
```

## A.4 Write Load-Displacement Data to File (Nonlinear Analyses)

This script extracts LPF (pressure) and lateral displacement at the center of the load and writes them to a file.

```
from abaqus import *
from abaqusConstants import *
from abaqusExceptions import *
import os

#region INPUT
instanceName = r'NONAME-TweenDeckBallast-1'.upper()
csvFileName = 'NONAME-Results-LPF_delta.csv'
#elementLength = 0.01238
#elementThickness = 0.01
L2span=3.35 #[m]

#outputFolder='AnalysesL2'
outputFolder='AnalysesL3'

# Create output folder if it does not already exist:
outFolder=os.path.join(os.getcwd(),outputFolder)

# Find odb files in current folder
odbNames = []
for file in os.listdir(outFolder):
    if file.endswith('.odb'):
        odbNames.append(file)

# If odb files were found
if len(odbNames) != 0:
    try:
        fout = open(os.path.join(os.getcwd(), csvFileName), 'w')
        fout.write(outputFolder + '\n' + ',stiffenerspan [mm],allowed
            permanent deformation1[-]'
            +',allowed permanent deformation1[mm]'
            +',allowed permanent deformation2[-]'
            +',allowed permanent deformation2[mm]'
            + '\n' + ',' + str(L2span*1000) + ',0.01,'+str(L2span
                *1000*0.01)+
            ',0.005,' + str(L2span*1000*0.005) + '\n \n \n \n')
    except IOError as e:
        print 'ERROR in opening ' + csvFileName + ' : ' + e.args[1]
        #return

printHeader = True
for odbName in odbNames:
    filePath = os.path.join(outFolder, odbName)
    try:
        odb = session.odbs[filePath]
    except KeyError:
        try:
            odb = session.openOdb(filePath)
```



```

        session.viewports['Viewport: 1'].setValues(
            displayedObject=odb)
    except OdbError:
        print 'ERROR: No odb-file with the name ' + odbName + '
            was found in the current folder'
#endregion

#region CREATE VARIABLES
ass = odb.rootAssembly
inst = ass.instances[instanceName]
nSets = inst.nodeSets

#-----create local CSYS (fixed at center of load)
-----

if outputFolder == 'AnalysesL2':
    scratchOdb = session.ScratchOdb(odb)
    CSYSname='CSYS-L2-plate-fixed'
    scratchOdb.rootAssembly.DatumCsysByThreePoints(name=
        CSYSname,
        coordSysType=CARTESIAN, origin=(59.7000045776367,
            -5.85721302032471,
            6.03801012039185), point1=(59.6012954711914,
            -5.88619947433472,
            6.02173376083374), point2=(59.7000045776367,
            -5.90748834609985,
            6.13758754730225))

elif outputFolder == 'AnalysesL3':
    scratchOdb = session.ScratchOdb(odb)
    CSYSname='CSYS-L3-plate-fixed'
    scratchOdb.rootAssembly.DatumCsysByThreePoints(name=
        CSYSname,
        coordSysType=CARTESIAN, origin=(60.0000038146973,
            -5.73804092407227,
            6.03168249130249), point1=(59.8423728942871,
            -5.78571701049805,
            6.00562000274658), point2=(60.0000038146973,
            -5.81309080123901,
            6.17571496963501))

#-----change to local fixed coord
scratchAss = scratchOdb.rootAssembly
dtm = scratchAss.datumCsyses[CSYSname]
session.viewports['Viewport: 1'].odbDisplay.basicOptions.
    setValues(
        transformationType=USER_SPECIFIED, datumCsys=dtm,
        transformOnDeformed=False)

#----- create xy data
#delete old xydata:
for i in range(len(session.xyDataObjects.items())):
    xydataname=session.xyDataObjects.items()[0][0] #delete
        first in list for each loop
    del session.xyDataObjects[xydataname]

```

```
#displacement at center of load
if outputFolder == 'AnalysesL2':
    session.xyDataListFromField(odb=odb, outputPosition=NODAL,
        variable=('U',
            NODAL, ((COMPONENT, 'U3'), )), ), nodeLabels=((
                'NONAME-TWEENDECKBALLAST-1', ('22994', )), ))
    session.xyDataObjects.changeKey(
        fromName='U:U3 (UNDEF:CSYS-L2-plate-fixed) PI: NONAME-
            TWEENDECKBALLAST-1 N: 22994',
        toName="deltaL2")
elif outputFolder == 'AnalysesL3':
    session.xyDataListFromField(odb=odb, outputPosition=NODAL,
        variable=('U',
            NODAL, ((COMPONENT, 'U3'), )), ), nodeLabels=((
                'NONAME-TWEENDECKBALLAST-1', ('30817', )), ))
    session.xyDataObjects.changeKey(
        fromName='U:U3 (UNDEF:CSYS-L3-plate-fixed) PI: NONAME-
            TWEENDECKBALLAST-1 N: 30817',
        toName="deltaL3")

#LPF for whole model
session.XYDataFromHistory(name='LPF', odb=odb,
    outputVariableName='Load proportionality factor: LPF for
        Whole Model',
    steps=('Step-2_starIKS', ), )

#----- write to CSV-file
fout.write(odbName + ',' + '\n')
num_inc=len(session.xyDataObjects['LPF'])

if outputFolder == 'AnalysesL2':
    fout.write('displacement loadcenter (L2) [mm]' + ',')
    for i in range(num_inc):
        fout.write(str(session.xyDataObjects['deltaL2'][i
            ][1]*1000) + ',')
    fout.write('\n')
elif outputFolder == 'AnalysesL3':
    fout.write('displacement loadcenter (L3) [mm]' + ',')
    for i in range(num_inc):
        fout.write(str(session.xyDataObjects['deltaL3'][i
            ][1]*1000) + ',')
    fout.write('\n')
fout.write('Pressure load (LPF) [MPa]' + ',')
for i in range(num_inc):
    fout.write(str(session.xyDataObjects['LPF'][i][1]) + ',')

#get space between data sets:
fout.write('\n')
fout.write('\n')
fout.write('\n \n \n \n \n \n') #to fit new layout
odb.close()

fout.close()
```

```
# If no odb files were found
else:
    print "No ODB-files found in the specified folder"
```

## A.5 Write Detailed Load-Displacement and Shear Data to File (Nonlinear Analyses)

This script extracts data from the result files where the load patch is centered at the L2 stiffener. LPF (pressure), lateral displacement at the center of the load, total reaction force, shear forces in stiffeners (L1, L2 and L3) and the sum of these are written to a file.

```
from abaqus import *
from abaqusConstants import *
from abaqusExceptions import *
import os
import displayGroupOdbToolset as dgo

#region INPUT
instanceName = r'NONAME-TweenDeckBallast-1'.upper()
csvFileName = 'NONAME-Results-LPF_delta_shear.csv'
elementLength = 0.01238
elementThickness = 0.01 #stiffener web

L2span=3.35 #[m]

outputFolder='AnalysesL2'

# Create output folder if it does not already exist:
outFolder=os.path.join(os.getcwd(),outputFolder)

#region OPEN ODB
# Find odb files in current folder
odbNames = []
for file in os.listdir(outFolder):
    if file.endswith('.odb'):
        odbNames.append(file)
# If odb files were found
if len(odbNames) != 0:
    try:
        fout = open(os.path.join(os.getcwd(), csvFileName), 'w')
        # write relevant info on top:
        fout.write(outputFolder + '\n' + ',stiffenerspan [mm],allowed
        permanent deformation1[-]'
        +',allowed permanent deformation1[mm]'
        +',allowed permanent deformation2[-]'
        +',allowed permanent deformation2[mm]'
        + '\n' + ',' + str(L2span*1000) + ',0.01,'+str(L2span
        *1000*0.01)+
        ',0.005,' + str(L2span*1000*0.005) + '\n \n \n \n')
    except IOError as e:
        print 'ERROR in opening ' + csvFileName + ' : ' + e.args[1]
        #return

printHeader = True
for odbName in odbNames:
    filePath = os.path.join(outFolder, odbName)
    try:
        odb = session.odbs[filePath]
```

```

except KeyError:
    try:
        odb = session.openOdb(filePath)
        session.viewports['Viewport: 1'].setValues(
            displayedObject=odb)
    except OdbError:
        print 'ERROR: No odb-file with the name ' + odbName + '
              was found in the current folder'
#endregion

#region CREATE VARIABLES
ass = odb.rootAssembly
inst = ass.instances[instanceName]
nSets = inst.nodeSets

#-----create local CSYS (fixed at center of load) -----
scratchOdb = session.ScratchOdb(odb)
scratchOdb.rootAssembly.DatumCsysByThreePoints(name='CSYS-L2-
plate-fixed',
        coordSysType=CARTESIAN, origin=(59.7000045776367,
            -5.85721302032471,
            6.03801012039185), point1=(59.6012954711914,
            -5.88619947433472,
            6.02173376083374), point2=(59.7000045776367,
            -5.90748834609985,
            6.13758754730225))

#-----change to local fixed coord
scratchOdb = session.ScratchOdb(odb)
scratchAss = scratchOdb.rootAssembly
CSYSname='CSYS-L2-plate-fixed'
dtm = scratchAss.datumCsyses[CSYSname]
session.viewports['Viewport: 1'].odbDisplay.basicOptions.
    setValues(
        transformationType=USER_SPECIFIED, datumCsys=dtm,
        transformOnDeformed=False)

#----- create xy data, displacement + LPF
#delete old xydata
for i in range(len(session.xyDataObjects.items())):
    xydataname=session.xyDataObjects.items()[0][0] #delete
        first in list for each loop
    del session.xyDataObjects[xydataname]

#displacement at center of load
session.xyDataListFromField(odb=odb, outputPosition=NODAL,
    variable= (('U',
        NODAL, ((COMPONENT, 'U3'), ), ), ), nodeLabels=((
        'NONAME-TWEENDECKBALLAST-1', ('22994', ), ))
session.xyDataObjects.changeKey(
    fromName='U:U3 (UNDEF:CSYS-L2-plate-fixed) PI: NONAME-
        TWEENDECKBALLAST-1 N: 22994',
    toName="deltaL2")

#LPF for whole model
session.XYDataFromHistory(name='LPF', odb=odb,

```

```

outputVariableName='Load proportionality factor: LPF for
  Whole Model',
steps=('Step-2_staRIKS', ), )

#----- region: extract shear in stiffeners
-----
#-----CREATE PATHS-----
frameNames = ['1', '2', '3'] #only for three central stiffeners
if len(session.paths) == 0:
    print "yes"
    #( remember to create CSYS for every path)
    for i in range(len(frameNames)):
        # Lower path
        myNode1 = nSets['PATHL%s-L-1' % frameNames[i]].nodes
            [0].label
        myNode2 = nSets['PATHL%s-L-2' % frameNames[i]].nodes
            [0].label
        session.Path(name='PATH-L%s-L' % frameNames[i], type=
            NODE.LIST, expression=((instanceName, (myNode1,
            myNode2, )), ))
        # Upper path
        myNode1 = nSets['PATHL%s-U-1' % frameNames[i]].nodes
            [0].label
        myNode2 = nSets['PATHL%s-U-2' % frameNames[i]].nodes
            [0].label
        session.Path(name='PATH-L%s-U' % frameNames[i], type=
            NODE.LIST, expression=((instanceName, (myNode1,
            myNode2, )), ))

#----- CREATE LOCAL CSYS-----
scratchOdb = session.ScratchOdb(odb)
scratchAss = scratchOdb.rootAssembly
for i in range(len(frameNames)):
    # Lower CSYS
    csysName = 'CSYS-L%s-L' % frameNames[i]
    originNode = nSets['XNODE-L%s-L0' % frameNames[i]].nodes[0]
    node1 = nSets['XNODE-L%s-L1' % frameNames[i]].nodes[0]
    node2 = nSets['XNODE-L%s-L2' % frameNames[i]].nodes[0]
    scratchAss.DatumCsysByThreeNodes (name=csysName,
        coordSysType=CARTESIAN,
        origin=
            originNode
            , point1=
            node1,
            point2=
            node2)

    # Upper CSYS
    csysName = 'CSYS-L%s-U' % frameNames[i]
    originNode = nSets['XNODE-L%s-U0' % frameNames[i]].nodes[0]
    node1 = nSets['XNODE-L%s-U1' % frameNames[i]].nodes[0]
    node2 = nSets['XNODE-L%s-U2' % frameNames[i]].nodes[0]
    scratchAss.DatumCsysByThreeNodes (name=csysName,
        coordSysType=CARTESIAN,
        origin=
            originNode
            , point1=

```

```

node1,
point2=
node2)

#----- CREATE XYOUTPUTS-----

#Choose S12
session.viewports['Viewport: 1'].odbDisplay.setPrimaryVariable(
    variableLabel='S', outputPosition=INTEGRATION_POINT,
    refinement=(COMPONENT, 'S12'))

#Set to mid-plane section points
session.viewports['Viewport: 1'].odbDisplay.
    setPrimarySectionPoint(
        sectionPoint={'shell < AH-36 > < 5 section points >':(
            'Mid, (fraction = 0.0)', 'SPOS, (fraction = 1.0)'), 'shell
            < NV-NS > < 5 section points >':('Mid, (fraction = 0.0)'
            ,
            'SPOS, (fraction = 1.0)'), 'beam < rectangular > < elset =
            ASSEMBLY_NONAME-TWEENDECKBALLAST-1.BEAMS-DECK >':(
            'Bottom Left Corner', 'Bottom Right Corner')}})

shearArray=[] #declare array where forces will be stored
for path in session.paths.items(): #counter for paths

    #change to local CSYS
    dtm = scratchAss.datumCsyses['CSYS-' + path[0][-4:]]
    session.viewports['Viewport: 1'].odbDisplay.
        basicOptions.setValues(transformationType=
            USER_SPECIFIED, datumCsys=dtm)

    #create xyData sets for each frame
    xyName = 'S12-' + path[0]
    for f in range(len(session.xyDataObjects['LPF'])): #
        counter to include all frames
        session.viewports['Viewport: 1'].odbDisplay.
            setFrame(step=0, frame=f) #choose frame
        session.XYDataFromPath(name=xyName, path=session.
            paths[path[0]], includeIntersections=True,
            projectOntoMesh=False,
            pathStyle=UNIFORM_SPACING, numIntervals=18,
            projectionTolerance=0, shape=UNDEFORMED,
            labelType=TRUE_DISTANCE)
        data = session.xyDataObjects[xyName]
        force = 0.0
        # Multiply the shear stress from each element with
        # the element thickness and length
        # to get each element's shear force. Sum up to get
        # the shear force for the current path
        for j in range(len(data)):
            if j == 0:
                force += data[j][1]*elementLength*
                    elementThickness*1.5 #[N]
            elif j == len(data) - 1:
                force += data[j][1]*elementLength*
                    elementThickness*0.5

```

```

        else:
            force += data[j][1]*elementLength*
                elementThickness
        # The first node is not included in the path - so
        # correct the shear force by adding the first
        # element
        # a second time
        shearArray.append(force)

# Declare arrays for each stiffener's force
ShearL1 = [] #[N]
ShearL2 = [] #[N]
ShearL3 = [] #[N]
num_inc=len(session.xyDataObjects['LPF'])
for i in range(num_inc):

    # sum shear force from upper and lower to get total shear
    # force carried by stiffener
    #(-(lower force) + (upper force))
    ShearL1.append( -(-shearArray[i] + shearArray[i + num_inc])
        ) # face of elements defined oppositely
    ShearL2.append( -shearArray[i +2*num_inc] + shearArray[i +
        3*num_inc] )
    ShearL3.append( -shearArray[i +4*num_inc] + shearArray[i +
        5*num_inc] )

#-----extract total reaction force-----
#create free body cut at BC-nodes
eLeaf = dgo.LeafFromElementSets(elementSets=(
    'NONAME-TWEENDECKBALLAST-1.BOUNDARYEDGES', ))
nLeaf = dgo.LeafFromNodeSets(nodeSets=(
    'NONAME-TWEENDECKBALLAST-1.BOUNDARYEDGES', ))
session.FreeBodyFromNodesElements(name='FreeBody-BCnodes',
    elements=eLeaf,
    nodes=nLeaf, summationLoc=NODAL_AVERAGE,
    componentResolution=CSYS,
    csysName=GLOBAL)
session.viewports['Viewport: 1'].odbDisplay.setValues(
    freeBodyNames=(
    'FreeBody-BCnodes', ), freeBody=ON)

#create xy data for total reaction force
session.XYDataFromFreeBody(odb=odb, force=ON, moment=OFF,
    resultant=ON,
    comp1=OFF, comp2=OFF, comp3=OFF)
session.xyDataObjects.changeKey(fromName='FreeBody-BCnodes
    force resultant',
    toName='totalRF')

#----- write to CSV-file
fout.write(odbName + ',' + '\n')

fout.write('displacement loadcenter (L2) [mm]' + ',')
for i in range(num_inc):

```



```

        fout.write(str(session.xyDataObjects['deltaL2'][i][1]*1000)
                  + ',')
fout.write('\n')
fout.write('Pressure load (LPF) [MPa]' + ',')
for i in range(num_inc):
    fout.write(str(session.xyDataObjects['LPF'][i][1]) + ',')
fout.write('\n')
fout.write('Reaction force (total load) [kN]' + ',')
for i in range(num_inc):
    fout.write(str(session.xyDataObjects['totalRF'][i][1]/1000)
              + ',')
fout.write('\n')

fout.write('ShearL1 [kN]' + ',')
for i in range(num_inc):
    fout.write(str(ShearL1[i]/1000) + ',')
fout.write('\n')
fout.write('ShearL2 [kN]' + ',')
for i in range(num_inc):
    fout.write(str(ShearL2[i]/1000) + ',')
fout.write('\n')
fout.write('ShearL3 [kN]' + ',')
for i in range(num_inc):
    fout.write(str(ShearL3[i]/1000) + ',')
fout.write('\n')
fout.write('Sum shear L1+L2+L3 [kN]' + ',')
for i in range(num_inc):
    fout.write(str(ShearL3[i]/1000+ShearL1[i]/1000+ShearL2[i]
                  ]/1000) + ',')
fout.write('\n')

# add space between data sets:
fout.write('\n')
fout.write('\n')
fout.write('\n \n \n \n \n')
odb.close()

fout.close()

# If no odb files were found
else:
    print "No ODB-files found in the specified folder"

#endregion

```

## A.6 Calculate Rule Design Loads

This script calculates rule design loads according to the DNV GL class notation Ice(1A\*). See Section 3 for explanations.

```
# ----- Calculate rule loads Ice(1A*)-----

# from DNVGL-RU-SHIP-Pt6Ch6, Section 2

# ----- Load patch 7.2.
h_0=1 # [m] ice thickness
h=0.35 # [m] design ice height

P_min=6600 # [kW] actual power, or as defined in [7.1.4]
c_1= 1.0 # Table 12 A factor which takes account of the probability
        that the design ice pressure occurs in a certain region of the hull
        for the ice class in question
delta_f=5000 #[tonnes] displacement

# ----- calculate c_d:
k_1=(sqrt(delta_f*P_min))/1000
#7.2 Table 11:
if k_1 <= 12: #in bow region
    a_1=30; b_1=230
else:
    a_1=6; b_1=518

c_d=(a_1*k_1+b_1)/1000 #A factor which takes account of the influence
        of the size and engine output of the ship. This factor is taken as
        maximum cd = 1.
if c_d >1:
    c_d=1

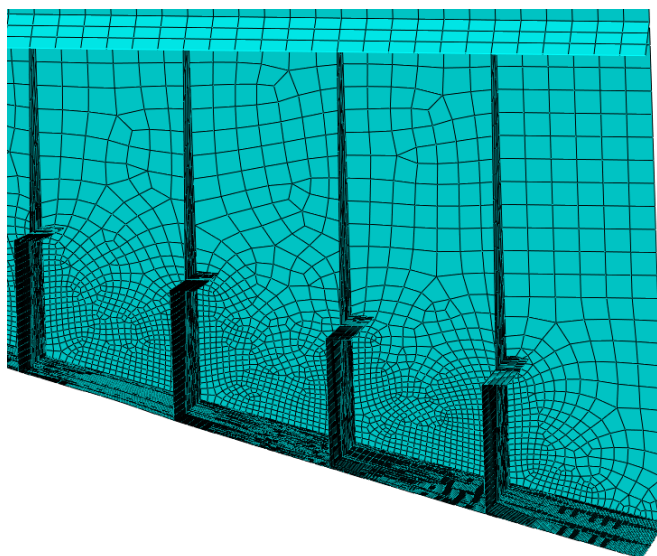
l_0=.6 # [m]
l_a=.312 #see table 13, approx 31,2cm for each step

# ----- calculate design pressure
P=[0,0,0,0,0]
c_a=P
P_design=P # declaring vector of design pressures
for i in range(1,6):
    c_a=sqrt(l_0/(l_a*i)) #A factor which takes account of the
        probability that the full length of the area under consideration
        will be under pressure at the same time. It is calculated by
        the formula:
    if c_a > 1:
        c_a=1
    elif c_a < .35:
        c_a=.35
    P[i-1]=5600*c_d*c_1*c_a #[kPa] #7.3.1 The design ice pressure
```

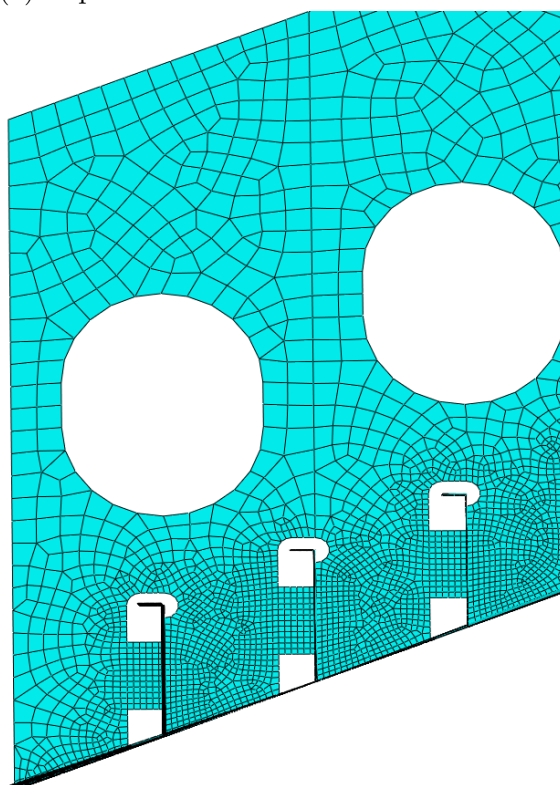
```
P_design[i-1]=1.8*5600*c_d*c_l*c_a #load factor of 1.8 used for  
analyses
```



## B Mesh Details

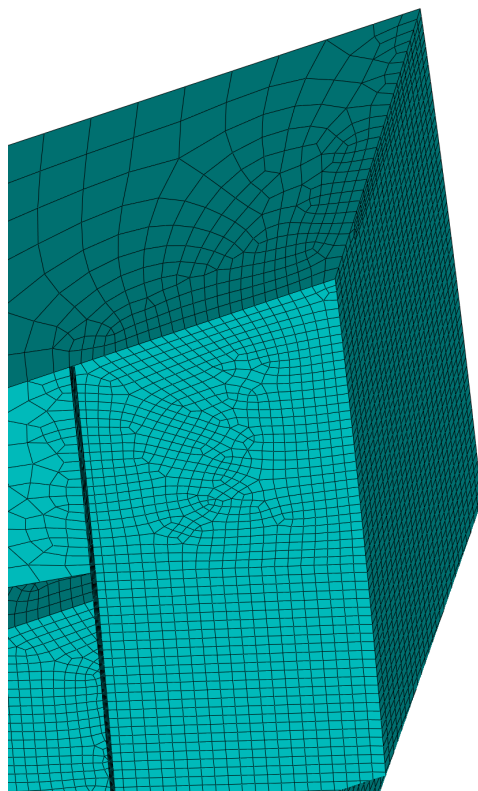


(a) Top deck mesh seen from below.

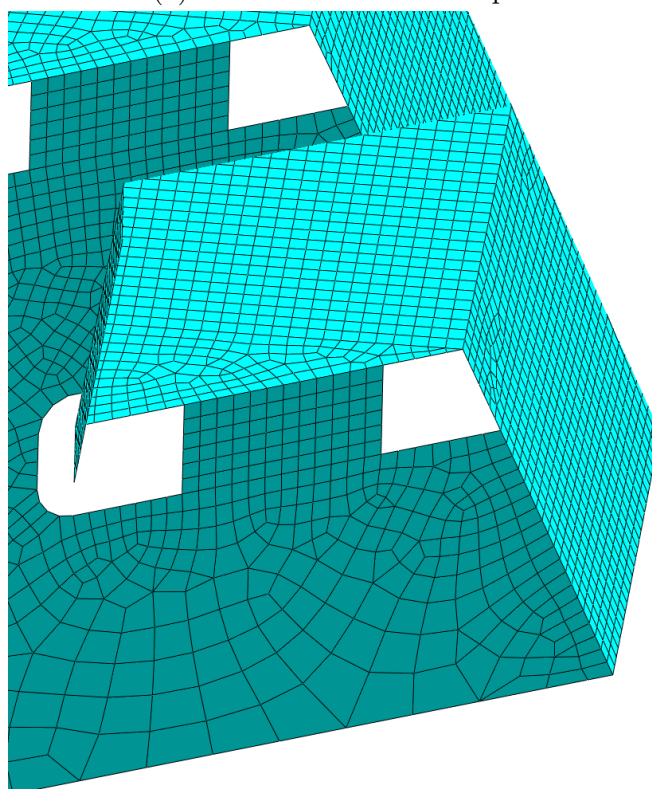


(b) Bottom deck mesh seen from above.

Figure B.1: Mesh details, decks.



(a) Mesh at a stiffener's top end.



(b) Mesh at a stiffener's bottom end.

Figure B.2: Mesh details, stiffeners.

## C Additional Results

### C.1 Verification of Stress Distributions along Paths

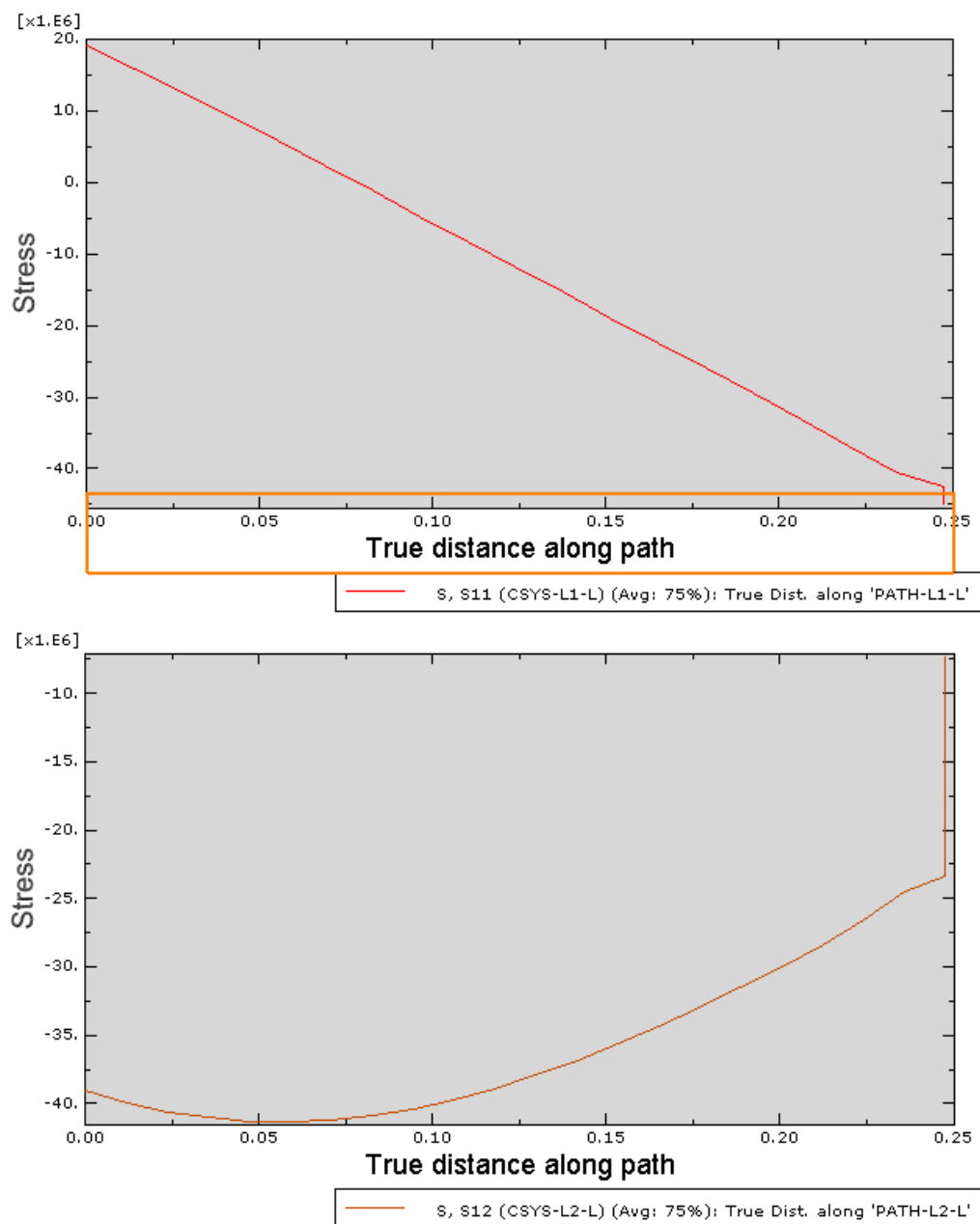


Figure C.1: Example of stress distribution along a path (cross section) at the lower end of a stiffener.

## C.2 Ultimate Strengths in Numbers

Table 8: Ultimate strengths from nonlinear analyses. "whole model", "all fixed".

		W0	W1	W2	W3	W4
allowable permanent deformation (w/l)		Capacities [MPa]				
H0	0,50 %	9,99946	5,72413	4,42685	3,9886	3,80779
	1,00 %	13,4984	7,6208	5,66142	4,82933	4,45678
H1	0,50 %	5,60264	3,12204	2,38465	2,13074	2,0287
	1,00 %	7,71898	4,20242	3,09441	2,62308	2,40842

Table 9: Ultimate strengths from nonlinear analyses. "half model", "partly fixed".

		W0	W1	W2	W3	W4
allowable permanent deformation (w/l)		Capacities [MPa]				
H0	0,50 %	9,53426	5,36635	4,0893	3,60854	3,36754
	1,00 %	13,6	7,37567	5,33544	4,44017	4,11092
H1	0,50 %	5,34614	2,93617	2,20551	1,92669	1,78618
	1,00 %	7,69187	4,09714	2,9297	2,4345	2,23391



## D Electronic Attachments

The following electronic attachments can be found in the file named `electronic_attachments.zip`

- Inputfiles for Abaqus analyses.
  - One for the "whole model" and "all fixed" BCs.
  - One for the "half model" and "partly fixed" BCs.
- Results in Excel-sheets.
  - From linear analyses, see Appendix D.1.
  - From nonlinear analyses. Load-deformation curves<sup>17</sup>, unloading curves, and detailed load deformation curves. Both for the "whole model" and "all fixed" BCs, and for the "half model" and "partly fixed" BCs.
  - Combined capacity curves for both linear and nonlinear analyses.

---

<sup>17</sup>Be aware that curves are not trustworthy for large displacements/loads since strain levels were too high.

## D.1 Excel-sheet with Results from Linear Analyses

Each column contain data from a path (cross section). The paths are named according to Figure 5.10a, and in addition U, M and L is added to denote "upper", "middle" and "lower", respectively. Maximum values over the cross section of Mises-, S12- and S11-stress components, utilization and capacity are included. The path data are organized so that the aft stiffeners are presented to the left, and the fore most at the right. Color coding makes it very easy to get an overview of the load carrying distribution, and of which stiffeners that are activated for the different load patches. Analysis results for five different load patch widths (W0-W4), two different heights (H0-H1), and for three different load-locations are presented. A screenshot of the sheet is seen in Figure D.1.

load	1000000 Pa	Analysis type	Linear <th colspan="16">load dimensions</th>	load dimensions																					
Sigma yield	355000000 Pa	BC	All-fixed	Height:	409cm	StepH:	Height/2	Width:	312cm	StepW:	Width/2														
Material stiffener web	AH-36																								
Path name	LA-L	LA-U	L1-L	L1-U	L2-L	L2-M	L2-U	L3-L	L3-U	L4-L	L4-U	L5-L	L5-U	L6-L	L6-U	L7-L	L7-U	L8-L	L8-U						
Stiffener where center of load patch																									
Job name	Maximum von Mises stress over web cross section [Pa]																								
Job-LoadPatch-W0-H0.odb	3,66E+06	5,94E+06	2,51E+07	1,33E+07	6,34E+07	9,49E+07	3,53E+07	2,92E+07	1,60E+07	3,76E+06	9,20E+06	2,84E+05	3,12E+05	3,28E+05	1,51E+05	3,15E+05	1,16E+05	2,58E+05	9,34E+04	1					
Job-LoadPatch-W1-H0.odb	7,69E+06	1,08E+07	5,84E+07	2,72E+07	1,02E+08	1,42E+08	5,41E+07	6,69E+07	3,39E+07	1,33E+07	1,92E+07	7,37E+05	7,47E+05	6,46E+05	2,89E+05	6,26E+05	2,42E+05	5,17E+05	1,90E+05	3					
Job-LoadPatch-W2-H0.odb	2,21E+07	1,18E+07	9,07E+07	3,93E+07	1,16E+08	1,52E+08	5,75E+07	1,00E+08	4,77E+07	3,42E+07	2,65E+07	1,95E+06	1,91E+06	9,10E+05	3,89E+05	8,68E+05	3,84E+05	7,26E+05	2,74E+05	4					
Job-LoadPatch-W3-H0.odb	4,89E+07	2,04E+07	1,08E+08	4,40E+07	1,19E+08	1,53E+08	5,56E+07	1,20E+08	5,39E+07	6,59E+07	3,30E+07	4,73E+06	4,44E+06	1,13E+06	5,44E+05	9,80E+05	5,63E+05	8,33E+05	3,35E+05	5					
Job-LoadPatch-W4-H0.odb	6,78E+07	3,26E+07	1,13E+08	4,43E+07	1,18E+08	1,53E+08	5,40E+07	1,25E+08	5,54E+07	8,92E+07	4,39E+07	8,64E+06	8,21E+06	1,45E+06	9,82E+05	9,64E+05	7,43E+05	8,17E+05	3,59E+05	5					
Utilization wrt. Yielding [-]																									
Job-LoadPatch-W0-H0.odb	0,01	0,02	0,07	0,04	0,18	0,27	0,10	0,08	0,04	0,01	0,03	0,00	0,00	0,00	0,00	0,00	0,00	0,00	0,00	0,00					
Job-LoadPatch-W1-H0.odb	0,02	0,03	0,16	0,08	0,29	0,40	0,15	0,19	0,10	0,04	0,05	0,00	0,00	0,00	0,00	0,00	0,00	0,00	0,00	0,00					
Job-LoadPatch-W2-H0.odb	0,06	0,03	0,26	0,11	0,33	0,43	0,16	0,28	0,13	0,10	0,07	0,01	0,01	0,00	0,00	0,00	0,00	0,00	0,00	0,00					
Job-LoadPatch-W3-H0.odb	0,14	0,06	0,30	0,12	0,33	0,43	0,16	0,34	0,15	0,19	0,09	0,01	0,01	0,00	0,00	0,00	0,00	0,00	0,00	0,00					
Job-LoadPatch-W4-H0.odb	0,19	0,09	0,32	0,12	0,33	0,43	0,15	0,35	0,16	0,25	0,12	0,02	0,02	0,00	0,00	0,00	0,00	0,00	0,00	0,00					
Capacity, load at first yield [Pa]																									
Job-LoadPatch-W0-H0.odb	9,70E+07	5,98E+07	1,41E+07	2,66E+07	5,60E+06	3,74E+06	1,01E+07	1,22E+07	2,22E+07	9,45E+07	3,86E+07	1,25E+09	1,14E+09	1,08E+09	2,35E+09	1,13E+09	3,06E+09	1,38E+09	3,80E+09	2					
Job-LoadPatch-W1-H0.odb	4,62E+07	3,29E+07	6,07E+06	1,30E+07	3,47E+06	2,50E+06	6,56E+06	5,30E+06	1,05E+07	2,68E+07	1,85E+07	4,82E+08	4,75E+08	5,49E+08	1,23E+09	5,67E+08	1,47E+09	6,87E+08	1,87E+09	1					
Job-LoadPatch-W2-H0.odb	1,60E+07	3,01E+07	3,92E+06	9,03E+06	3,05E+06	2,34E+06	6,18E+06	3,53E+06	7,44E+06	1,04E+07	1,34E+07	1,82E+08	1,86E+08	3,90E+08	9,13E+08	4,09E+08	9,25E+08	4,89E+08	1,30E+09	7					
Job-LoadPatch-W3-H0.odb	7,26E+06	1,74E+07	3,30E+06	8,07E+06	2,99E+06	2,33E+06	6,39E+06	2,97E+06	6,59E+06	5,39E+06	1,07E+07	7,50E+07	7,99E+07	3,13E+08	6,53E+08	3,62E+08	6,30E+08	4,26E+08	1,06E+09	6					
Job-LoadPatch-W4-H0.odb	5,24E+06	1,09E+07	3,15E+06	8,02E+06	3,00E+06	2,33E+06	6,57E+06	2,83E+06	6,40E+06	3,98E+06	8,08E+06	4,11E+07	4,32E+07	2,44E+08	3,61E+08	3,68E+08	4,77E+08	4,34E+08	9,88E+08	6					
Stiffener where center of load patch																									
Job name	Maximum shear stress (S12) over web cross section [Pa]																								
Job-LoadPatch-W0-H0.odb	4,64E+05	1,02E+06	9,12E+06	5,29E+06	2,02E+07	3,22E+06	1,80E+07	9,07E+06	4,94E+06	7,53E+05	2,44E+06	1,35E+05	8,40E+04	5,48E+04	4,81E+04	1,53E+04	5,23E+04	3,33E+03	4,16E+04	1					
Job-LoadPatch-W1-H0.odb	1,81E+06	9,06E+05	1,96E+07	1,33E+07	3,34E+07	5,77E+06	2,73E+07	2,03E+07	1,34E+07	3,61E+06	2,93E+06	3,82E+05	2,63E+05	1,15E+05	8,98E+04	2,90E+04	1,09E+05	5,91E+03	8,43E+04	3					
Job-LoadPatch-W2-H0.odb	7,95E+06	4,97E+06	2,88E+07	2,14E+07	3,86E+07	7,23E+06	2,86E+07	3,09E+07	2,13E+07	9,93E+06	2,19E+06	9,60E+05	7,53E+05	1,83E+05	1,08E+05	3,17E+04	1,74E+05	1,00E+04	1,23E+05	4					
Job-LoadPatch-W3-H0.odb	1,60E+07	1,31E+07	3,39E+07	2,55E+07	3,94E+07	8,19E+06	2,71E+07	3,76E+07	2,51E+07	1,94E+07	1,11E+07	2,05E+06	1,91E+06	2,88E+05	1,33E+05	4,79E+04	2,57E+05	1,60E+04	1,56E+05	5					
Job-LoadPatch-W4-H0.odb	2,11E+07	1,89E+07	3,58E+07	2,64E+07	3,89E+07	8,77E+06	2,59E+07	4,00E+07	2,58E+07	2,67E+07	1,82E+07	3,34E+06	3,70E+06	4,66E+05	1,95E+05	1,24E+05	3,40E+05	2,45E+04	1,68E+05	4					
Utilization wrt. Yielding [-]																									
Job-LoadPatch-W0-H0.odb	0,00	0,00	0,04	0,03	0,10	0,02	0,09	0,04	0,02	0,00	0,01	0,00	0,00	0,00	0,00	0,00	0,00	0,00	0,00	0,00					
Job-LoadPatch-W1-H0.odb	0,01	0,00	0,10	0,06	0,16	0,03	0,13	0,10	0,07	0,02	0,01	0,00	0,00	0,00	0,00	0,00	0,00	0,00	0,00	0,00					
Job-LoadPatch-W2-H0.odb	0,04	0,02	0,14	0,10	0,19	0,04	0,14	0,15	0,10	0,05	0,01	0,00	0,00	0,00	0,00	0,00	0,00	0,00	0,00	0,00					
Job-LoadPatch-W3-H0.odb	0,08	0,06	0,17	0,12	0,19	0,04	0,13	0,18	0,12	0,09	0,05	0,01	0,01	0,00	0,00	0,00	0,00	0,00	0,00	0,00					
Job-LoadPatch-W4-H0.odb	0,10	0,09	0,17	0,13	0,19	0,04	0,13	0,20	0,13	0,13	0,09	0,02	0,02	0,00	0,00	0,00	0,00	0,00	0,00	0,00					
Capacity, load at first yield [Pa]																									
Job-LoadPatch-W0-H0.odb	4,42E+08	2,00E+08	2,25E+07	3,87E+07	1,02E+07	6,36E+07	1,14E+07	2,26E+07	4,15E+07	2,72E+08	8,41E+07	1,52E+09	2,44E+09	3,74E+09	4,26E+09	1,34E+10	3,92E+09	6,16E+10	4,93E+09	1					
Job-LoadPatch-W1-H0.odb	1,13E+08	2,26E+08	1,05E+07	1,54E+07	6,14E+06	3,53E+07	7,49E+06	1,01E+07	1,53E+07	5,68E+07	7,01E+07	5,36E+08	7,79E+08	1,78E+09	2,28E+09	7,06E+09	1,88E+09	3,47E+10	2,43E+09	5					
Job-LoadPatch-W2-H0.odb	2,58E+07	4,13E+07	7,11E+06	9,56E+06	5,31E+06	2,34E+07	7,17E+06	6,63E+06	9,63E+06	2,06E+07	9,34E+07	2,14E+08	2,72E+08	1,12E+09	1,90E+09	6,47E+09	1,18E+09	2,04E+10	1,66E+09	4					
Job-LoadPatch-W3-H0.odb	1,28E+07	1,57E+07	6,04E+06	8,04E+06	5,21E+06	2,50E+07	7,57E+06	5,45E+06	8,15E+06	1,06E+07	1,84E+07	9,98E+07	1,07E+08	7,12E+08	1,55E+09	4,28E+09	7,97E+08	1,28E+10	1,32E+09	4					
Job-LoadPatch-W4-H0.odb	9,70E+06	1,08E+07	5,73E+06	7,76E+06	5,26E+06	2,34E+07	7,92E+06	5,12E+06	7,93E+06	7,68E+06	1,12E+07	6,13E+07	5,54E+07	4,40E+08	1,05E+09	1,65E+09	6,02E+08	8,38E+09	1,22E+09	4					
Stiffener where center of load patch																									
Job name	Maximum bending stress (S11) over web cross section [Pa]																								
Job-LoadPatch-W0-H0.odb	3,51E+06	3,58E+06	2,27E+07	1,07E+07	6,06E+07	9,48E+07	6,05E+06	2,75E+07	1,30E+07	3,51E+06	8,73E+06	2,17E+05	1,20E+05	3,19E+05	7,80E+04	3,21E+05	2,45E+04	2,63E+05	4,02E+04	1					
Job-LoadPatch-W1-H0.odb	7,73E+06	7,40E+06	5,34E+07	1,82E+07	9,75E+07	1,42E+08	1,72E+07	6,25E+07	2,13E+07	1,26E+07	1,82E+07	6,50E+05	1,90E+05	6,22E+05	1,44E+05	6,37E+05	4,73E+04	5,26E+05	8,32E+04	3					

Figure D.1: Snip of the Excel-sheet displaying data from the linear analyses.